Measurement-Based Modeling of Wireless Propagation Channels - MIMO and UWB

Kåredal, Johan

2009

Measurement-Based Modeling of Wireless Propagation Channels

–

MIMO and UWB

Johan Kåredal

Lund 2009

Department of Electrical and Information Technology
Lund University
Box 118, SE-221 00 LUND
SWEDEN

This thesis is set in Computer Modern 10pt
with the LaTeX Documentation System

Series of licentiate and doctoral theses
No. 14
ISSN 1654-790X

Printed in Sweden by *Tryckeriet i E-huset*, Lund.
January 2009.

Till dem som finns med oss,
och dem som inte gör det.

Sammanfattning

Det tillgängliga frekvensutrymmet för radiokommunikation är begränsat. Därför har mycket forskning fokuserat på trådlösa kommunikationssystem som kan ge en tillförlitlig och snabb uppkoppling utan att ta överdrivna frekvensresurser i anspråk. Två system som rönt särskilt stort intresse de senaste åren är så kallade *flerantennsystem* (MIMO) och *ultrabredbandssystem* (UWB), som använder två olika sätt för att hantera det begränsade frekvensutrymmet. MIMO-system förlitar sig på utnyttjande av *rumsdomänen* (d.v.s. använder fler antenner) för att kunna ge ett ökat informationsflöde. Genom avancerad signalbehandling kan varje *enskild länk* (en sändar- till en mottagarantenn) överföra en egen dataström, och den möjliga datahastigheten ökar således med antalet antenner. UWB-system, å andra sidan, är tänkta att fungera helt utan särskild frekvenstilldelning genom att *samexistera* med befintliga system. Detta är möjligt genom att UWB-signalen sprids över ett så stort frekvensband att effekten per Hertz blir låg nog att endast uppfattas som svagt brus av andra mottagare. Emellertid är prestandan hos MIMO- och UWB-system (t.ex. i form av datahastighet) starkt beroende på egenskaperna hos den trådlösa *utbredningskanalen*, vilket är den länk som sammanbinder en radiosändare med en mottagare. Olika sändar- och mottagartekniker måste därför utvärderas under realistiska kanalförhållanden, och kunskap om utbredningskanalen är således en viktig del i designen av framtida trådlösa kommunikationssystem. Exempel på sådana system som täcks in av denna avhandling är trådlösa personnätverk (artiklarna I och II), fordon-till-fordonkommunikation (artikel III), kommunikation mellan datorenheter (artikel IV) och sensornätverk för industritillämpningar (artikel V). En vanlig metod för att utvärdera ett trådlöst systems prestanda är att använda *kanalmodeller*, d.v.s. modeller som på matematisk väg kan återskapa verklighetsnära utbredningsegenskaper. Kanalmodellering är temat för den här avhandlingen, som innehåller en samling artiklar som analyserar och modellerar beteendet hos utbredningskanalerna för några framtida MIMO- och UWB-system.

Artikel I undersöker hur mänsklig närvaro påverkar de snabba och långsamma variationerna hos den mottagna signalen, så kallade *fädningseffekter*, i trådlösa personnätverk. Sådana nätverk utgörs i allmänhet av kommunikation mellan små handhållna (eller på andra sätt kroppsnära) konsumentelektronikenheter (t.ex. handdatorer), där framtida produkter förutspås innehålla flera antennelement. Resultat från utförliga kanalmätningar visar att kroppen har en markant inverkan på den mottagna signalen. Slutsatsen är att den exakta positionen hos ett antennelement i förhållande till kroppen styr hur signalen varierar. Dessa observationer sammanfattas i en simuleringsmodell för all fädning hos en enskild länk.

Artikel II utökar modellen från artikel I till att gälla även för flerantennsystem och presenterar därigenom en komplett MIMO-kanalmodell. Artikeln kombinerar strukturen hos en klassisk MIMO-modell med resultat från artikel I genom att ge olika fädningsegenskaper till de olika antennelementen. Modellen verifieras gentemot mätdata och visar sig kunna återskapa effekter hos MIMO-kanaler för personnätverk som tidigare modeller inte klarar. Artikeln innehåller också en beskrivning av modellparametrarnas beteende för ett specifikt personnätverksscenario.

Artikel III presenterar en MIMO-kanalmodell för kommunikation mellan fordon. Först dras slutsatser kring de viktigaste utbredningsegenskaperna baserat på resultat från ett stort antal kanalmätningar utförda på motor- och landsvägar utanför Lund. På grund av deras starkt tidsvarierande beteende är ingen tidigare MIMO-modell kapabel att beskriva den här typen av utbredningskanaler. I stället förespråkas en ny *geometrisk-stokastisk* modell, som baseras på att sändare, mottagare och *punktspridare* placeras slumpvis i en geometri. Punktspridarna används för att representera diverse signalpåverkande objekt i kanalen, och dessa utplaceras i enlighet med stokastiska fördelningar och tilldelas slumpvis olika utbredningsegenskaper (t.ex. i form av en amplitud). Därefter beräknas signalvägen från sändare till mottagare via varje punktspridare och den totala signalen erhålls genom summering av alla enskilda bidrag. Den föreslagna modellen skiljer på diffusa bidrag (som inte kan härledas till ett enskilt objekt) och de som härstammar från interaktion med *signifikanta* objekt i utbredningskanalen, t.ex. bilar, skyltar och hus. De senares fädningsegenskaper extraheras från mätdata och uppvisar ett beteende som inkluderas i modellen på ett nyskapande sätt.

Artikel IV studerar UWB-utbredningskanaler inuti datorhöljen. Mätresultat från två olika datorer visar att utbredningskanalen bara uppvisar mindre variationer för olika datorer och positioner inom höljena. Det noteras också att datorerna ger upphov till störningseffekt, men att denna är begränsad till ett flertal mindre frekvensband. Två principer har föreslagits för UWB-system: *impulsradio* och *multibands-UWB*. Impulsradio bygger på att man sänder ex-

tremt korta pulser, där frekvensbandbredden som upptas är omvänt proportionell mot pulslängden (d.v.s. ju kortare puls, desto mer frekvensutrymme upptas). Multibands-UWB bygger i stället på klassiska radiotekniker, med den skillnaden att ett stort antal frekvenser utnyttjas. En fördel med den senare varianten är att det är enkelt att undvika vissa frekvensband, genom att helt enkelt låta bli att använda dem. Slutsatsen i den här artikeln pekar alltså mot att multibands-UWB är en lämpligare lösning för den här typen av tillämpningar.

Artikel V beskriver en UWB-kanalmodell baserat på de första UWB-mätningarna i en industrimiljö. Impulsradiokonceptet medför att det är av stort intresse att studera UWB-kanalers *impulssvar*, d.v.s. hur kanalen reagerar på utsändning av en extremt kort puls. Studier av mätresultat från två olika fabriksmiljöer visar att ekona av den utsända signalen anländer till mottagaren i tätt packade grupper, så kallade kluster. Därför används en klassisk multiklustermodell för att beskriva kanalens impulssvar. Delar av resultatet från den här artikeln användes också i utvecklingen av kanalmodellen till UWB-standarden IEEE 802.15.4a.

Sammanfattningsvis vill den här avhandlingen bidra till en ökad förståelse för beteendet hos trådlösa utbredningskanaler för MIMO- och UWB-system. Tre detaljerade simuleringsmodeller som kan användas vid utvecklingen av sådana system presenteras, två för MIMO och en för UWB. Därigenom kan avhandlingen förhoppningsvis bidra till en effektivare prestanda hos framtidens trådlösa kommunikationssystem.

Abstract

Future wireless systems envision higher speeds and more reliable services but at the same time face challenges in terms of bandwidth being a limited resource. Two promising techniques that can provide an increased throughput without requiring additional bandwidth allocation are multiple-input multiple-output (MIMO) systems and ultra-wideband (UWB) systems. However, the performance of such systems is highly dependent on the properties of the wireless propagation channel, and an understanding of the channel is therefore crucial in the design of future wireless systems. Examples of such systems covered by this thesis are wireless personal area networks (papers I and II), vehicle-to-vehicle communications (paper III), board-to-board communications inside computers (paper IV) and sensor networks for industrial applications (paper V). Typically, channel models are used to evaluate the performance of different transmission and reception schemes. Channel modeling is the focus of this thesis, which contains a collection of papers that analyze and model the behavior of MIMO and UWB propagation channels.

Paper I investigates the fading characteristics of wireless personal area networks (PANs), networks that typically involve human influence close to the antenna terminals. Based on extensive channel measurements using irregular antenna arrays, typical properties of PAN propagation channels are discussed and a model for the complete fading of a single link is presented.

Paper II extends the model from paper I to a complete MIMO channel model. The paper combines the classical LOS model for MIMO with results from paper I by prescribing different fading statistics and mean power at the different antenna elements. The model is verified against measurement data and the paper also provides a parameterization for an example of a PAN scenario.

Paper III presents a geometry-based stochastic MIMO model for vehicle-to-vehicle communications. The most important propagation effects are discussed based on the results from extensive channel measurements, and the modeling approach is motivated by the non-stationary behavior of such channels. The

model distinguishes between diffuse contributions and those stemming from interaction with significant objects in the propagation channel, and the observed fading characteristics of the latter are stochastically accounted for in the model.

Paper IV gives a characterization of UWB propagation channels inside desktop computer chassis. By studying measurement results from two different computers, it is concluded that the propagation channel only shows minor differences for different computers and positions within the chassis. It is also found out that the interference power produced by the computer is limited to certain subbands, suggesting that multiband UWB systems are more suitable for this type of applications.

Paper V describes a UWB channel model based on the first UWB measurements in an industrial environment. Analyzing results from two different factory halls, it is concluded that energy arrives at the receiver in clusters, which motivates the use of a classical multi-cluster model to describe the channel impulse response. Parts of the results from this paper were also used as input to the channel model in the IEEE 802.15.4a UWB standardization work.

In summary, the work within this thesis leads to an increased understanding of the behavior of wireless propagation channels for MIMO and UWB systems. By providing three detailed simulation models, two for MIMO and one for UWB, it can thus contribute to a more efficient design of the wireless communications systems of tomorrow.

Preface

Being originally devoted to mechanical engineering, I finished my undergraduate studies in engineering physics at LTH in 2002 with a master's project on antenna design. Even so, my first post-educational work was at Husqvarna AB, where I took part in the research and development of forestry clearing saws. Having not forgotten the appealing challenges of wireless communications briefly encountered during my final undergraduate work, however, I did not hesitate to apply for an open Ph.D. student position in the Radio Systems Group when it was presented to me in 2003. Since I had the pleasure of also being offered the position, I soon thereafter started my new career under the supervision of Professor Andreas F. Molisch and co-supervision of Associate Professor Fredrik Tufvesson and Professor Ove Edfors.

When I started at the department, ultra-wideband (UWB) communications was a really hot topic, and the IEEE was about to start the work on a new standard, IEEE 802.15.4a. My first scientific work thus focused on measurements and modeling of a particular environment for the 802.15.4a channel model, namely industrial propagation environments. The attention given to UWB was also the motivation for my next paper, containing a characterization of UWB channels within desktop computer chassis. After our research group acquired a multiple-input multiple-output (MIMO) channel sounder from Medav in 2004, my work also became focused on MIMO channel characterization. Taking part in the European Union research project MAGNET, which set out to lay the foundation for small, short-range, future networks commonly referred to as personal area networks (PANs), our group performed extensive MIMO channel measurements for such applications. Another fruitful cooperation, between Lund, TU Vienna and ftw. in Austria, focused on characterizing MIMO channels for vehicle-to-vehicle communications and to develop a propagation model for such environments, the latter becoming my task.

This doctoral thesis thus concludes my work as a Ph.D. student. The thesis consists of two parts, where the first gives an overview of the research field I have been working in, where my contributions fit in, as well as a brief summary

of the latter. The second part contains my main scientific work by including the following papers:

[1] J. Karedal, A. J. Johansson, F. Tufvesson and A. F. Molisch, "A Measurement-Based Fading Model for Wireless Personal Area Networks," in *IEEE Transactions on Wireless Communications*, vol. 7, no. 11, pp. 4575–4585, Nov. 2008.

[2] J. Karedal, P. Almers, A. J. Johansson, F. Tufvesson and A. F. Molisch, "A MIMO Channel Model for Wireless Personal Area Networks," submitted to *IEEE Transactions on Wireless Communications*, 2009.

[3] J. Karedal, F. Tufvesson, N. Czink, A. Paier, C. Dumard, T. Zemen, C. F. Mecklenbräuker and A. F. Molisch, "A Geometry-Based Stochastic MIMO Model for Vehicle-to-Vehicle Communications," accepted with minor revision and resubmitted to *IEEE Transactions on Wireless Communications*, 2008.

[4] J. Karedal, A. P. Singh, F. Tufvesson and A. F. Molisch, "Characterization of a Computer Board-to-Board Ultra-Wideband Channel," in *IEEE Communication Letters*, vol. 11, no. 6, pp. 468–470, June 2007.

[5] J. Karedal, S. Wyne, P. Almers, F. Tufvesson and A. F. Molisch, "A Measurement-Based Statistical Model for Industrial Ultra-Wideband Channels," in *IEEE Transactions on Wireless Communications*, vol. 6, no. 8, pp. 3028–3037, Aug. 2007.

My time as a Ph.D. student has also rendered the following publications, which are not included in my thesis:

[6] S. Wyne, A. F. Molisch, P. Almers, G. Eriksson, J. Karedal and F. Tufvesson, "Outdoor-to-Indoor Office MIMO Measurements and Analysis at 5.2 GHz," in *IEEE Transactions on Vehicular Technology*, vol. 57, no. 3, pp. 1374–1386, May 2008.

[7] P. Almers, T. Santos, F. Tufvesson, A. F. Molisch, J. Karedal and A. J. Johansson, "Antenna Selection in Measured Indoor Channels," in *IET Microwaves, Antennas & Propagation*, vol. 1, no. 5, pp. 1092–1100, Oct. 2007.

[8] A. F. Molisch, D. Cassioli, C.-C. Chong, S. Emami, A. Fort, B. Kannan, J. Karedal, J. Kunisch, H. G. Schantz, K. Siwiak and M. Z. Win, "A Comprehensive Standardized Model for Ultrawideband Propagation Channels," in *IEEE Transactions on Antennas and Propagation*, vol. 54, no. 11, pp. 3151–3166, Nov. 2006.

[9] J. Karedal, F. Tufvesson, N. Czink, A. Paier, C. Dumard, T. Zemen, C. F. Mecklenbräuker and A. F. Molisch, "Measurement-Based Modeling of Vehicle-to-Vehicle MIMO Channels," to appear in *Proc. IEEE International Conference on Communications (ICC2009)*, Dresden, Germany, June 2009.

[10] A. F. Molisch, F. Tufvesson, J. Karedal, and C. F. Mecklenbräuker, "Propagation aspects of vehicle-to-vehicle communications – an overview," in *Proc. IEEE Radio and Wireless Symposium (RWS09)*, San Diego, USA, Jan. 2009.

[11] T. Santos, J. Karedal, P. Almers, F. Tufvesson and A. F. Molisch, "Scatterer Detection by Successive Cancellation for UWB – Method and Experimental Verification," in *Proc. IEEE Vehicular Technology Conference (VTC2008-Spring)*, Singapore, Canada, vol. 1, pp. 445–449, May 2008.

[12] L. Bernadó, T. Zemen, A. Paier, G. Matz, J. Karedal, N. Czink, C. Dumard, F. Tufvesson, M. Hagenauer, A. F. Molisch and C. F. Mecklenbräuker, "Non-WSSUS Vehicular Channel Characterization at 5.2 GHz – Spectral Divergence and Time-Variant Coherence Parameters," in *Proc. URSI General Assembly*, 2008.

[13] A. Paier, T. Zemen, L. Bernadó, G. Matz, J. Karedal, N. Czink, C. Dumard, F. Tufvesson, A. F. Molisch, C. F. Mecklenbräuker, "Non-WSSUS vehicular channel characterization in highway and urban scenarios at 5.2 GHz using the local scattering function," in *Proc. International Workshop on Smart Antennas (WSA)*, vol. 1, pp. 9–15, Feb. 2008.

[14] A. Paier, J. Karedal, N. Czink, H. Hofstetter, C. Dumard, T. Zemen, F. Tufvesson, A. F. Molisch and C. F. Mecklenbräuker, "Car-to-Car Radio Channel Measurements at 5 GHz: Pathloss, Power-Delay Profile, and Delay-Doppler Spectrum," in *Proc. International Symposium on Wireless Communication Systems ISWCS*, Trondheim, Norway, vol. 1, pp. 224–228, Oct. 2007.

[15] A. Paier, J. Karedal, N. Czink, H. Hofstetter, C. Dumard, T. Zemen, F. Tufvesson, A. F. Molisch and C. F. Mecklenbräuker, "First Results from Car-to-Car and Car-to-Infrastructure Radio Channel Measurements at 5.2 GHz," in *Proc. International Symposium on Personal, Indoor and Mobile Radio Communications PIMRC*, Athens, Greece, vol. 1, pp. 1–5, Sept. 2007.

[16] J. Karedal, A. J Johansson, F. Tufvesson and A. F. Molisch, "Shadowing effects in MIMO Channels for Personal Area Networks," in *Proc. IEEE*

Vehicular Technology Conference (VTC2006-Fall), Montreal, Canada, vol. 1, pp. 173–177, Sept. 2006.

[17] P. Almers, T. Santos, F. Tufvesson, A. F. Molisch, J. Karedal and A. J Johansson, "Measured Diversity Gains from MIMO Antenna Selection," in *Proc. IEEE Vehicular Technology Conference (VTC2006-Fall)*, Montreal, Canada, vol. 1, pp. 1–6, Sept. 2006.

[18] S. Wyne, N. Czink, J. Karedal, P. Almers, F. Tufvesson and A. F. Molisch, "A Cluster-based Analysis of Outdoor-to-Indoor Office MIMO Measurements at 5.2 GHz," in *Proc. IEEE Vehicular Technology Conference (VTC2006-Fall)*, Montreal, Canada, vol. 1, pp. 22–26, Sept. 2006.

[19] A. F. Molisch, K. Balakrishnan, D. Cassioli, C.-C. Chong, S. Emami, A. Fort, J. Karedal, J. Kunisch, H. G. Schantz and K. Siwiak, "A Comprehensive Model for Ultrawideband Propagation Channels," in *Proc. IEEE Global Telecommunications Conference (GLOBECOM)*, St. Louis, USA, vol. 6, pp. 3648–3653, Nov.-Dec. 2005.

[20] G. M. Khan, A. A. Ashraf, J. Karedal, F. Tufvesson and A. F. Molisch, "Measurements and Analysis of UWB Channels in Industrial Environments," in *Proc. International Symposium on Wireless Personal Multimedia Communications (WPMC)*, Aalborg, Denmark, Sept. 2005.

[21] J. Karedal, A. J. Johansson, F. Tufvesson and A. F. Molisch, "Characterization of MIMO channels for Personal Area Networks at 5 GHz," in *Proc. European Signal Processing Conference (EUSIPCO)*, Florence, Italy, Sept. 2005.

[22] A. J. Johansson, J. Karedal, F. Tufvesson and A. F. Molisch, "MIMO Channel Measurements for Personal Area Networks," in *Proc. IEEE Vehicular Technology Conference (VTC2005-Spring)*, Stockholm, Sweden, vol. 1, pp. 171–176, May–June, 2005.

[23] S. Wyne, A. F. Molisch, P. Almers, G. Eriksson, J. Karedal and F. Tufvesson, "Statistical Evaluation of Outdoor-to-Indoor Office MIMO Measurements at 5.2 GHz," in *Proc. IEEE Vehicular Technology Conference (VTC2005-Spring)*, Stockholm, Sweden, vol. 1, pp. 146–150, May–June, 2005.

[24] J. Karedal, S. Wyne, P. Almers, F. Tufvesson and A. F. Molisch, "UWB Channel Measurements in an Industrial Environment," in *Proc. IEEE Global Telecommunications Conference (GLOBECOM)*, Dallas, USA, vol. 6, pp. 3511–3516, Nov. 2004.

[25] J. Karedal, S. Wyne, P. Almers, F. Tufvesson and A. F. Molisch, "Statistical Analysis of the UWB Channel in an Industrial Environment," in *Proc. IEEE Vehicular Technology Conference (VTC2004-Fall)*, Los Angeles, USA, vol. 1, pp. 81–85, Sept. 2004.

[26] S. Wyne, P. Almers, G. Eriksson, J. Karedal, F. Tufvesson and A. F. Molisch, "Outdoor-to-Indoor Office MIMO Measurements at 5.2 GHz," in *Proc. IEEE Vehicular Technology Conference (VTC2004-Fall)*, Los Angeles, USA, vol. 60, pp. 101–105, Sept. 2004.

[27] S. Wyne, P. Almers, B. K. Lau, G. Eriksson, J. Karedal, F. Tufvesson and A. F. Molisch, "Why Channel Matrix in LOS Scenarios has Zero Mean Entries," in *COST273*, TD(04)194, Duisburg, Germany, Sept. 2004.

[28] S. Wyne, P. Almers, G. Eriksson, J. Karedal, A. Waern, B. Lundborg, F. Tufvesson and A. F. Molisch, "Outdoor to Indoor Office MIMO Measurements at 5.2 GHz," in *COST273* TD(04)152, Duisburg, Germany, Sept. 2004.

[29] P. Almers, O. Edfors, F. Florén, A. J. Johansson, J. Karedal, B. K. Lau, A. F. Molisch, A. Stranne, F. Tufvesson and S. Wyne, "Exercises," in *Wireless Communications*, A. F. Molisch, Chichester: IEEE PressWiley, 2005.

Acknowledgements

Writing this thesis ends the journey I set out on in the summer of 2003. During my time at the department, I have encountered numerous people whose help have been a true asset, and to whom I owe my deepest gratitude. I therefore want to take the opportunity to acknowledge all those who, in one way or another, have contributed to this reaching of my goal.

First and foremost, I want to express my deepest gratitude to my main supervisor Prof. Andreas F. Molisch for having given me the opportunity to pursue my Ph.D. studies by taking me under his wings during these years. His sincere interest in science, his deep knowledge in the vast field of wireless communications and his always having the time for discussions, despite being mostly located overseas (or on airplanes), has been a constant source of inspiration. With the main supervisor located overseas, the pressure on the co-supervisors is bound to increase. My co-supervisor, Prof. Fredrik Tufvesson, has handled this situation tremendously, to which I am truly grateful. Thank you for fruitful discussions, support, eagle-eye proofreading and always running the Lund base camp. I also want to thank my second co-supervisor, Prof. Ove Edfors for his constant eagerness for discussions and never-ceasing desire to understand underlying mechanisms. Lastly, I want to thank my channel-measuring friends and colleagues Telmo Santos, Shurjeel Wyne and Dr. Peter Almers for priceless discussions. I would never have made it this far without you.

My friends and colleagues within the areas of Radio Systems and Signal Processing research deserve my sincere thanks: Dr. Anders J Johansson, Dr. André Stranne, Andrés Alayon, Dr. Buon Kiong Lau, Farzad Foroughi, Dr. Fredrik Florén, Fredrik Harrysson, Frida Sandberg, Gunnar Eriksson, Jianjun Chen, Martin Stridh, Palmi Thor Thorbergsson, Peter Hammarberg and Ulrike Richter. Going to work wouldn't be the same without you.

Many thanks go to the technical and administrative staff at the department, especially Lars Hedenstjerna, for his excellent mechanical solutions, Birgitta Holmgren and Pia Bruhn for always being helpful with my various queries, and

Erik Jonsson for helping me out with computer matters.

I also want to acknowledge the sponsors of my PhD studies, an INGVAR grant of the Swedish Strategic Research Foundation (SSF), the SSF Center of Excellence for High-Speed Wireless Communications (HSWC) and a grant from the Swedish Science Council (Vetenskapsrådet).

My endless gratefulness goes to my family, for loving and supporting me in everything I do – my father Jan, my mother Agneta and my sister Maria. Finally, thank you Monica. For always being there, for your unconditional love and support, and for being the mother of our beloved daughter Sigrid.

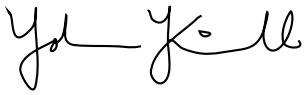

Johan Kåredal

List of Acronyms and Abbreviations

AOA Angle-Of-Arrival

AOD Angle-Of-Departure

APDP Average Power Delay Profile

BLAST Bell labs LAyered Space-Time

BP BandPass

CDF Cumulative Distribution Function

CDMA Code Division Multiple Access

COST COoperation européenne dans le domaine de la recherche Scientifique et Technique

CSI Channel State Information

DSP Digital Signal Processing

EIRP Effective Isotropic Radiation Pattern

FCC Federal Communications Commission

FFT Fast Fourier Transform

GP Guard Period

GSCM Geometry-based Stochastic Channel Model

IEEE Institute of Electrical and Electronics Engineers

IFFT Inverse Fast Fourier Transform

i.i.d. Independent and Identically Distributed

ISI Inter-Symbol Interference

ISM Industrial Scientific and Medical

LOS Line-Of-Sight

MAGNET My personal Adaptive Global NET

MIMO Multiple-Input Multiple-Output

ML Maximum Likelihood

MLE Maximum Likelihood Estimate

MPC MultiPath Component

MRC Maximum Ratio Combining

MSE Mean Squared Error

NLOS Non-Line-Of-Sight

OFDM Orthogonal Frequency Division Multiplexing

OOK On-Off Keying

PAM Pulse Amplitude Modulation

PAN Personal Area Network

PDF Probability Density Function

PDP Power Delay Profile

PPM Pulse Position Modulation

RF Radio Frequency

RMS Root Mean Square

RX Receiver

SER Symbol Error Rate

SISO Single-Input Single-Output

SNR Signal-to-Noise Ratio

SV Saleh-Valenzuela

TH-IR Time-Hopping Impulse Radio

TX Transmitter

ULA Uniform Linear Array

UWB Ultra-WideBand

VNA Vector Network Analyzer

WLAN Wireless Local Area Network

WSSUS Wide-Sense Stationary Uncorrelated Scattering

Contents

Part I

Overview of the Research Field

Chapter 1

Introduction

Ever since Marconi's first experiments in the late 1800s, there has been a big interest in the possibilities of wireless communications. Since then, wireless links have gone from only being capable of unreliable and low-rate transmissions to the high-capacity networks we see today. The fields of applications are numerous: Voice services are so established that they often may replace fixed line services, wireless local area networks are up and running in many residential, office, municipal or school buildings, and personal area networks, e.g., Bluetooth links, form wireless connections between various consumer electronics devices. Nevertheless, there is a seemingly constant urge for improving the capabilities of wireless communications in terms of throughput and/or reliability, and there is a variety of new applications and environments for which wireless technology is envisioned. However, while the number of wireless applications continues to grow, bandwidth is still as limited a resource as in the days of Marconi.

The limitation in available bandwidth has motivated the development of novel transmission techniques, out of which two that have gathered a lot of research interest in recent years are multiple-input multiple-output (MIMO) systems and ultra-wideband (UWB) systems. Employing several antenna elements at both sides of the radio link, MIMO systems make use of the *spatial* domain to increase the system performance, by using transmissions coded across both time and space. Such codes can be realized in a variety of ways, with different codes achieving diversity gain, array gain or multiplexing gain. Even though the name of MIMO in fact only implies the usage of multiple antenna elements at both link ends, it is often intimately associated with the concept of spatial multiplexing. This is also the reason behind most of the attention given to MIMO systems, since spatial multiplexing, at least in theory, can provide a

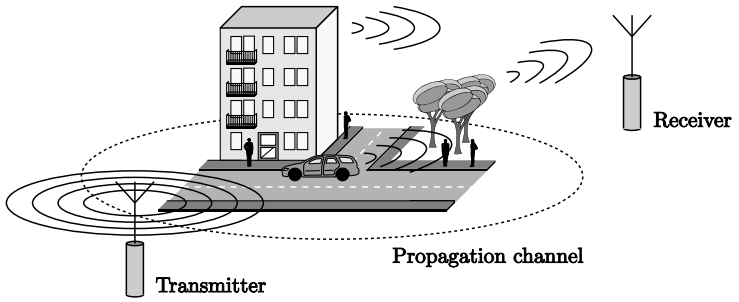

Figure 1.1: The wireless propagation channel.

capacity that increases linearly with the number of antenna elements.

The UWB concept relies on unlicensed use, i.e., with no frequency resources uniquely allocated to UWB transmissions. Instead UWB systems are intended to *coexist* with existing services. The core idea is to spread the information over a huge bandwidth, such that the power spectral density is so low that the transmission is perceived as noise to other systems. Research interest received a major boost in 2002 when the US frequency regulator allowed the unlicensed use of UWB systems over a frequency range specified by spectral masks, and since then UWB systems have been envisioned for numerous applications. Subsequently, the increasing interest led to the forming of two IEEE task groups, 802.15.3a and 802.15.4a, dedicated to developing standards for such systems.

In the context of promising technologies such as MIMO and UWB, it is well-known that the development of any wireless system requires knowledge about the propagation environment in which it is intended to be used. For an optimal system design, transmission (and reception) techniques, such as different space-time codes for MIMO systems, need to be evaluated under realistic conditions since their performance is highly dependent on the conditions of the wireless propagation channel. The wireless propagation channel (often referred to as only "the channel") is the medium linking the transmitter and receiver in a wireless system (see Fig. 1.1) and the research field of channel modeling aims at providing the means for describing and emulating the channel in terms of certain quantities. Even though channel modeling itself is not a new field of research, the concepts of MIMO and UWB imply new effects that need to be characterized. In this thesis, we provide insight into the MIMO and UWB characteristics by focusing on *measurement-based* modeling of the wireless propagation channels. Measurement-based modeling basically consists of three steps: collecting channel samples through field measurements, analyzing the channel in order to understand the reasons behind important effects, and,

usually stochastically, providing a model description that can reproduce the same properties.

The subsequent chapters of Part I give a further introduction to the contributions of this thesis. Chapter II contains an overview of the fundamentals of MIMO and UWB systems, whereas Chapter III describes the wireless propagation channel, common approaches of general channel modeling as well as modeling issues specific to MIMO and UWB systems. Chapter IV describes principles for measurements of the propagation channel, and finally, Chapter V summarizes the contributions of the included papers and gives some general conclusions regarding my work.

Chapter 2

Two Promising Wireless Systems

Bandwidth is a resource that is essential for any wireless communications system. However, with numerous wireless links for military applications, meteorological applications, satellite communications, radioastronomy etc. simultaneously in operation, frequency regulations are strict and the amount of available bandwidth is very limited, and therefore also expensive. This has sparked the research interest in wireless communications systems that can utilize other means than additional bandwidth allocation and still provide a high system performance. Two such promising techniques are MIMO systems and UWB systems. Whereas the former provides a solution for the increased throughput by usage of the spatial domain, the latter is intended to coexist with already existing wireless services, by reusing the same frequency bands. This chapter gives an overview of the principles behind these two techniques.

2.1 Multiple-Input Multiple-Output Systems

Despite the fairly recent breakthrough of MIMO, the interest in wireless systems that make use of multiple antennas is by no means new. H. H. Beverage and H. O. Petersen investigated the received signals at different antennas already in the early 1920s [1] and D. G. Brennan did theoretical investigations on diversity combining in the 1950s [2]. The interest in the usage of multiple antennas at *each* end of the radio link originally started with the paper by Winters in 1987 [3], followed by theoretical investigations by Foschini and Gans [4] and Telatar [5] in the late 1990s.

Multiple antenna elements can be exploited in three different ways; for diversity, beamforming or spatial multiplexing. These transmission schemes are collected under the name space-time coding [6] (further separated into space-time block codes and space-time trellis codes) and different codes provide different gains. Depending on the array configuration and what space-time code that is applied, array gain, diversity gain, multiplexing gain or combinations thereof can be achieved. The following sections briefly cover the key elements of the different ways of space-time transmissions; more thorough descriptions are given in, e.g., [6], [7] and [8].

2.1.1 Diversity

Under most conditions, the received signal of a wireless system consists of the superposition of delayed and attenuated replicas of the transmitted signal and the effects of constructive or destructive summation of these waves is referred to as fading. When the received signal power drops below some level, the channel is said to be in a fade, or in a fading dip, and fading can significantly degrade the performance of a wireless system. Diversity techniques are applied as a means to combat fading and increase throughput by lowering the variations of the received signal-to-noise ratio (SNR) which in turn reduce the average symbol error rate (SER) for a given average SNR. Though mentioned here in the context of multiple antenna systems, diversity techniques are not at all limited to the spatial domain; separate or joint diversity can be achieved by using (and possibly combining) the spatial, frequency, temporal or polarization domain.

Depending on the amount of channel state information (CSI), different diversity schemes can be applied. Well-known examples of receive diversity techniques include antenna selection schemes (see e.g., [9]) and the maximum ratio combining (MRC) scheme, where a receiver with CSI can add up the signals received at the different antenna elements coherently [2]. With CSI at the transmitter, it too can apply the MRC principle, which is often referred to as maximum ratio transmission. There are also transmit schemes that can achieve diversity even without CSI, e.g., using space-time block codes such as the Alamouti scheme [10].

2.1.2 Array Gain

Beamforming techniques, also known as smart antennas, steer the beam pattern of the antenna array into the directions of incoming multipath components (MPCs). Whereas diversity gain is obtained in terms of an improved *slope* of the SER vs. SNR curve, array gain gives an increase in the *average* received

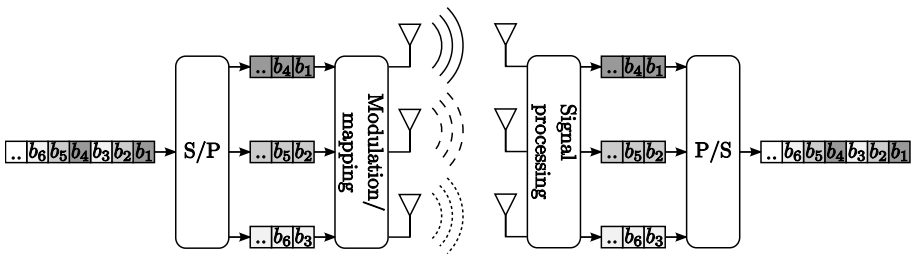

Figure 2.1: The concept of spatial multiplexing (vertical BLAST) for a 3×3 MIMO system. A bit stream $b_1, b_2, b_3, \ldots$ is serial-to-parallel (S/P) converted into three substreams, each transmitted from a single antenna element. At the receiver, the substreams are recovered and parallel-to-serial (P/S) converted back to the original sequence.

SNR. The maximum ratio combining scheme described above gives an array gain (equal to the number of antennas), whereas the Alamouti scheme does not. Optimal performance is achieved if transmitter *and* receiver have CSI, since both can perform maximum ratio combining and thus array gain is obtained at each side of the link. This is often referred to as dominant eigenmode transmission [6].

2.1.3 Spatial Multiplexing

Spatial multiplexing is the newer concept of multiple antenna usage and has thus attracted the highest interest in recent years. This stems from the fact that under beneficial channel conditions, the transmission rate may be increased linearly with the number of antenna elements in use. The basic concept of spatial multiplexing is to transmit multiple data streams simultaneously by dividing (or multiplexing) the data stream to be transmitted into several substreams, as demonstrated by the BLAST transmission schemes [11] (see Fig. 2.1). Since each transmit signal is given a separate spatial signature from the channel, it is possible for the receiver to distinguish between the different signals if it has channel knowledge, and the MIMO channel can then be seen as a number of parallel spatial sub-channels.

Before the year 2000, the research focus was mainly from an information theoretical point of view. Since then interest has shifted somewhat to investigations of what realistic throughputs that can be obtained. In this context, measurements are needed to answer questions regarding the channel conditions. This is also the motivation for the measurements of the included papers I-III,

where the propagation channels for some envisioned future MIMO applications are characterized. Papers I and II study propagation channels for wireless Personal Area Networks (PANs), which are short-range networks that typically consist of communication between small, handheld (or in other ways body-close) consumer electronics devices. PAN channels are especially interesting since human presence can have important consequences for the signal quality. Paper III characterizes the behavior of MIMO links between vehicles. Such channels are of particular interest since they usually involve very high mobility of both terminals as well as important interacting objects in the channel.

The benefits of spatial multiplexing can be reaped without CSI at the transmitter. The narrowband MIMO link with M receive elements and N transmit elements can be expressed as a linear system with input $\mathbf{s} \in \mathbb{C}^{N\times 1}$ and output $\mathbf{y} \in \mathbb{C}^{M\times 1}$ by

$$\mathbf{y} = \mathbf{H}\mathbf{s} + \mathbf{n}, \tag{2.1}$$

where $\mathbf{n} \in \mathbb{C}^{N\times 1}$ is zero mean circularly symmetric complex Gaussian noise and $\mathbf{H} \in \mathbb{C}^{M\times N}$ is the channel transfer function. In can be shown [5], that the capacity of a MIMO system is given by

$$C = \max_{\mathrm{Tr}(\mathbf{R_{ss}})} \left\{ \log_2 \det \left(\mathbf{I}_M + \frac{\rho}{N} \mathbf{H}\mathbf{R_{ss}}\mathbf{H}^H \right) \right\}, \tag{2.2}$$

where $\mathbf{I}_M$ is the identity matrix of size M, $\mathbf{R_{ss}}$ is the covariance matrix of $\mathbf{s}$, $\mathrm{Tr}(\cdot)$ denotes the trace of a matrix, $\{\cdot\}^H$ denotes Hermitian transpose and ρ is the mean SNR per receiver branch. In the case of no CSI at the transmitter, the transmitter may choose the vector $\mathbf{s}$ without preference, i.e., allocating equal power to all branches such that $\mathbf{R_{ss}} = \mathbf{I}_N$, in which case the MIMO channel capacity becomes

$$C = \log_2 \det \left(\mathbf{I}_M + \frac{\rho}{N} \mathbf{H}\mathbf{H}^H \right). \tag{2.3}$$

Rewriting $\mathbf{H}\mathbf{H}^H = \mathbf{Q}\mathbf{\Lambda}\mathbf{Q}^H$, where $\mathbf{Q}^H\mathbf{Q} = \mathbf{I}_M$, the capacity of (2.3) can be reduced to

$$C = \log_2 \det \left(\mathbf{I}_M + \frac{\rho}{N} \mathbf{\Lambda} \right) \tag{2.4}$$

or

$$C = \sum_{i=1}^{r} \log_2 \left(1 + \frac{\rho}{N} \lambda_i \right), \tag{2.5}$$

where r is the rank of the channel matrix and λ_i are the (positive) eigenvalues of $\mathbf{H}\mathbf{H}^H$. In this way, the MIMO capacity can be expressed as the sum of the capacities of r single-input single-output (SISO) channels, each with a power gain λ_i. The eigenvalues λ_i are used as a comparative metric in paper II.

In the context of random (fading) MIMO channels, the capacity is a random variable. It is therefore common to use two statistics for analysis of the capacity: ergodic capacity and outage capacity [4]. The ergodic capacity, $\overline{C}$, is defined as the average over an ensemble of values, i.e.,

$$\overline{C} = E_{\mathbf{H}} \left\{ \log_2 \det \left(\mathbf{I}_M + \frac{\rho}{N} \mathbf{H}\mathbf{H}^H \right) \right\}, \tag{2.6}$$

where $E_{\mathbf{H}}\{\cdot\}$ denotes the expectation taken over a number of channel realizations. Outage capacity, on the other hand, is a measure of the capacity that guarantees a certain performance (the capacity that is exceeded a certain percentage of time).[1] The ergodic capacity measure is used as a performance metric for the proposed model in paper II.

The optimal transmission scheme can be applied if also the transmitter has CSI. If so, the waterfilling scheme, where power is allocated to the spatial subchannels according to their respective strength, can be applied which results in an optimal covariance matrix $\mathbf{R}_{\mathbf{ss}}^{\text{opt}}$. Further information about waterfilling can be found in, e.g., [7].

2.2 Ultra-Wideband Systems

In principle, pulse-based transmission goes as far back as Marconi's first experiments with spark gap transmitters in 1894–1896 [12]. In 1901, Sommerfeld performed analysis for an initial understanding of the UWB pulse propagation when he investigated the diffraction of a time-domain pulse by a perfectly conducting wedge [13]. However, up until recent years continuous-wave transmission has been commercially favored due to limits in technology as well as demands for more reliable communications, and pulse-based transmission was for a long time-period relegated to military research (mostly confined to radar applications) [14]. Important work was done by Win and Scholtz in the 1990s [15], [16], [17], and the major break-through in UWB communications came in 2002 when the United States frequency regulator, the FCC, issued a Report and Order that allowed the unlicensed transmission within specified spectral masks for indoor and outdoor communications [18] (see Fig. 2.2).

The concept of UWB relies on spreading the transmitted information over extremely large bandwidths. The FCC defines UWB as having an absolute bandwidth of more than 500 MHz or a fractional bandwidth (average bandwidth over center frequency) of more than 20%. The bandwidth implies that

[1] Strictly speaking, outage capacity is an approximate concept, because "capacity" theoretically requires the transmission of infinitely long code blocks. For "outage capacity," one thus assumes that "sufficiently large" code blocks can be transmitted in a time during which the channel is constant.

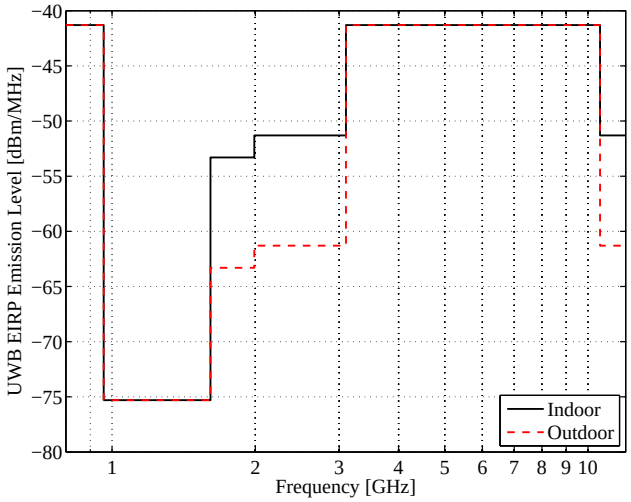

Figure 2.2: The spectral masks for indoor and outdoor UWB transmission defined by the FCC.

the power spectral density of the transmitted signal can be extremely low, such that a UWB system can coexist with other existing wireless services to which it will be perceived as noise, i.e., slightly increasing the noise floor.

2.2.1 UWB Physical Layer

The FCC provides power spectra, but does not prescribe any signals for UWB systems (though certain types of signals, such as slow frequency hopping, are excluded by their rulings). While the original ideas revolved around pulse-based transmission, other realizations of UWB in terms of regular carrier-based systems are possible as well. This led to two competing proposals for the UWB physical layer in the high-data-rate transmission standard IEEE 802.15.3a: a direct-sequence code division multiple access (CDMA) proposal, and a multiband proposal, usually suggested in the context of using orthogonal frequency division multiplexing (OFDM) in combination with frequency hopping. The direct-sequence approach faded when its main proponent, Xtreme Spectrum/Freescale, stopped manufacturing it. The multiband approach, while it never became an IEEE standard, was ultimately adopted by Ecma and the WiMedia alliance.

Pulse-based UWB, often referred to as *impulse radio*, is based on transmitting very short pulses (on the order of a few hundred picoseconds) where

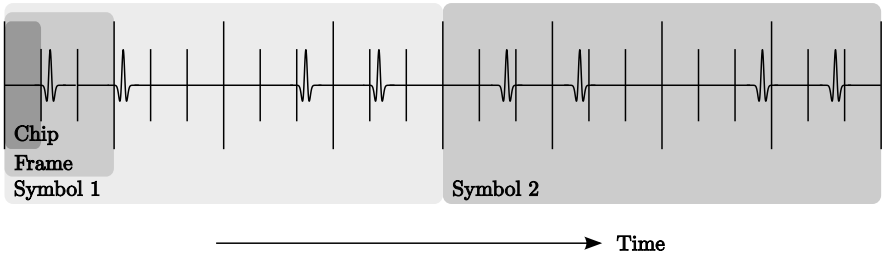

Figure 2.3: The concept of time-hopping impulse radio visualized through an example of a binary PPM pulse train. Different users are controlled by the pulse position within the frame, whereas the pulse position within the chip is used to represent different symbols.

a transmitted symbol usually is represented by a sequence of pulses through a repetition code in order to increase robustness. To account for multiaccess interference, the concept of time-hopping impulse radio (TH-IR) relies on transmitting such pulse trains, where each symbol time is divided into a number of *frames* and each frame further divided into a number of chips. Then, multiple access is enabled by assigning different spreading codes for different users, such that the positions within the frames identifies the user. Additionally, since the regular structure of such pulse trains gives undesirable spectral qualities, techniques such as random dithering can be applied in order to shape the spectrum of the signal and comply with the FCC masks. Several modulation methods have been suggested for TH-IR, e.g., on-off keying (OOK), pulse amplitude modulation (PAM) or pulse position modulation (PPM) (Fig. 2.3 shows an example of a PPM pulse train).

In multiband UWB, the overall bandwidth is divided into subbands of at least 500 MHz, and the baseband signals are modulated onto carrier frequencies. Being often mentioned in the context with OFDM, multiband UWB is not as novel a concept as impulse radio. It has, however, appealing benefits in terms of spectrum flexibility such that non-intentional interference can be avoided in certain bands using nulling of subcarriers. This also simplifies coexistence with other systems, which is especially suitable for UWB services in locations where UWB transmission on a detect-and-avoid basis is mandatory.

2.2.2 Applications and Industrial Standards

UWB communications are envisioned for high-data-rate as well as low-data-rate applications. For high data rates, it is often suggested as a cable replacement for streaming multimedia content between consumer electronics devices. As

such, it constitutes a possible wireless solution to applications where existing standards such as Bluetooth or regular local area networks (i.e., the IEEE 802.11 standards) have not succeeded so far [12]. The increasing interest in the performance of such applications motivated a need for characterization of the wireless propagation in the appropriate environments, which was the reason behind many UWB measurement campaigns in residential and office environments. Our included paper IV is also along those lines, where we investigate the propagation environment within the chassis of desktop computers. The main conclusion of the paper concerns the interference produced by the computer circuitry, which due to its band-limited nature suggests that multiband UWB is better suited for this particular type of applications.

For low data rates, UWB systems are often associated with wireless sensor networks, possibly with positioning capabilities, which is very appealing given the fine delay resolution of UWB. The low transmit power is another quality that make UWB an attractive technique for sensor networks. Sensor networks may include control of home appliances, search-and-rescue applications for avalanche or earthquake victims, logistics (e.g., package tracking), security applications or industrial control applications.

Up until this date, two industrial standards have been developed for UWB communications, the IEEE 802.15.3a and IEEE 802.15.4a. The 802.15.3a task group was formed in 2001 in order to develop a multiband UWB standard for high data rates. While this standard ultimately failed, the multiband approach was later standardized by Ecma. IEEE 802.15.4a, whose task group was formed in 2004, is intended for low data rate UWB systems, especially with sensor networks in mind. When this standard was developed, it could not directly apply the propagation model of 802.15.3a since this accounted for far less propagation environments than the 802.15.4a standard was intended to cover. Hence several new measurement campaigns were required. One of the new propagation environments that were to be characterized in the development of the standard was industrial environments. Our included paper V was the first to describe measurements in such environments, and partial results of the paper were used as input to the propagation model of IEEE 802.15.4a (see [19]).

Chapter 3

Modeling Wireless Propagation Channels

A transmitter is linked to the receiver through the wireless propagation channel. Since channel conditions can have a major impact on the performance of a wireless system, channel knowledge is obviously vital in the system design process.

A channel may consist of a large number of propagation paths conveying the transmitted signal to the receiver, where different paths undergo one or several propagation mechanisms: free-space attenuation, transmission, reflection, diffraction and scattering. The channel characteristics are determined by the interaction of such paths and the art of channel modeling is to describe these effects in a compact and efficient manner. In this chapter, we describe different approaches for modeling the wireless channel, first in a general sense, then by studying some important aspects on SISO modeling. Finally, we discuss channel models for MIMO and UWB systems.

3.1 Channel Modeling Approaches

By providing a realistic means for testing and analysis of system performance in the design process, channel models that can accurately describe the propagation channel are essential for the planning of wireless systems. In this context, channel modeling always implies a trade-off. On one hand the model should be as accurate as possible, on the other there is a desire for simplicity in order to make the model easy to use. Channel modeling can be performed in a variety of ways, with different complexity level for different approaches. Several

classifications of modeling approaches can be made, though there is an overlap between classes. One can, e.g., distinguish between narrowband and wideband models, stochastic and deterministic models, non-physical and physical models, and measurement-based and scatterer models [20].

3.1.1 Deterministic vs. Stochastic Channel Modeling

The most exact deterministic channel modeling approach relies on solving Maxwell's equations under the boundary conditions imposed by a specific environment, thus requiring information about the location, shape, and electromagnetic properties of every object in the propagation environment. An analytical solution is obviously not a straightforward approach, so typically solutions are derived using approximative methods like the finite-difference time-domain (FDTD) method [21] or the finite-element method (FEM) [22]. Even so, calculations are demanding and solutions require a lot of computational power which limits the usefulness of such methods. The intensive calculations also make it difficult to vary parameters and these methods thus cannot be easily used for extensive system-level simulations of communications systems. Another, more common approximative deterministic method is the so-called raytracing method (see e.g., [23], [24], [25]) where rays are launched from the transmitter, and their respective paths to the receiver determined from geometric optics including all fundamental propagation mechanisms. Raytracing methods can produce very accurate results (see e.g., [26]), though their main drawback, even though the method being simplified, lies in the computational efforts. Deterministic methods are mainly used for the deployment of cellular systems, so that coverage can be tested for specific deployment options.

Stochastic channel models provide the statistics of the received power by predicting the probability density function (PDF) of parameters such as delay, Doppler shift, pathloss etc. Ideally, such models provide a means of investigating the impact of a certain parameter, which is a benefit compared to using pure measurement data for system analysis.[1] A special category of stochastic channel models are the geometry-based stochastic channel models (GSCMs) [27], [28], which assign positions and properties to scatterers stochastically and perform a simplified ray-tracing before summing up the contributions at the receiver. GSCMs are especially useful for non-stationary environments, as they can easily model motion of transmitter, receiver and/or scatterers [29], [30]. All channel modeling in this thesis is stochastic.

[1] Using pure measurement data may also incorporate problems of including measurement noise. Ideal channel models describe the noise-free channel

3.1.2 Narrowband vs. Wideband Channel Modeling

Narrowband channel models assume that the system bandwidth is (much) smaller than the coherence bandwidth of the channel, and thus that the channel response is the same over the whole system bandwidth. If the situation is reversed, i.e., the coherence bandwidth is smaller than the system bandwidth, the channel is frequency selective, and the channel response is different for different frequencies. Frequency selectivity implies that the channel is delay dispersive, i.e., a (finite-time-support) signal will arrive at the receiver over a longer time period than over which it was transmitted. Wideband channel modeling can be performed either in the frequency domain or the delay domain, though the latter approach, where the channel impulse response $h(t, \tau)$ is modeled, is by far the most common.

3.1.3 Non-Physical vs. Physical Channel Modeling

Non-physical models, also referred to as analytical models, characterize the channel in terms of capturing certain *effects* rather than explicitly relying on wave propagation. Several analytical MIMO models exist, as will be discussed later. Models that use a realistic (to some degree) geometric scattering environment as their basis are referred to as physical models.

3.1.4 Scatterer vs. Measurement-Based Channel Modeling

Scatterer models postulate a model, by distributing scatterers, in order to capture the channel characteristics. The model still needs to be verified against measurement data, but measurements serve as a verificative measure, rather than a source of inspiration for the modeling strategy. The reversed strategy applies for measurement-based models, that are based on channel data, from which important channel characteristics are derived and a model capable of reproducing the same characteristics is created. Measurement-based modeling is the focus of this thesis.

3.2 SISO Channel Modeling

The time-varying wireless channel is typically modeled through its complex channel transfer function $H(t, f)$ or corresponding complex channel impulse response $h(t, \tau)$. Besides modeling temporal and delay/frequency properties, there are three main propagation effects that are of interest for the SISO link: (Large-scale) pathloss, large-scale fading (shadowing) and small-scale fading.

3.2.1 Pathloss

Pathloss models predict the expected average level of receiver power for a given transmitter-receiver separation d. The received power, P_{RX}, is usually described by a power law, i.e.,

$$P_{RX}(d) = P_{RX}\left(d_{\text{ref}}\right) - 10n \log_{10} \frac{d}{d_{\text{ref}}}, \tag{3.1}$$

where $P_{RX}\left(d_{\text{ref}}\right)$ is the received power at a reference distance d_{ref}, typically determined through reference measurements [31]. The pathloss exponent n is a model parameter that depends on the particular environment, and thus commonly supplied in modeling papers. It is therefore important to note that the measurement setup can have an influence on the parameter estimate. Two effects apply: the measurement range and the measurement sampling grid.

The measurements range should be large enough for local large-scale variations (such as shadowing effects) not to have an influence on the estimation process. Achieving this is, however, not always feasible, especially for indoor measurement campaigns where the building structure often sets the limit. This issue relates to the included paper III, where we characterize the signal contributions from individual scatterers by a distance decay. Since our observation window is limited (usually over a few hundred meters), we only estimate pathloss exponents from signals visible over a *relative* distance range (absolute range over mean propagation distance) larger than 0.2.

To show the influence of the distance sampling grid, we make use of measurement data from a line-of-sight (LOS) scenario in a corridor. The transmitter (TX) was located in one end of a corridor and channel samples were recorded every meter by moving the receiver (RX) along the corridor. Both TX and RX were equipped with multiple, horizontally polarized, antenna elements and the frequency range was 2.6 ± 0.1 GHz. The small-scale averaged (over TX and RX antenna elements) received power is shown in Fig. 3.1. A common approach to estimate the pathloss exponent n is by simple regression analysis of $10 \log_{10}(d)$ to the measured, dB-valued, power values [32], i.e., by minimizing the mean squared error (MSE) between the measured and modeled samples such that

$$\left\{\hat{n}, \hat{P}_0\right\} = \underset{n, P_0}{\arg\min} \sum_i \left(P_0 + 10n \log_{10} d_i - P_i\right)^2, \tag{3.2}$$

where P_i is the received power measured at a distance d_i. Applying (3.2) to the data in Fig. 3.1 gives $\hat{n} = 0.67$. However, due to the higher concentration of samples at large *logarithmic* distances, this estimate constitutes a better predictor for larger rather than smaller distances. To improve the predictability of the model for small d, one can apply another estimation approach where the

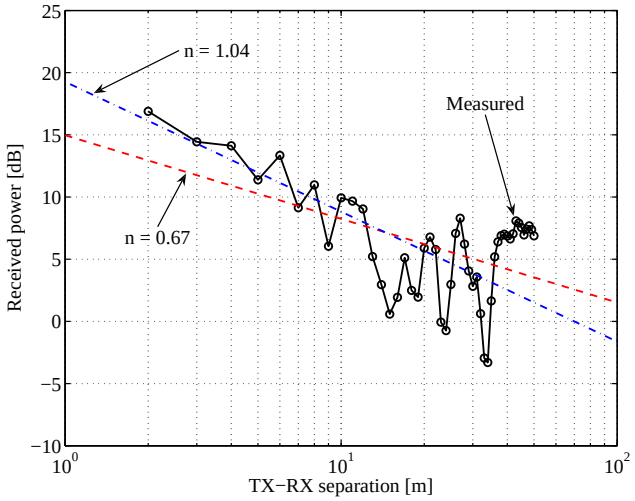

Figure 3.1: Small-scale averaged received power in a LOS corridor scenario along with two different estimates of the pathloss exponent.

MSE between measurement and model, for each sample, is weighed according to the logarithmic sampling density, i.e.,

$$\left\{\hat{n}, \hat{P}_0\right\} = \arg\min_{n,P_0} \sum_i \left(P_0 + 10n \log_{10} d_i - P_i\right)^2 \log_{10} \frac{d_{i+1}}{d_i}. \tag{3.3}$$

This renders $\hat{n} = 1.04$, which provides a better fit for small TX-RX separations (see Fig. 3.1) and only a slightly larger deviation for the higher range. However, our point here is not to suggest one estimation method over the other (that is more a matter of preference), but rather to show that different sampling grids give the same *effect* as different estimation methods.

3.2.2 Large-Scale Fading

Large-scale fading, or shadowing, describes the variations of the small-scale averaged received signal power at a given distance. The ideal way of measuring shadowing would thus be to perform a large set of measurements for every TX-RX separation d, and study the statistics. However, since such a procedure is very time-consuming, few measurements have been performed in this way. Rather, shadowing is defined as the variations of the small-scale averaged power around the distance-dependent decay, i.e., the residue power variations once the

distance dependence has been subtracted. Shadowing is commonly included in the pathloss equation (3.1) by

$$P_{RX}(d) = P_{RX}(d_{\text{ref}}) - 10n \log_{10} \frac{d}{d_{\text{ref}}} - X, \tag{3.4}$$

where $X \sim \mathcal{N}(0, \sigma_X)$ is the dB-valued shadowing loss and σ_X^2 the shadowing variance [32]. The undesired effect of this procedure is that the shadowing variance is sensitive to the estimation of the pathloss exponent, since the latter procedure often is performed first. With different estimates $\hat{n}$ thus leading to different estimates $\hat{\sigma}_X^2$, this puts further importance to proper choices in the measurement setup.

Shadowing is typically associated with variations in the environment. However, human presence in the channel, especially close to the antennas, leads to the same effect and is referred to as body shadowing. Once human bodies are included at one or both sides of the link, the position of the body, relative the position of the other side of the link, will greatly affect the shadowing situation. Variations in signal power may thus occur not only by lateral movement, but also by rotation of the user and/or movement of the antennas with respect to the body. This issue is addressed in the included paper I, where we study the influence of body shadowing for wireless PANs. By equipping two persons with (small-size) antenna arrays, and performing measurements with different rotations of these persons, we find it preferable to distinguish between two types of shadowing: shadowing due to the environment and body shadowing (see Fig. 3.2). We thus extend (3.4) to

$$P_{RX}(d) = P_{RX}(d_{\text{ref}}) - 10n \log_{10} \frac{d}{d_{\text{ref}}} - L_e - L_b, \tag{3.5}$$

where $L_e \sim \mathcal{N}(0, \sigma_e)$ and $L_b \sim \mathcal{N}(0, \sigma_b)$ are the dB-valued losses due to shadowing from the environment and body shadowing, respectively.

3.2.3 Small-scale Fading

Small-scale fading is caused by the constructive and destructive interference of multipath components impinging at the receiver. Typically occurring during movements of a terminal over one or a few wavelengths, small-scale fading thus gives variations around the large-scale signal level. Though there exist joint distributions that can describe the combined effects of large-scale and small-scale fading (e.g., the Suzuki distribution [33]), the more common approach is to give separate PDFs for the two.

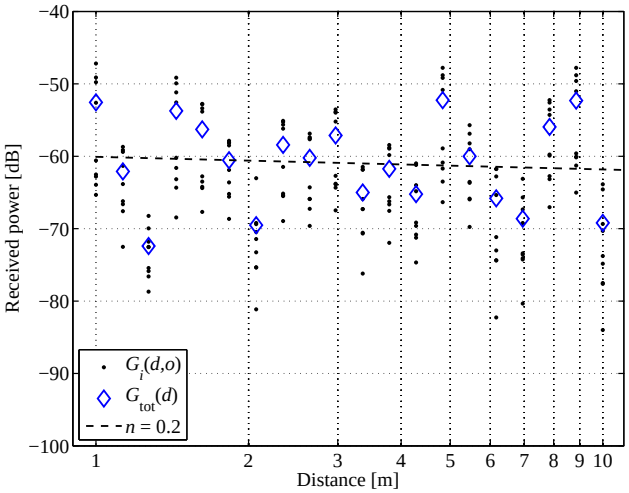

Figure 3.2: Scatter plot of the received power vs. propagation distance for a 5.2 GHz PAN LOS measurements. Dot markers represent (small-scale averaged) power for different rotations of the test persons, thus implying different amounts of body shadowing. Diamond markers represent the average power over all rotations. (From included paper I.)

There are several distributions that have been proposed to describe the small-scale variations of the signal envelope r, with different distributions having been found suitable for different wireless systems and propagation environments. The by far most frequently used model is the Rayleigh distribution, whose PDF

$$p(r) = \frac{r}{\sigma^2} \exp\left\{-\frac{r^2}{2\sigma^2}\right\}, \tag{3.6}$$

stems from a signal that is zero-mean complex Gaussian with a standard deviation σ, as motivated by the central limit theorem (CLT) [31]. The zero-mean makes this distribution useful for non-line-of-sight (NLOS) situations. For LOS situations, where the received signal has a *non-zero* mean, the dominant component renders an envelope PDF instead being described by the Ricean distribution

$$p(r) = \frac{r}{\sigma^2} \exp\left\{-\frac{r^2 + A^2}{2\sigma^2}\right\} I_0\left(\frac{Ar}{\sigma^2}\right), \tag{3.7}$$

where I_0 is the zero-order modified Bessel function of the first kind and A is the amplitude of the dominant component. Usually, the Ricean distribution is

described by the Ricean K-factor, defined as

$$K = \frac{A^2}{2\sigma^2}, \tag{3.8}$$

and (3.7) can then be rewritten as

$$p(r) = \frac{2(K+1)r}{\Omega} \exp\left(-K - \frac{(K+1)r^2}{\Omega}\right) I_0\left(2\sqrt{\frac{K(K+1)}{\Omega}}r\right), \tag{3.9}$$

where $\Omega = E\left\{r^2\right\}$ is the mean power [34]. With no dominant component, $K = 0$ and (3.7) or (3.9) reduces to the Rayleigh PDF. The K-factor is a parameter frequently studied in modeling papers, such as the included papers I and II.

The above distributions are the most popular to describe the amplitude statistics for narrowband or wideband wireless systems. There are situations, however, when these descriptions are insufficient. Such a situation is addressed in the included paper I, where we study how the small-scale statistics are influenced by human presence in wireless PANs. The terminals we use in the study are intended to resemble real body-close applications in terms of handheld and bodyworn devices and are equipped with antenna arrays that have an irregular structure, i.e., their elements have different antenna patterns. Since the person carrying the device essentially becomes a part of the antenna, the combined antenna pattern is sensitive to changes in the relative position between the body and the antenna devices and we find that this results in amplitude statistics that can alternate between being Ricean or Rayleigh distributed (i.e., the estimated K-factors show large variations). The statistical ensemble over a small time frame thus contains a mixture of Ricean and Rayleigh samples, and we find that a mixed distribution, the generalized gamma distribution [35]

$$p(r) = \frac{cr^{c\alpha-1}}{\beta^{c\alpha}\Gamma(\alpha)} \exp\left[-\left(\frac{r}{\beta}\right)^c\right], \tag{3.10}$$

where $\Gamma(x)$ is the gamma function, constitutes a suitable model for the amplitude statistics. α, β and c thus become the model parameters of interest. It is noteworthy that the generalized gamma distribution contains both the Rayleigh and the Ricean distributions as special cases.[2]

3.2.4 Temporal and Wideband Characterization

A common approach for wireless stochastic modeling is the wide-sense stationary uncorrelated scattering (WSSUS) assumption [36]. The WSS part implies

[2]Strictly speaking, it only constitutes a good approximation of the Ricean distribution [35].

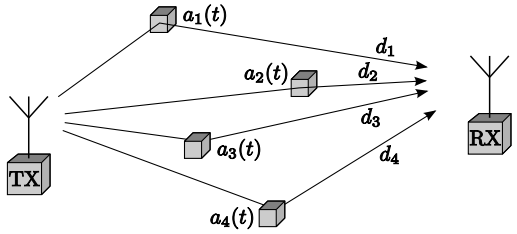

Figure 3.3: The principle of a multipath channel. $N = 4$ multipath components are arriving at the receiver with delays $\tau_i = d_i/c$, where c is the speed of light.

that the channel *statistics* must not change over time and that the temporal auto-correlation function of the channel is only dependent on the lag, i.e., not on the particular time instant considered.[3] This also requires a constant Doppler spectrum over time. The US part implies that each tap of the impulse response fade independently.

Temporal characterization thus requires modeling of the frequency dispersion, i.e., modeling of the Doppler Spectrum (or alternatively the temporal autocorrelation function). Several methods for modeling a Rayleigh-fading channel with a constant Doppler spectrum (often the Jakes spectrum [37]) exist in the literature, e.g., [38].

Wideband modeling describes the delay dispersion of the channel. Delay dispersion, where a signal will arrive over a longer duration than over which it was transmitted, is caused by the interaction between objects and the transmitted signal in a frequency-selective channel. Since it is the reason behind inter-symbol interference, a proper understanding and modeling of the delay dispersion is vital for the effective design of wireless systems. As previously mentioned, wideband characterization is commonly made in the delay domain. If the channel fulfills the WSSUS condition, it can be represented by a tapped-delay line, i.e., the complex channel impulse response $h(t, \tau)$ is given by a sum of N multipath components arriving with different delays at the receiver such that

$$h(t, \tau) = \sum_{i=1}^{N} a_i(t)\delta(\tau - \tau_i), \tag{3.11}$$

where $a_i(t)$ is the time-varying complex amplitude of the ith component arriving at a delay τ_i (see Fig. 3.3).

[3]The constant channel statistics should however not be confused with the definition of a static channel.

3.3 MIMO Channel Modeling

Most SISO modeling approaches can also be used for MIMO modeling, though MIMO models typically require more parameters. A key issue of MIMO channel models is that they should predict the correlation between antenna elements, since the correlation controls the eigenvalues of the channel matrix and thus capacity (see Chapter 2.1.3). A MIMO channel model describes the $M \times N$ channel matrix, either as a frequency response $\mathbf{H}(t, f)$ or an impulse response $\mathbf{h}(t, \tau)$. Some common MIMO models are described below, for a more detailed overview of MIMO channel modeling, see [39].

3.3.1 Analytical MIMO Channel Models

Analytical MIMO channel models can be based on first and second order channel statistics. A common approach is the i.i.d. (Rayleigh) channel model, where each element of the channel matrix, $[\mathbf{H}]_{mn}$, is assigned the following properties:

$$E\{[\mathbf{H}]_{mn}\} = 0, \tag{3.12}$$

$$E\left\{|[\mathbf{H}]_{mn}|^2\right\} = 1, \tag{3.13}$$

$$E\{[\mathbf{H}]_{mn}[\mathbf{H}]_{kl}\} = 0, \text{ if } m \neq k \text{ or } n \neq l. \tag{3.14}$$

Since the i.i.d. Rayleigh channel relies on a rich scattering environment and assumes no correlation between the antenna elements, it produces overly optimistic results on the MIMO capacity. In reality, many MIMO channels include spatial correlation, and several methods exists to induce correlative effects on the channel matrix, such as the Kronecker model (see e.g., [40], [41]) and the model by Weichselberger et al [42].

A MIMO channel with a dominant component (such as a LOS component) can be modeled by [43]

$$\mathbf{H} = \sqrt{G}\left(\sqrt{\frac{K}{1+K}}\mathbf{H}^{dm} + \sqrt{\frac{1}{1+K}}\mathbf{H}^{fd}\right), \tag{3.15}$$

where $\sqrt{G}$ is the small-scale averaged path gain, $\mathbf{H}^{dm}$ is the dominant component, $\mathbf{H}^{fd}$ is the fading component given by (3.14) and K is the Ricean K-factor of the system. This model includes correlation between the antenna elements, though the only correlative effect is through the dominant component. In included paper I, we present an analytical model for MIMO channels that is based on a generalization of (3.15).

3.3.2 Physical MIMO Channel Models

Physical MIMO channel models can usually be derived by extending SISO models. The spatial domain, however, involves more parameters of interest, such that each multipath component is assigned a delay, angle-of-arrival (AOA), angle-of-departure (AOD), and Doppler frequency. The tapped-delay line of (3.11) is then extended to the double-directional channel model [30], i.e.,

$$h(t,\tau) = \sum_{i=1}^{N} h_i\left(t,\tau,\Omega_R,\Omega_T\right) g_R(\Omega_R) g_T(\Omega_T), \tag{3.16}$$

where

$$h_i(t,\tau,\Omega_R,\Omega_T) = a_i(t) e^{j2\pi\nu_i t}\delta(\tau-\tau_i)\delta(\Omega_R-\Omega_{R,i})\delta(\Omega_T-\Omega_{T,i}), \tag{3.17}$$

and ν_i is the Doppler frequency, τ_i the delay, $\Omega_{R,i}$ the AOA, and $\Omega_{T,i}$ the AOD of path i, respectively. Furthermore, $g_R(\Omega_R)$ and $g_T(\Omega_T)$ are the receiver and transmitter antenna gain at an (azimuth) angle-of-arrival Ω_R or angle-of-departure Ω_T, respectively (this description can also be extended to contain elevation angular information). Physical channel models are appealing for MIMO systems since the distribution of AOAs and AODs can have a big impact on the system capacity; a small angular spread at any side of the link usually reduces the rank of the channel matrix and hence capacity.

Stochastic physical MIMO channel modeling focus on either assigning statistical distributions to the scatterer parameters (i.e., without assuming an underlying geometry) or by randomly placing scatterers in a geometry, i.e., modeling their physical distributions. The latter method is referred to as geometry-based stochastic channel modeling (GSCMs). The difference to SISO modeling lies in a need to determine several channel responses, the channel between any transmit and receive antenna element, each with a separate antenna diagram, has to be derived. A major benefit with GSCMs is their ability to capture non-stationary effects. Since GSCMs model the location of TX, RX and each scatterer, it is easy to include temporal variations of their locations and thus describe motion of objects or terminals. Such an approach is chosen in the included paper III, where a GSCM for MIMO vehicle-to-vehicle communications is presented.

3.4 UWB Channel Modeling

The huge transmission bandwidth of UWB systems has several fundamental implications concerning the modeling of the propagation channel. All propa-

gation mechanisms show a frequency-dependence, and the fine delay resolution leads to consequences for the interaction between multipath components.

3.4.1 Properties of the UWB Propagation Channel

All important propagation mechanisms, free-space loss, transmission, reflection, diffraction and diffuse scattering, are frequency-dependent [44]. There are several underlying reasons. Firstly, the dielectric properties of materials typically show significant variations over a large relative bandwidth, and it has been shown that a pulse sent through various building materials show significant distortion [45]. Secondly, objects appear of different size at different frequencies, expressed in the number of *wavelengths*, and similarly, the electrical length of materials (e.g., walls) changes.

Since, generally speaking, free-space loss increases with increasing frequency only under the assumption of a constant antenna gain, the antennas can have a significant impact on UWB systems with a large relative bandwidth. To fulfill the constant gain requirement, an antenna would need to have a constant frequency response not only in the azimuth plane, but also in elevation. A non-isotropic antenna response will thus lead to different distortions of the received pulses depending on their direction of arrival, which in turn complicates pathloss derivations, where the distortion effects are seen as a frequency dependence. Equalizing the antenna influence is not straight-forward since it requires complete angular information of the MPCs (azimuth and elevation) as well as three-dimensional antenna calibration data over the whole frequency range of interest.

A large absolute bandwidth has impacts on the small-scale fading. Due to the fine delay resolution at the receiver, the number of components falling within one and the same delay bin is typically much smaller than for narrowband systems, which makes the fading effects less severe [46]. Mathematically speaking, this does not fulfill the conditions of the central limit theorem (the basis for the assumption of regular wireless channels being Rayleigh-fading) and hence several other distributions have been suggested to describe the UWB channel. Different measurement campaigns have proposed PDFs such as the Weibull [47], [48] or lognormal distribution [49] to describe the small-scale statistics, where the latter distribution was also used in the propagation model of the first IEEE UWB standard, 802.15.3a. In IEEE 802.15.4a, however, this model was abandoned in favor of the m–Nakagami distribution [50], whose PDF is given by

$$p\left(r\right) = \frac{2}{\Gamma(m)} \left(\frac{m}{\Omega}\right)^{m} r^{2m-1} \exp\left\{-\frac{mr^2}{\Omega}\right\}, \tag{3.18}$$

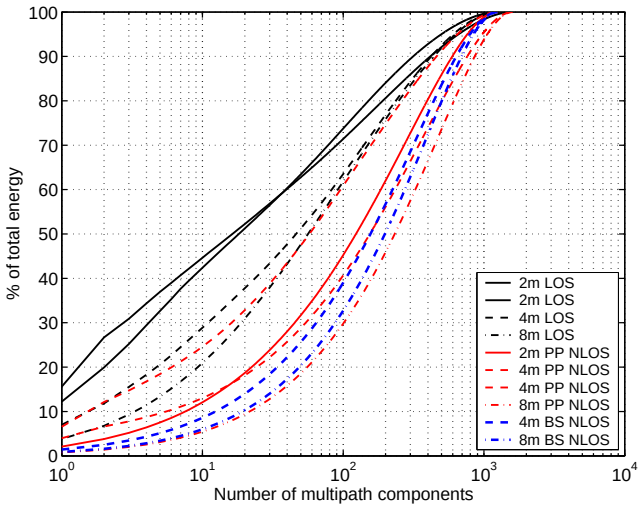

Figure 3.4: Captured energy using different numbers of multipath components, as derived from impulse responses measured in a factory hall. (From included paper V.)

where Ω is the mean power and m the Nakagami m-factor. The latter is a model parameter often studied in the context UWB channel modeling, and it is noteworthy that for $m = 1$, the Nakagami PDF breaks down to the Rayleigh distribution. The m-Nakagami PDF is also found capable of describing the small-scale amplitude statistics in the included paper V, where an industrial UWB channel was studied. However, the estimated m–parameters are close to 1 with the exception of the first component in each cluster.

Another consequence of the fine delay resolution is that the received energy is carried through a (very) large number of delay taps, up to several hundreds in a UWB system compared to just a few in a 5 MHz system [12]. With such a large number of resolvable MPCs, conventional Rake receivers (with 3–5 fingers) cannot be expected to capture more than a fraction of the available energy. This is also a conclusion of the included paper V, where UWB measurement results from factory halls are studied by counting the number of impulse response taps required to capture different percentages of the energy (see Fig. 3.4).

3.4.2 Modeling the UWB Impulse Response

For UWB communications over a large relative bandwidth, the common tapped-delay line model of (3.11) is usually not valid due to the pulse distortion mentioned above. Instead, each component is assumed to undergo distortion represented by a (time-varying) function $\chi_i(t,\tau)$ [13]. Then, (3.11) can be written

$$h(t,\tau) = \sum_{i=1}^{N} a_i(t)\chi_i(t,\tau) * \delta(\tau - \tau_i), \tag{3.19}$$

where $*$ denotes convolution. Characterization of the distortion function is a challenging task, with few results existing in the literature. A common approach is therefore the assumption of $\chi_i(t,\tau) = \chi_i(\tau) = \delta(\tau)$.

Many measurement campaigns have found clustering phenomena in typical UWB impulse responses, i.e., MPCs arrive at the receiver in "lumps." A well-known modeling method for a clustered impulse response was presented by Saleh and Valenzuela (SV) [51], who described the impulse response by

$$h(t) = \sum_{l=0}^{\infty}\sum_{k=0}^{\infty} \beta_{kl} e^{j\theta_{kl}} \delta\left(t - T_l - \tau_{kl}\right), \tag{3.20}$$

where β_{kl} and θ_{kl} are the gain and phase of the kth ray of the lth cluster, respectively, whereas T_l is the arrival time of the lth cluster and τ_{kl} the arrival time of the kth ray measured from the beginning of the lth cluster. Furthermore, the gain β_{kl} is determined by

$$\overline{\beta_{kl}^2} \equiv \overline{\beta^2\left(T_l, \tau_{kl}\right)} = \overline{\beta^2\left(0,0\right)} e^{-T_l/\Gamma} e^{-\tau_{kl}/\gamma}, \tag{3.21}$$

where Γ and γ are the cluster and ray power decay constants, respectively. This modeling approach is used in the included paper V, due to the clustered nature of the measured impulse responses, and also for the channel models of IEEE 802.15.3a and IEEE 802.15.4a. Whereas the original model uses the same ray power decay constant γ for all clusters, the measurements in paper V show a dependence on the excess delay. We include this in our model by a linear increase, i.e.,

$$\gamma = \gamma\left(\tau\right) = \gamma_0 + a\tau, \tag{3.22}$$

where γ_0 is the ray power decay constant of the first cluster and a is a constant.

The SV model generally gives a good fit to LOS impulse responses, but some NLOS situations can provide a quite different shape of the impulse response in terms of a "soft onset", such that the first tap of the impulse response is not the strongest on average. Such channel conditions has system implications on, e.g., partial Rake receivers that capture the first arriving components and

thus cannot be expected to work well [52]. This impulse response shape was observed in the included paper V, and was modeled by

$$\overline{\beta_{kl}^2} = \Omega_1 \frac{\gamma_1 + \gamma_{\text{rise}}}{\gamma_1 \left(\gamma_1 + \gamma_{\text{rise}} \left(1 - \chi\right)\right)} \left(1 - \chi e^{-\tau/\gamma_{\text{rise}}}\right) e^{-\tau/\gamma_1}, \tag{3.23}$$

where γ_1, γ_{rise} and χ are shape parameters while Ω_1 is the normalized power [53].

Chapter 4

Channel Measurements

In one sense or another, all channel models rely on measurements of the wireless propagation channel. For stochastic channel models, model parameters need to be extracted from measured data, but also postulated scatterer models or raytracing models need to be verified against reality. Measurements of the wireless channel properties is also known as channel sounding, a name stemming from a transmitter that "sounds" (or excites) the channel, whereas the receiver records the channel output.

While early channel sounders in the 1960s were only required to measure field strength, their complexity has increases drastically since then. The introduction of wideband wireless systems requires measurements of the delay dispersion of the channel, whereas the research on multiple antenna systems has rendered an interest in directional channel properties. Furthermore, up until the 1990s, channel measurements were mostly focused on macrocells. Many more recent campaigns, however, have been aiming at characterizing indoor scenarios, which puts higher demands on the required delay resolution of a channel sounder. Finally, recent wireless applications such as vehicle-to-vehicle communications systems (see included paper III) imply that current channel sounders are required to store the fast fluctuations of the time-varying, wideband, double-directional propagation channel.

4.1 Measurement Techniques

Channel measurements can be performed in the time or frequency domain, storing the channel impulse response $h(\tau, t)$ or transfer function $H(f, t)$, respectively. Time-domain measurements obtain the channel impulse response

by exciting the channel with pulses or pseudo-noise sequences. Frequency domain measurements, on the other hand, typically use a chirp-like or other multitone signal to sound the channel.

While band-limited time-invariant measurements, i.e., $H(f,t) = H(f)$ and $h(\tau,t) = h(\tau)$, can be performed as long as the channel is sampled at the Nyquist rate, additional requirements must be considered for time-variant channels. First of all, the repetition time of the sounding signal T_{rep} must be shorter than the coherence time of the channel, i.e., short enough for the channel not to have changed between the beginning and end of the sounding sequence. This implies that the temporal sampling frequency f_{rep} must fulfill

$$\frac{1}{T_{\text{rep}}} = f_{\text{rep}} \geq 2\nu_{\max}, \tag{4.1}$$

or

$$T_{\text{rep}} \leq \frac{1}{2\nu_{\max}}, \tag{4.2}$$

where $\nu_{\max}$ is the maximum Doppler frequency. Secondly, in order to avoid overlap between consecutive sounding signals, the delay dispersion of the channel has to be taken into account by

$$T_{\text{rep}} \geq \tau_{\max}, \tag{4.3}$$

where $\tau_{\max}$ is the maximum excess delay of the channel. Combining these two requirements gives

$$\tau_{\max} \leq T_{\text{rep}} \leq \frac{1}{2\nu_{\max}} \tag{4.4}$$

or

$$2\nu_{\max}\tau_{\max} \leq 1. \tag{4.5}$$

Equation (4.5) is known as the two-dimensional Nyquist criterion, and when fulfilled, the channel is said to be underspread. This applies for the vast majority of the wireless channels, meaning that the temporal variations of the channel are sufficiently slow. For the reversed situation, the channel can only be identified based on a priori assumptions of an underlying model. While complying with (4.5), it is also often of interest to perform measurements with a *time bandwidth product* larger than unity. Since the possible transmit power usually is limited by regulations, the total available signal energy can instead be increased by increasing the length of the sounding sequence; a length larger than the inverse of the sounding signal bandwidth achieves a time bandwidth product larger than one.

Some specific conditions apply for measurements of MIMO and UWB channels. Measurement noise is of concern for any channel measurement, but an

especially important issue for UWB measurements. Due to the large bandwidth (the FCC range covers both the ISM band at ~ 2.4 GHz and the 5 GHz WLANs), chances are that there is an existing wireless service in the vicinity of the measurement setup. Thus, UWB measurements sites need to be "swept" for interference power using a spectrum analyzer. The alternative is to perform measurements in environments shielded from noise, such as the shielded chamber we use in the included paper IV. Furthermore, there is a slight preference for frequency domain UWB measurements in the literature. Whereas the pulse-based measurements are seemingly in perfect alignment with the core idea of impulse radio, there is a difficulty in generating sufficiently short high-energy pulses.

For MIMO channels, the channel responses between all possible combinations of TX and RX antenna elements have to be measured. Three different methods apply: With *real* arrays, each with its own RF chain, the channel can be measured directly at the different receiver elements. This approach is costly, and puts high requirements on the calibration procedure. In contrast, the usage of *switched* arrays only requires one RF chain at the receiver [54]. Fast RF switches, or *multiplexers*, control the switching between the different TX and RX elements, such that only one antenna pair is measured at a time. The simplest measurement method uses *virtual* arrays, i.e., only one antenna element is available at each side of the link, and MIMO measurements are performed by moving the elements to predefined positions before each sounding of the channel. The advantage of virtual arrays lie in their simplicity, though there is a major drawback in terms of limitations on the allowable temporal variations of the channel; it needs to be static during the whole measurement run. In the following sections, we describe the measurement systems that were used to record the measurement data used in this thesis.

4.2 RUSK LUND Channel Sounder

Papers I-III relies on data stored using the RUSK Lund channel sounder, which uses the switched array principle. Though the exact design is not publically available, the basic sounding method is through frequency correlative measurements (see Fig. 4.1 for an overview). The channel is sounded using a multitone, OFDM-like, signal where the fixed phases of each subcarrier are selected in order to minimize the *crest factor* (peak-to-average power ratio) of the transmitted signal. Thus sounding the channel at different frequencies simultaneously, the low crest factor ensures a low distortion level in the amplifier and modulator circuits. Once designed in the frequency domain, the corresponding time domain sounding signal is stored and periodically repeated.

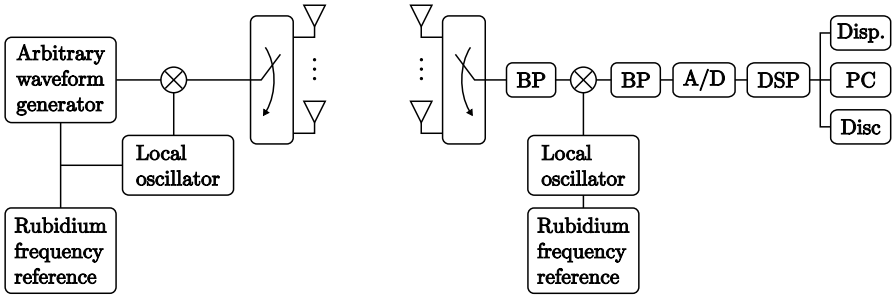

Figure 4.1: Block diagram of the RUSK Lund channel sounder (courtesy of Medav).

Since the RUSK Lund sounder is continuously transmitting the sounding signal, i.e., $T_{\text{rep}} = T_p$, we have from (4.3) that $T_p \geq \tau_{\max}$ must be fulfilled. This, in turn, determines the frequency spacing of the (frequency-domain) sounding signal as $f_\Delta = 1/T_p$, such that delays up to T_p can be measured. As previously discussed, a long sounding sequence is beneficial since it leads to a higher time-bandwidth product, which for a correlation-based sounder gives benefits in terms of a correlation gain at the receiver.

The received signal is bandpass-filtered, down-converted to an intermediate frequency of 160 Hz, demodulated, sampled at 640 Hz and, finally, the time-domain sampled data is converted to the frequency domain through a Fast Fourier Transform (FFT) in the Digital Signal Processing (DSP) block in Fig. 4.1. The time-variant channel responses are estimated through a cross-correlation with the (Fourier-transformed) calibration data in order to remove sounder influence.

Since the sounder applies the switched-array principle, thus making use of fast multiplexers to sequentially step through the transmit and receive antenna elements, the length of a complete MIMO snapshot is determined by the switching cycle as illustrated in Fig. 4.2. Having its switching time synchronized to the length of the sounding period, T_p, the sounder requires an additional guard period (GP) of length T_p between every RX element in order to avoid unintentional overlaps between consecutive snapshots. With N TX elements and M RX elements, (4.2) thus extends to a requirement of

$$2 \cdot T_p \cdot M \cdot N \leq \frac{1}{2\nu_{\max}}, \tag{4.6}$$

where $2 \cdot T_p \cdot M \cdot N$ thus is the length of one MIMO snapshot. Additionally, MIMO snapshots are stored in blocks, where the number of snapshots per

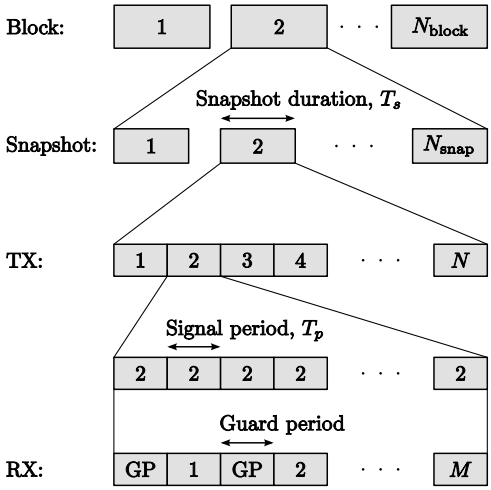

Figure 4.2: Recorded data structure of the RUSK Lund channel sounder.

block, N_{snap}, the number of blocks N_{block} and the sampling time between consecutive snapshots or blocks are parameters to be set depending on the specific measurement scenario.

4.3 Vector Network Analyzer

Vector Network Analyzer (VNA) measurements were used to conduct the measurements in included papers IV and V. VNAs sound the channel by slowly sweeping the frequency range of interest and estimating the transfer function between its two ports (S_{21}). Since the antennas are not a part of the VNA calibration procedure, obtaining the "pure" channel from VNA measurements thus requires a separate calibration of the antennas, whose influence only can be completely removed if the directions of all multipath components are known (in elevation as well as azimuth). This is particularly interesting for UWB systems, given the frequency dependence of the antenna patterns (see Chapter 3.4.1).

The VNA measurements were performed using virtual arrays as shown in Fig. 4.3 (even though the antennas were *manually* moved between positions in paper IV). As previously mentioned, the main benefits of virtual array measurements lie in their simplicity, but also the (position) accuracy is appealing for high-resolution algorithms. The usage of virtual arrays also avoids the problem of coupling between antenna elements that can occur in the case of

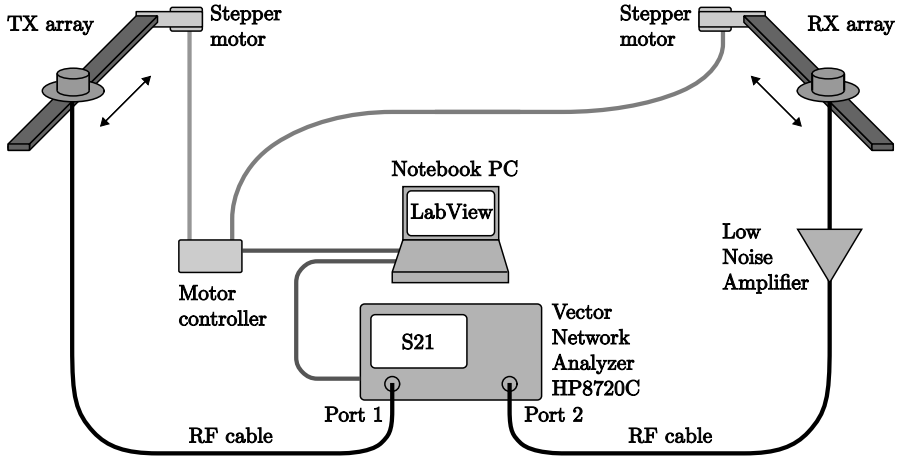

Figure 4.3: The virtual array measurement setup. The stepper motors of the virtual arrays as well as the VNA are controlled through a LabView script on a notebook PC.

measurements with real arrays. The main drawback, apart from the virtual array requiring a static environment, is that the possible measurement range is limited since TX and RX are connected through cables to the VNA.

Chapter 5

Summary and Contributions

This chapter summarizes my contributions to the research field. Including five papers of varying focus, this thesis extends the general understanding of wireless propagation channels for MIMO and UWB applications. Three detailed simulation models are presented, two for MIMO and one for UWB, which can hopefully benefit the design process of future communications systems. Conclusions from the individual papers are given within the summary of each one in Sec. 5.1, where also my contributions to each paper are specified. Some general conclusions regarding the measurement and modeling of wireless propagation channels are discussed in Sec. 5.2 along with a few thoughts on future work.

5.1 Paper Contributions

5.1.1 Paper I: "A Measurement-Based Fading Model for Wireless Personal Area Networks"

This paper puts focus on the interaction between user and antenna device and how this influences the propagation channel for short-range indoor applications, commonly referred to as Personal Area Networks (PANs). Since PAN channels are associated with human presence in the immediate vicinity of the terminals, it is important to study the combined effect of user, antenna and channel. Whereas the vast majority of previous propagation measurement campaigns were performed using *uniform* antenna arrays without human influence, this paper describes extensive MIMO measurements performed with *irregular*

antenna arrays and human users at one or both link ends.

The measurement results show that the human influence motivates the distinction between two shadowing effects: body shadowing and shadowing due to the environment. We find that body shadowing can have a significant impact on pathloss; up to 20 dB extra attenuation on the radio link is observed depending on the orientation of the user(s). In combination with the irregular antenna arrays we use, the human interaction is also found to be the cause of small-scale amplitude statistics that are sensitive to the exact location of the user, and the element relative the user. The classical approach of modeling a radio link as Ricean or Rayleigh fading during motion over a small area is thus not suitable for PANs. Rather, sampling the channel during even small movements of the antenna devices will render a combination of Rayleigh distributed amplitude samples and samples from a Ricean distribution (with various K-factors). We therefore suggest a mixed distribution, the generalized gamma distribution, suitable to describe such amplitude fluctuations.

These observations are included in a detailed model for all fading effects of the SISO link, modeling large-scale shadowing variances and parameters to control the generalized gamma distribution. The model also includes a *relative path gain* to account for the power imbalance between the different antenna elements of the irregular antenna arrays we are using.

I am the main contributor to this paper and I was involved in all parts of the scientific work: channel measurements, data analysis, model derivation and the writing of the paper.

5.1.2 Paper II: "A MIMO Channel Model for Personal Area Networks"

This paper presents a MIMO model based on the PAN measurements described in paper I. Finding no existing MIMO channel model suitable to describe the measured channel characteristics, we propose a generalization of the well-known LOS MIMO model, where the channel is given as the sum of a dominant and a fading part. We make use of two important conclusions from paper I, that different links in the MIMO channel matrix experience different small-scale fading statistics and have different mean power (through the relative path gain), and find that including these effects in our model can capture important MIMO characteristics in terms of antenna correlation, eigenvalues and capacity. We first give the narrowband model description, and then extend it to the time-variant wideband case. Additional measurements are used to supply a parameterization for a specific PAN scenario: situations with no large-scale movement of transmitter and receiver.

I am the main contributor to this paper and I was involved in all parts of

the scientific work: channel measurements, data analysis, model derivation and the writing of the paper.

5.1.3 Paper III: "A Geometry-Based Stochastic MIMO Model for Vehicle-to-Vehicle Communications"

In this paper we present a simulation model suitable for MIMO systems in vehicle-to-vehicle applications. The paper is based on one of the first MIMO measurement campaigns for such applications, performed in highway and rural traffic situations. With the measurement data showing a non-stationary behavior, where the mean received power as well as the Doppler spectrum can change significantly over time, we find no existing channel model that can adequately describe these effects. Instead, we opt for developing a geometry-based stochastic model, since GSCMs are suitable to describe non-stationary channels.

Using a high-resolution method, we analyze the contributions from single scattering objects, such as cars, road signs and houses, and find their power contributions to be fading, likely due to the interaction of several unresolvable paths. We model such fluctuations by prescribing a stochastically varying amplitude to some scatterers (labeled "discrete"), whereas others (labeled "diffuse") are complex Gaussian distributed as in classical GSCM. The proposed model is compared to measurement data, and we provide a full simulation model for the complex channel impulse response.

I am the main contributor to this paper and I was involved in all parts of the scientific work: channel measurements, data analysis, model derivation and the writing of the paper.

5.1.4 Paper IV: "Characterization of a Computer Board-to-Board Ultra-Wideband Channel"

In the context of envisioning UWB systems as cable replacements, this paper explores the possibilities for such applications between desktop computer boards. We present the results of the first propagation measurements inside the chassis of two different desktop computers and conclude that the variations in received (small-scale averaged) signal power are very small for both computers. Subsequently, the fading margins needed by a UWB system to account for large-scale variations can be small. The only notable difference in channel properties between the two computers lies in the delay dispersion and relates to the interior design; the more crowded computer has a smaller delay spread.

The expected noise level is a key matter for the performance of any wireless application, and of particular interest for this type of application. Firstly, it

is a UWB system (see Chapter 4.1), and secondly, the computer itself can be expected to produce noise. We thus performed noise measurements inside the computers using a spectrum analyzer. The results show that interference is present over the whole FCC-approved frequency band, though limited to regularly spaced subbands. This suggests that multi-band UWB techniques are more suitable for this type of applications.

I was involved in setting up the channel measurements, data analysis, model derivation and the writing of the paper.

5.1.5 Paper V: "A Measurement-Based Statistical Model for Industrial Ultra-Wideband Channels"

This paper describes a UWB channel model based on the first UWB channel measurements performed in an industrial environment. When the IEEE sought to develop the new 802.15.4a standard, it was clear that the (older) 802.15.3a channel model was not sufficient for the testing of system proposals. One of the main reasons for this was that (due to different applications) it was necessary to include propagation models for more environments. There was thus a need for the characterization of several propagation environments, out of which the industrial environment was one. Partial results of this paper were used as input to the IEEE 802.15.4a standard channel model.

The paper presents results from three different measurement campaigns performed at two different sites, and concludes that the impulse response usually is of a multi-cluster nature. A detailed model for the impulse response is provided based on a Saleh-Valenzuela approach to account for the multiple clusters. We introduce a generalization to the classical Saleh-Valenzuela model in terms of modeling the ray power decay time constants (the decay *within* a cluster) as increasing with excess delay. We also observe that some NLOS situations, especially for larger distances, render an impulse response where the first delay tap is not the strongest, rather the strongest tap occurs some 10 ns *after* the first arriving component. This kind of "soft onset" is modeled by means of a separate function controlling the rise time and decay time of the impulse response. Furthermore, we observe small-scale amplitude statistics that can be described by the m-Nakagami distribution, though the m-parameter estimates close to 1 implies that they are close to Rayleigh distributed. This is in contrast to the common assumption of the fine delay resolution of UWB systems violating the central limit theorem, thus leading to non-Rayleigh fading statistics.

I am the main contributor to this paper and I was involved in all parts of the scientific work: channel measurements, data analysis, model derivation and the writing of the paper.

5.2 General Conclusions and Future Work

A natural question to ask someone having done a Ph.D. on channel modeling would be: what constitutes a good channel model? While this question does not have a simple answer, I take the opportunity in this section to elaborate a little on the subject. Doing so, I thereby share some general conclusions on the principles behind measuring and modeling of the wireless propagation channel that I have drawn during my years within the field.

First of all, I have learned that the wireless propagation channel is a complicated process. There are a huge number of factors that determine how the transmitted information is conveyed to the receiver, especially in a time-varying scenario, and including them all rapidly increases the model complexity. In this context, one aspect on channel modeling that I think deserves being given much more attention is the trade-off between simplicity and accuracy. A model may be never so accurate, but it doesn't matter as long as it is deemed too complicated to be actually used by anyone. I therefore think that models in general should strive more towards simplicity. Despite their shortcomings, the i.i.d. Rayleigh MIMO model and the Kronecker MIMO model are seemingly very popular.

If truly accurate predictions on a *particular* site are of interest, I would say that ray-tracing methods are the way to go. Since such methods have the potential of including the interaction with almost anything in the channel, their achievable exactness leaves little to ask for. However, ray-tracing methods are not as well suited for certain situations. Rapidly changing propagation environments, with high-speed mobility of both TX, RX and scatterers, requires a lot of effort to be included in a ray-tracing simulator. The same effect applies for close-to-body antennas, such as in PANs, where the temporal variations of the combined pattern of user and antenna need to be included. For such situations, as well as whenever an *arbitrary* example of a realistic channel is desired, I think a simple stochastic model is a more appealing approach for a system designer who wants run performance evaluations. The strive towards simplicity is also the motivation behind some modeling choices in the included papers, such as the modeling approach in paper II and the modeling of discrete scatterer amplitudes in paper III.

The alternative to using simulated channel data for testing is to use measured channel data. Testing wireless systems in real-life situations will of course always play an important role in the development chain, though rather in the later stages. Before venturing into the time-consuming task of gathering channel data, I think simulations can serve as a first encounter with realistic channel conditions. Furthermore, a direct usage of measurement data not only has the drawback of including measurement noise (which can have a large impact on

particular evaluations) but is also limited to the exact measurement scenario in which the data were collected. A good channel model should allow for easy altering of important channel parameters, e.g., delay or frequency dispersion.

In the future, I would like to see more investigations on the interaction between humans, antennas and the channel. Whereas some important observations on this were drawn in papers I and II, much more needs to be done, such as a more thorough analysis of the combined antenna pattern of user and antenna. This links to another interesting future topic, namely what kind of antennas that should be used during channel characterization. Whereas a great deal of measurement campaigns has used uniform arrays, which are suitable for array processing, it is well-known that the performance of a MIMO system depends highly on the exact antenna configuration (which is also confirmed by our paper II). I therefore think that future measurements should focus, to a larger extent than today, on channel characterization using more realistic antenna arrangements. Finally, I would like to see more cooperation between those working on a system design level and those who develop channel models. A channel model that is never being used obviously is of little value. It is therefore my opinion that any channel modeling work should consider what specific properties that are the most essential for those who are intended to make use of the model.

References

[1] H. H. Beverage and H. O. Petersen, "Diversity receiving system of R.C.A. Communications, Inc., for radiotelegraphy," *Proceedings of the IRE*, vol. 19, pp. 529–561, Apr. 1931.

[2] D. G. Brennan, "Linear diversity combining techniques," *Proceedings of the IRE*, vol. 47, pp. 1075–1102, June 1959.

[3] J. H. Winters, "On the capacity of radio communications systems with diversity in Rayleigh fading environments," *IEEE Journal on Selected Areas in Communications*, vol. 5, pp. 871–878, June 1987.

[4] G. J. Foschini and M. J. Gans, "On limits of wireless communications in a fading environment when using multiple antennas," *Wireless Personal Communications*, vol. 6, pp. 311–335, Feb. 1998.

[5] I. E. Telatar, "Capacity of multi-antenna Gaussian channels," *European Transactions on Telecommunications*, vol. 10, pp. 585–595, Nov.-Dec. 1999.

[6] A. Paulraj, R. Nabar, and D. Gore, *Introduction to Space-Time Wireless Communications*. Cambridge, U.K.: Cambridge University Press, 2003.

[7] D. Gesbert, M. Shafi, D.-S. Shiu, P. J. Smith, and A. Naguib, "From theory to practice: An overview of MIMO space-time coded wireless systems," *IEEE Journal on Selected Areas in Communications*, vol. 21, pp. 281–302, 2003.

[8] D. Tse and P. Viswanath, *Fundamentals of Wireless Communication*. Cambridge, UK: Cambridge University Press, 2005.

[9] P. Almers, T. Santos, F. Tufvesson, A. Molisch, J. Karedal, and A. J. Johansson, "Antenna subset selection in measured indoor channels," *IET Microwaves, Antennas & Popagation*, vol. 1, pp. 1092–1100, 2007.

[10] S. M. Alamouti, "A simple transmit diversity technique for wireless communications," *IEEE Journal on Selected Areas in Communications*, vol. 16, pp. 1451–1458, Oct. 1998.

[11] G. J. Foschini, "Layered space-time architecture for wireless communication in a fading environment when using multi-element antennas," *Bell Labs Technical Journal*, pp. 41–59, 1996.

[12] X. Shen, M. Guizani, R. C. Qiu, and T. Le-Ngoc, eds., *Ultra-Wideband Wireless Communications and Networks*. Wiley, 2006.

[13] R. C. Qiu, H. Liu, and X. Shen, "Ultra-wideband for multiple access communications," *IEEE Communications Magazine*, vol. 43, pp. 80–87, Feb. 2005.

[14] M.-G. Di Benedetto and G. Giancola, *Understanding Ultra Wide Band Radio Fundamentals*. Upper Saddle River, NJ, USA: Prentice Hall, 2004.

[15] R. A. Scholtz, "Multiple access with time-hopping impulse modulation," vol. 2, pp. 447–450, Oct. 1993.

[16] M. Z. Win and R. A. Scholtz, "Impulse radio: How it works," *IEEE Communications Letters*, vol. 2, pp. 36–38, Feb. 1998.

[17] M. Z. Win and R. A. Scholtz, "Ultra-wide bandwidth time-hopping spread-spectrum impulse radio for wireless multiple-access communications," *IEEE Transactions on Communications*, vol. 48, pp. 679–691, Apr. 2000.

[18] Federal Communications Commission, "First report and order 02-48," 2002.

[19] A. F. Molisch et al., "IEEE 802.15.4a channel model - final report," Tech. Rep. Document IEEE 802.15-04-0662-02-004a, 2005.

[20] K. Yu, *Multiple-Input Multiple-Output Radio Propagation Channels – Characteristics and Models*. PhD thesis, Royal Institute of Technology, Stockholm, Sweden, 2005.

[21] A. Taflove, *Computational Electrodynamics The Finite-Difference Time Domain Method*. Norwood, MA, USA: Artech House, 1995.

[22] N. Ottosen and H. Pettersson, *Introduction to the Finite Element Method*. Upper Saddle River, NJ, USA: Prentice Hall, 1992.

[23] F. Ikegami, T. Takeuchi, and S. Yoshida, "Theoretical prediction of mean field strength for urban mobile radio," *IEEE Transactions on Antennas and Propagation*, vol. 39, no. 3, pp. 299–302, 1991.

[24] S. Y. Seidel and T. S. Rappaport, "A ray-tracing technique to predict path loss and delay spread inside buildings," in *Proc. IEEE Global Communications Conference*, vol. 2, pp. 649–653, Dec. 1992.

[25] C.-F. Yang, B.-C. Wu, and C.-J. Ko, "A ray-tracing method for modeling indoor wave propagation and penetration," *IEEE Transactions on Antennas and Propagation*, vol. 46, no. 6, pp. 907–919, 1998.

[26] J. Maurer, *Strahlenoptisches Kanalmodell für die Fahrzeug-Fahrzeug-Funkkommunikation*. PhD thesis, Institut für Höchstfrequenztechnik und Elektronik (IHE), Universität Karlsruhe (TH), Karlsruhe, Germany, July 2005. In German.

[27] J. Fuhl, A. F. Molisch, and E. Bonek, "Unified channel model for mobile radio systems with smart antennas," in *IEE Proceedings Radar, Sonar and Navigation*, vol. 145, pp. 32–41, Feb. 1998.

[28] P. Petrus, J. H. Reed, and T. S. Rappaport, "Geometrical-based statistical macrocell channel model for mobile environments," *IEEE Transactions on Communications*, vol. 50, pp. 495–502, 2002.

[29] A. F. Molisch, A. Kuchar, J. Laurila, K. Hugl, and R. Schmalenberger, "Geometry-based directional model for mobile radio channels - principles and implementation," *European Transactions on Telecommunications*, vol. 14, pp. 351–359, 2003.

[30] A. F. Molisch, "A generic channel model for MIMO wireless propagation channels in macro- and microcells," *IEEE Transactions on Signal Processing*, vol. 52, pp. 61–71, Jan. 2004.

[31] A. F. Molisch, *Wireless Communications*. Chichester, West Sussex, UK: IEEE Press–Wiley, 2005.

[32] T. S. Rappaport, *Wireless Communications — Principles and Practices*. Upper Saddle River, NJ, USA: Prentice Hall, 1996.

[33] H. Suzuki, "A statistical model for urban radio propagation," *IEEE Transactions on Communications*, vol. COM-25, pp. 673–680, July 1977.

[34] A. Abdi, C. Tepedelenlioglu, M. Kaveh, and G. Giannakis, "On the estimation of the K parameter for the Rice fading distribution," *IEEE Communications Letters*, vol. 5, pp. 92–94, Mar. 2001.

[35] R. Vaughan and J. B. Andersen, *Channels, Propagation and Antennas for Mobile Communications*. London, UK: IEE, 2003.

[36] P. A. Bello, "Characterization of randomly time-variant linear channels," *IEEE Transactions on Communications*, vol. 11, pp. 360–393, 1963.

[37] W. C. Jakes, ed., *Microwave Mobile Communications*. New York: Wiley, 1974.

[38] P. Hoeher, "A statistical discrete-time model for the WSSUS multipath channel," *IEEE Transactions on Vehicular Technology*, vol. 41, pp. 461–468, Nov. 1992.

[39] P. Almers, E. Bonek, A. Burr, N. Czink, M. Debbah, V. Degli-Esposti, H. Hofstetter, P. Kyoesti, D. Laurenson, G. Matz, A. Molisch, C. Oestges, and H. Oezcelik, "Survey of channel and radio propagation models for wireless MIMO systems," *EURASIP Journal on Wireless Communications and Networking*, vol. 2007, 2007.

[40] J. P. Kermoal, L. Schumacher, K. I. Pedersen, P. E. Mogensen, and F. Frederiksen, "A stochastic MIMO radio channel model with experimental validation," *IEEE Journal on Selected Areas in Communications*, vol. 20, pp. 1211–1226, Aug. 2002.

[41] D. P. McNamara, M. A. Beach, and P. N. Fletcher, "Spatial correlation in indoor MIMO channels," in *Proc. IEEE International Symposium on Personal, Indoor and Mobile Radio Communications*, vol. 1, (Lisbon, Portugal), pp. 290–294, 2002.

[42] W. Weichselberger, M. Herdin, H. Özcelik, and E. Bonek, "A stochastic MIMO channel model with joint correlation of both link ends," *IEEE Transactions on Wireless Communications*, vol. 5, pp. 90–100, Jan. 2006.

[43] F. Rashid-Farrokhi, A. Lozano, G. Foschini, and R. Valenzuela, "Spectral efficiency of wireless systems with multiple transmit and receive antennas," in *Proc. IEEE International Symposium on Personal, Indoor and Mobile Radio Communications*, vol. 1, pp. 373–377, Sept. 2000.

[44] A. F. Molisch, "Ultrawideband propagation channels - theory, measurement, and modeling," *IEEE Transactions on Vehicular Technology*, vol. 54, pp. 1528–1545, Sept. 2005. Invited paper.

[45] A. H. Muqaibel, A. Safaai-Jazi, A. Bayram, and S. Riad, "UWB through-the-wall propagation and material characterization," in *Proc. IEEE Antennas Propagation Society International Symposium*, pp. 623–626, 2003.

[46] F. Ramírez-Mireles, "On the performance of ultra-wideband communications in dense multipath," *IEEE Transactions on Vehicular Technology*, vol. 50, pp. 244–249, Jan. 2001.

[47] Á. Álvarez, G. Valera, M. Lobeira, R. Torres, and J. L. García, "New channel impulse response model for UWB indoor system simulations," in *Proc. IEEE Vehicular Technology Conference 2003 spring*, pp. 1–5, June 2003.

[48] P. Pagani and P. Pajusco, "Experimental assessment of the UWB channel variability in a dynamic indoor environment," in *Proc. IEEE International Symposium on Personal, Indoor and Mobile Radio Communications*, pp. 2973–2977, 2004.

[49] J. R. Foerster and Q. Li, "UWB channel modeling contribution from Intel," Tech. Rep. P802.15 02/279SG3a, Intel Corporation, Hillboro, OR, USA, June 2002. IEEE P802.15 SG3a contribution.

[50] M. Nakagami, "The m-distribution – a general formula of intensity distribution of rapid fading," in *Statistical methods in radio wave propagation* (W. C. Hoffman, ed.), Oxford, UK: Pergamon, 1960.

[51] A. A. M. Saleh and R. A. Valenzuela, "A statistical model for indoor multipath propagation," *IEEE Journal on Selected Areas in Communications*, vol. 5, pp. 128–137, Feb. 1987.

[52] D. Cassioli, M. Z. Win, F. Vatalaro, and A. F. Molisch, "Low complexity Rake receivers in ultra-wideband channels," vol. 6, pp. 1265–1275, Apr. 2007.

[53] A. F. Molisch, D. Cassioli, C.-C. Chong, S. Emami, A. Fort, B. Kannan, J. Karedal, J. Kunisch, H. G. Schantz, K. Siwiak, and M. Z. Win, "A comprehensive standardized model for ultrawideband propagation channels," *IEEE Transactions on Antennas and Propagation*, vol. 54, pp. 3151–3166, Nov. 2006.

[54] R. Thomae, D. Hampicke, A. Richter, G. Sommerkorn, A. Schneider, U. Trautwein, and W. Wirnitzer, "Identification of the time-variant directional mobile radio channels," *IEEE Transactions on Instrumentation and Measurement*, vol. 49, pp. 357–364, 2000.

Part II

Included Papers

Paper I

A Measurement-Based Fading Model for Wireless Personal Area Networks

Johan Karedal, *Student Member, IEEE*, Anders J. Johansson, *Member, IEEE*, Fredrik Tufvesson, *Senior Member, IEEE*, and Andreas F. Molisch, *Fellow, IEEE*

***Abstract*—Personal area networks (PANs) are wireless communications systems with high data rates but small coverage area. PAN propagation channels differ from the well-explored propagation channels of wide-area networks due to several reasons: (i) the distances are typically very small, (ii) the antenna arrangements can be quite different, and (iii) the influence from human presence in the environment is different.**

The current paper presents results of a channel measurement campaign, where measurements are conducted over distances of 1-10 m using several multi-antenna devices, combined to create different PAN scenarios. For each measured Tx-Rx separation, channel realizations are obtained by small spatial movements of the antenna devices, and by rotating the persons holding the devices.

From the results, we draw two main conclusions: (i) The small-scale amplitude statistics, analyzed as the variations over a small sampling area and frequency subchannels, cannot be described in a satisfactory way using only the Rayleigh or Ricean distribution, rather a mixed distribution, the generalized gamma distribution, is more suitable; (ii) it is advantageous to distinguish between two types of large-scale fading: body shadowing (due to the orientation of the person holding the device) and shadowing due to surrounding objects (lateral movement). We also define and parameterize a complete statistical model for all fading.

***Index Terms*—Personal area networks, channel measurements, statistical channel model, body shadowing.**

I. Introduction

PERSONAL area networks (PANs) are often defined as a network where transmitter and receiver are separated no more than 10 m, usually located within the same room. In the last years, there has been a steadily increasing interest in such networks, and various technologies have been explored for improving their performance [3], [4]. In order to achieve the high data rates that are required for many PAN applications, multiple-antenna systems [5], [6], [7] seem especially suitable and have been explored, e.g., in the European MAGNET project [8].

In order to assess the potential and the performance of PAN systems, it is necessary to measure and model the wireless propagation channels between transmitters and receivers. PAN channels differ remarkably from traditional wireless local area network (WLAN) channels that have been well explored. First, the distance between transmitter and receiver is smaller for PANs than in typical WLANs. Secondly, most multi-antenna WLAN propagation channel measurement campaigns make use of uniform arrays, in which the physical environment experienced by an array element can also be assumed to be experience by its array neighbor. However, the antenna arrangements on PAN devices can be quite different, with antenna elements being squeezed in wherever they may fit, and thus different antenna elements can no longer be expected to "see" the same environment. Thirdly, and most importantly, PAN communications usually involve at least one handheld or bodyworn device, and the user holding the device has a distinctive impact on the propagation channel. The user can be viewed as an integral part of antenna, i.e., the total antenna pattern is determined by a combination of the exact positions of the antenna, the user and his/her extremities. Therefore, it is preferable to analyze the combined effect of channel, antennas, and human operators of the mobile station - again in contrast to WLAN channels, where models of propagation channels in the absence of users are the norm (see, e.g., [9]).[1]

While there are numerous publications on BAN propagation (see, e.g., [11], [12] and [13]), the propagation effects in PAN settings are quite different, and despite their great practical importance, measurements and models of PAN channels can, to the authors' best knowledge, hardly be found in the literature. The current paper intends to alleviate that gap. It reports the results of a wideband measurement campaign for a number of PAN scenarios, where we find that PAN channels show a fundamentally different *structure* of the small-scale and the large-scale fading.

Large-scale fading or shadowing, i.e., variations of the received power due to obstruction of propagation paths by various objects, has commonly been modeled as lognormally-distributed variations of the (distance-dependent, narrowband) pathloss. However, this model was originally devised for cellular systems, and is insufficient for many PANs; due to the body shadowing, variations occur not only by lateral movement, but also by rotation of the user (which are more common in PANs), and/or movement of the antennas with respect to the body. It is thus preferable to distinguish between the shadowing caused by surrounding objects and the shadowing

Manuscript received May 14, 2007; revised March 3, 2008; accepted April 18, 2008. The associate editor coordinating the review of this letter and approving it for publication was M. Win. Parts of this work have been published at EUSIPCO 2006 [1] and VTC 2006 fall [2].

J. Karedal, A. J Johansson, and F. Tufvesson are with the Dept. of Electrical and Information Technology, Lund University, Lund, Sweden (e-mail: {Johan.Karedal, Anders.J.Johansson, Fredrik.Tufvesson}@eit.lth.se).

A. F. Molisch is with Mitsubishi Electric Research Laboratories (MERL), Cambridge, MA, USA, and also at the Dept. of Electrical and Information Technology, Lund University, Lund, Sweden (e-mail: Andreas.Molisch@ieee.org).

Digital Object Identifier 10.1109/T-WC.2008.070500

[1] An exception is, e.g., the recent paper [10] that analyzes the impact of humans on the transfer function in wireless LANs.

caused by the body as different types of movements of the users lead to different types of shadowing, with different fading statistics and coherence times.

Small-scale fading is typically modeled as being Ricean distributed for line-of-sight (LOS) situations, and Rayleigh distributed for non-line-of-sight (NLOS) situations. However, as we will see in this paper, the proximity of the human body and the irregular antenna arrangements, makes this description insufficient, and furthermore, the antenna arrangements also cause the small-scale fading to have different statistics at different antenna elements.

Thus, the key contributions of this paper are:

- We present results from an extensive measurement campaign performed in a modern office building for PAN propagation channels. The measurement campaign covers two frequency bands (center frequencies of 2.6 and 5.2 GHz).
- We compare the results for several different PAN scenarios, using several different types of multi-antenna devices (access points, handheld devices, laptops and a bodyworn device).
- We show the impact of typical antenna arrangements, as well as the influence of the human operator of the antenna device. Especially, we find that the generalized gamma distribution should be used to describe the small-scale fading, since neither Rayleigh nor Ricean distributions give a satisfactory description of the fading statistics.
- We introduce and motivate a distinction between body-shadowing and environment shadowing, and experimentally verify this concept.
- We provide a complete statistical model for the two types of shadowing and the small-scale fading statistics.

Though all measurements in our campaign are done with multiple-antenna devices, an evaluation of MIMO correlation matrices and resulting capacity analysis is relegated to a separate paper.

The remainder of the paper is organized the following way: Section II describes the setup for the measurements, and the physical environment in which the measurements were made. Section III describes the model parameters as well as how they are extracted from the measurements. Also, a discussion about the different types of shadowing, and explanations why different types of movement lead to different values of shadowing is included. Section IV presents measurement results and extracted channel parameters of interest, whereas Section V describes our model based on the results from the previous section. Finally, a summary and conclusions in Section VI wraps up this paper.

II. Measurement Setup

The measurements were done with the RUSK LUND channel sounder that performs MIMO measurements based on the "switched array" principle [14]. Two different frequency bands were investigated, 2.6 ± 0.1 GHz and 5.2 ± 0.1 GHz, each of which was measured at 321 equidistantly spaced frequency points. The RUSK sounder allows to adjust the length of the test signal, and for these measurements a value of 1.6 μs was used, corresponding to a resolvable "excess runlength" of multipath components of 480 m, which was more than enough in our considered environment to avoid overlap of subsequent impulse responses. In order to gather a large number of channel samples, the receiver unit was slowly moved over a small area during each measurement (details of the movement will be described in Sec. II-C) allowing the channel sounder to record 10 different channel samples, or snapshots, with small spatial offsets. The output power of the channel sounder was 0.5 W, and we made sure that the received signal level always was within the allowable limits of the sounder.

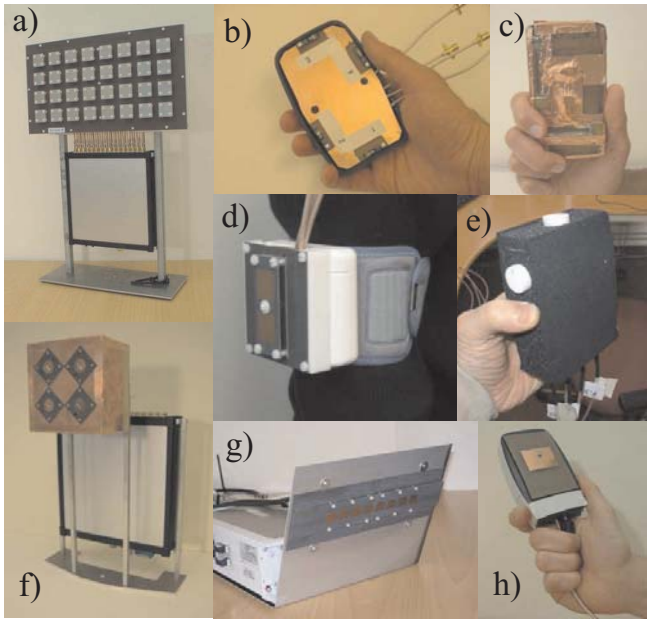

Fig. 1. The antennas used in the measurements: a) 2.6 GHz access point; b) 2.6 GHz 4-element handheld device (with the plastic lid removed in order to expose the antennas); c) 5.2 GHz 4-element handheld device; d) 5.2 GHz bodyworn device; e) 5.2 GHz 6-element handheld device; f) 5.2 GHz access point; g) laptop dummy, here with the 5.2 GHz array mounted; h) 2.6 GHz 2-element handheld device.

Several antenna arrays were used for each frequency band. The different arrays where designed with an intention of resembling realistic multi-antenna consumer devices as much as possible. Hence, we used access point (AP) arrays, handheld (HH) device arrays (similar to personal digital assistants, PDAs, or mobile phones), laptop computer (PC) arrays and a body worn (BW) device array (similar to a blood-pressure gauge) and by using different combinations of antenna devices as Tx and Rx, four different scenarios were created. The following sections describe the different antenna arrays, the measurement environment and the scenarios in greater detail.

A. Antenna Devices

In total, 11 different antenna devices were used throughout the measurement campaign (see Fig. 1). Hereinafter, the array size is, where applicable, given as (number of rows $\times$ number of columns $\times$ number of polarizations per antenna element).

1) Access Point – 2.6 GHz: The 2.6 GHz access point was a $(4 \times 8 \times 2)$ antenna array consisting of quadratic, dual-polarized, microstrip antennas. Only the middle two rows were used during the measurements, and the ports of the other two where terminated with 50 Ω-terminations. The array

was tripod-mounted at ceiling height in order to increase the resemblance with a real access point.

2) Laptop Computer – 2.6 GHz: This device consisted of a $(1 \times 4 \times 2)$ array of the same sort of elements as the 2.6 GHz AP, mounted on a laptop dummy (a laptop-shaped metal frame). The array was placed on the reverse side of the "screen", with the broadside direction aiming away from the "keyboard". Since the "screen" was tilted slightly backwards (in order represent a typical laptop pose), so was the antenna array.

3) Handheld Device – 2.6 GHz: Two different handheld devices were used, one with 2 elements and one with 4 elements. The latter device, used in the AP/HH/PC to HH scenarios, consisted of a plastic box containing a ground plane and 4 PIFAs, one on each edge of the ground plane. The element on the rightmost edge (see Fig. 1b) was constantly covered by the hand during the measurements and was therefore disregarded in the analysis. The 2-element array, used only in the HH to HH scenario, consisted of an identical plastic box, equipped with 2 rectangular patch antenna elements with orthogonal polarization, mounted on opposite sides on the outside of the box (see Fig. 1h).

4) Access Point – 5.2 GHz: A $(2 \times 2 \times 2)$ array of dual-polarized, circular microstrip antennas was used as the 5.2 GHz access point, tripod-mounted in the same way as in the 2.6 GHz case.

5) Laptop Computer – 5.2 GHz: The metal frame of the corresponding 2.6 GHz scenario was also used at 5.2 GHz, though equipped with a $(1 \times 8 \times 2)$ array of dual-excited microstrip element.

6) Handheld Device – 5.2 GHz: Four antenna devices, of two different types, were used. The first type of HH was a 4-element slot antenna array (denoted HH_4), consisting of a metal box with built-in slot antenna elements; two in the front of the box, perpendicular to each other, one in the top side, and one in the right side of the box. The front left element of one HH_4 was found to give abnormal results, and was therefore disregarded in the analysis. This device is thus denoted HH_3. The second type of HH was a 6-element circular patch antenna array (denoted HH_6). Three dual-polarized antennas were mounted outside a foam-clad metal box; one on the left side, one on the top side, and one on the right side.

7) Bodyworn Device – 5.2 GHz: As a bodyworn device, we used a $(2 \times 1 \times 2)$ array of the same type of microstrip elements used for the 5.2 GHz PC. The array was mounted on top a plastic box (originally a blood-pressure gauge), attached to a strip of Velcro tape enabling wearing of the device.

B. The Office Environment

The measurements were performed in an office environment in the E-building at Lund University, Lund, Sweden. Office floor sizes are between 10 m^2 and 30 m^2, where the outer walls of the building consist of brick and reinforced concrete, whereas gypsum wallboards separate different offices. Throughout the offices, different Tx and Rx positions were selected to constitute realistic usage situations with a Tx-Rx separation less than 10 m. All scenarios could not share the exact same set of positions, since what is regarded as a realistic position for a certain type of antenna device, may not be very realistic for another. The same set of positions was used for the AP to HH and AP to BW measurements, whereas the PC to HH scenario only used a subset of these. The HH to HH scenarios used their own set of positions, as shown in Fig. 2.

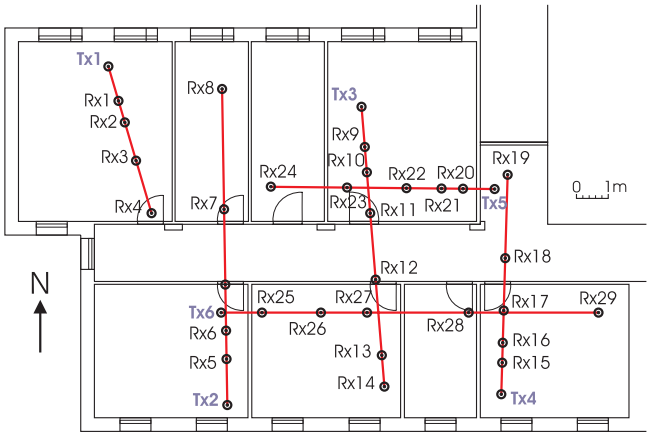

Fig. 2. Site map of the measurement positions for the HH to HH scenarios. Measurements were only recorded between positions along the lines.

The shadowing impact of the human operator discussed earlier also leads to an ambiguity in the definition of "line-of-sight" (LOS), as it is not obvious if a channel where the shortest propagation path between Tx and Rx is obstructed by one or several human operators should be counted as LOS or not. We choose to separate our measurements into LOS and NLOS according to a definition where a measurement is considered LOS when the *operators* are within line-of-sight of each other.

C. Measurement Scenarios

In this section we describe the different measurement scenarios; the common features of the various setups are summarized in Table I, where N_{meas} is the total number of measurements per scenario, N_{Tx} the number of Tx positions and N_{Rx} the number of Rx positions (given as LOS/NLOS). Furthermore, "Tx or." and "Rx or." are the measured Tx/Rx orientations, respectively.

1) Access Point to Handheld Device (AP2HH): In this scenario, the AP was used as Tx. Five different Tx/AP positions were selected amongst the offices along with 20 Rx/HH positions. Three AP positions were used for NLOS measurements, whereas two were used to create LOS situations. For each NLOS Tx position, measurements were made at every (NLOS) HH position within a 10 m range, whereas for the LOS AP positions, measurements were made at each HH position within LOS. During the measurements, the HH was held by a person seated in front of a desk (at 5.2 GHz, the HH_3 and one HH_6 was simultaneously held, one in each hand), and in order to capture the effects of orientation with respect to the AP as well as the shadowing of the operator's body, four different measurements were made at every HH position. These measurements were made with different orientations of the person holding the HH; orientations of 0° (the person facing the desk), 90°, 180° and 270° were measured. In order to obtain ten channel snapshots, the human operator moved

TABLE I
MEASUREMENT SCENARIOS.

Scenario	N_{meas}	Tx unit	N_{Tx}	N_{Rx}	Tx or.	Rx or.		
AP2HH	44/192	AP	2/3	11/18	–	0°, 90°, 180°, 270°	rel. to	desk
PC2HH	96/–	PC	5/–	19/–	–	0°, 90°, 180°, 270°	rel. to	desk
HH2HH	180/90	HH	4/2	20/10	60°, 180°, 300°	60°, 180°, 300°	rel. to	Rx/Tx
AP2BW	44/124	AP	2/2	11/18	–	0°, 90°, 180°, 270°	rel. to	desk

the HH(s) in front of his body over an area of approximately 30×30 cm^2.

2) Laptop Computer to Handheld Device (PC2HH): This scenario used the PC as Tx and was limited to LOS measurements only. Five Rx positions of the AP to HH scenario, one in each office, were used as Tx/PC positions, and measurements were made at all HH positions within LOS. The stance of the person holding the antenna(s) (the HH_3 and one HH_6 at 5.2 GHz) the principle of measuring four different orientations of the antenna carrier, and the obtaining of ten channel snapshots were the same as for the AP to HH scenario.

3) Handheld Device to Handheld Device (HH2HH): For the HH to HH scenario, both Tx and Rx were held by standing persons (at 5.2 GHz, either person was equipped with a $HH_{3/4}$ *and* a HH_6). LOS situations were created using 4 Tx and 20 Rx positions, whereas NLOS measurements were made with 2 Tx and 10 Rx positions (see Fig. 2). Similar to previous scenarios, measurements with different antenna orientations were made in order to capture the effects of body shadowing. In this scenario, however, both Tx *and* Rx (or rather the antenna-carrying persons) were varied over an ensemble of different orientations; $60°$, $180°$ and $300°$ (with $0°$ denoting the bearing to the other antenna carrier). Hence, nine measurement were made for every Tx-Rx position. Ten snapshots were obtained by moving the Rx device(s) in the same way as in the AP to HH scenario.

4) Access Point to Bodyworn Device (AP2BW): In the AP to BW scenario, the AP was used as Tx. The measurement points as well as the orientations of the antenna device carrier were the same as in the AP to HH scenario (though one Tx position less was used for NLOS). The BW was carried around the right biceps of the carrier, facing away from the body. To obtain ten channel snapshots, the carrier moved his torso slowly over an area of approximately 30×30 cm ^{2} during the measurements.

III. MODEL PARAMETERS AND DATA EVALUATION

The standard model for fading, i.e., fluctuations in the received power of a wireless channel, is the combined effect of two processes: the small-scale fading and the large-scale fading, also known as shadowing [15]. The former is due to the constructive and destructive interference of the multipath components (MPCs) impinging of the receiver, and is thus related to the relative *phases* of the multipath components. The latter is due to changes in the average *power* of the multipath components; it is typically assumed to be due to large-scale variations in the physical environment of the receiver. Since the channel sounder performs measurements in the frequency domain, we have for each measurement location (with a Tx-Rx separation d; consisting of O orientations each consisting of $S = 10$ snapshots), a channel transfer function for snapshot s of orientation o of the transmission between Rx element m and Tx element n defined as $H = H(f, d, o, s, m, n)$. Based on the transfer functions, we extract information about the fading as described in the subsequent sections.

A. Shadowing

Traditionally, variations of the shadowing are assumed to occur when the mobile station moves (laterally) over large distances, and are described as a random process with a lognormal amplitude probability density function. In PANs a strong impact of the human presence in the near field of its antennas can be expected and hence one or several human bodies are likely to lead to shadowing in a wireless PAN channel. Human presence in a wireless channel, even with handheld devices, is not a new problem and has been studied for cellular networks for quite some time. However, the common method of including the human impact is as a time-invariant "bulk attenuation factor" (see e.g., [16]); variations of the shadowing due to rotation by the user have to the best of our knowledge not been modeled statistically. Furthermore, PANs also show an additional mechanism for shadowing variations as the relative position between the body and a handheld device can change frequently.

We also note that the used device and antenna types affect the amount of shadowing inflicted by the human body, as the antenna patterns determine how much power will be received or transmitted through the body of the operator. It is also of importance where the antennas are mounted and how they are directed with respect to the body, and hence, the human body will, depending on the exact locations of Tx, Rx and human operator, add a different amount of shadowing on the received power. Thus, the assumption of the shadowing experienced by a receiver being constant for each Tx-Rx position is no longer valid: if a person rotates, the amount of shadowing will change markedly. The total shadowing induced by the channel will thus be the sum of two parts, and hence it is reasonable to separate two types of shadowing: 1) the power variations due to the physical surroundings around Tx and Rx, and 2) the power variations due to the changes of body shadowing induced by the operator of the device.

To investigate the influence of rotations and body shadowing, we determine the path gain for two cases: the *total* path gain $G_{\text{tot}}(d)$ is defined as the average of $|H|^2$ over antennas, frequency, snapshots and orientation, while the *local* path gain $G_i(d, o)$ is defined as the average of $|H|^2$ over antennas, frequency and snapshots. By fitting a deterministic distance decay $G_{\text{det}}(d)$ to describe the distance dependence of $G_{\text{tot}}(d)$, the shadowing loss due to the environment, L_e, is defined as the local variation of $G_{\text{tot}}(d)$ around $G_{\text{det}}(d)$, and the shadowing loss due to the body/orientation, L_b, is defined as the local variations of $G_i(d, o)$ around $G_{\text{tot}}(d)$.

B. Small-Scale Fading

The small-scale amplitude variations are analyzed from frequency domain data, i.e., from the channel transfer functions. On most antenna arrays that we use, different antenna elements have different directions or polarizations, and for that reason, separate small-scale analysis is done for each Tx-Rx antenna element pair (or *spatial channel*).

First, we want to characterize the relative path gain of each spatial channel, G_{r}, i.e., the mean power of each spatial channel (over snapshots and frequency) relative the mean power over all spatial channels within a measurement. Then, to evaluate the small-scale amplitude variations around G_{r}, we use an ensemble of frequency sub-channels *and* snapshots (i.e., 3210 channel samples) as the basis for analysis.[2] We normalize the amplitude data $r = |H|$ to unit power, i.e., $E\left(r^2\right) = 1$, fit the data to three possible distributions and select the best fit. The three candidate distributions we consider are the Rayleigh distribution, the Rice distribution and a mixed distribution to account for situations that are neither Rayleigh nor Ricean. While a number of different distributions are possible for the latter case, we choose here the generalized gamma (GG) distribution [18], whose pdf is

$$p_R(r) = \frac{c r^{c\alpha-1}}{\beta^{c\alpha}\Gamma(\alpha)} \exp\left[-\left(\frac{r}{\beta}\right)^c\right], \tag{1}$$

where $\Gamma(\sim)$ is the Gamma function, because of its simple functional form. With a proper choice of its three parameters α, β and c, the GG distribution can represent a wide variety of distributions including the Rayleigh and the Rice case.[3] Fitting of the different distribution parameters is done by means of maximum-likelihood (ML) estimation. Since no closed-form expression exists for the Ricean K-factor, ML estimates are obtained by stepping through a range of values from 0.1 to 20 and selecting the one that maximizes the log-likelihood function. For the GG distribution, the ML estimates of α, β and c can be shown to fulfill [19]

$$\hat{\beta} = \left(\frac{1}{N\hat{\alpha}}\sum_{n=1}^{N} x_n^{\hat{c}}\right)^{1/\hat{c}}, \tag{2}$$

$$\frac{1}{\hat{\alpha}} = \hat{c}\left(\frac{\sum_{n=1}^{N} x_n^{\hat{c}} \ln x_n}{\sum_{n=1}^{N} x_n^{\hat{c}}} - \frac{1}{N}\sum_{n=1}^{N} \ln x_n\right). \tag{3}$$

Numeric ML estimates can thus be derived by stepping through a range of c-values (from 0.1 to 10), determining the corresponding α and β from Eqs. (2) and (3), and selecting the set of $\{\alpha, \beta, c\}$ that maximizes the log-likelihood function.

After deriving the ML estimates of the parameters for each candidate distribution, we use Akaike's Information Criterion (AIC) [20] to derive its corresponding Akaike weight. As the latter is interpreted as the probability that the candidate distribution gives the best fit, we thus regard the pdf with the largest weight as the one giving the best fit to our data.

[2]With the delay spreads we measure in these scenarios (10–12 ns), the corresponding (0.5–)coherence bandwidth ensures that we have enough independent frequency samples for the analysis (the measured bandwidth of 200 MHz implies 11–13 independent samples per snapshot, i.e., a total of 110–130 per ensemble) [17].

[3]Though the Rice pdf cannot be *exactly* represented by a generalized gamma, it indeed constitutes a very good approximation [18].

C. Delay Dispersion

In order to analyze the delay dispersion of the channel, we convert the channel transfer functions to impulse responses by means of an inverse Fourier transform (using a Hanning window) from which we derive the averaged power delay profiles (APDPs), $\bar{P}(\tau)$, as the square magnitude of the impulse responses averaged over snapshots and antennas.[4] Preceding our results section, we note that the APDP of our measurements can be well described by a single-exponential (SE) decay, i.e., $\bar{P}(\tau) = \bar{P}_0 e^{-\tau/\gamma}$ where γ is the decay time constant. An important and convenient implication of the SE decay model, is that decay time constant equals the rms delay spread of the channel (defined as the second central moment of the APDP; see e.g., [15]). We therefore choose to extract the decay time constant instead of the rms delay spread, because it is less sensitive to noise floor influence [21]. The decay constant values are extracted by fitting regression lines to the APDPs on a dB scale.

IV. Results

A. Pathloss and Shadowing

The (deterministic) distance dependent power decay is modeled, in dB, as

$$G_{\mathrm{det}}(d) = G_0 - 10n\log_{10}(d/d_0), \tag{4}$$

where G_0 is the path gain at a distance $d_0 = 1$ m and n is the pathloss exponent. Fig. 3 shows a scatter plot of the total and local path gain, $G_{\mathrm{tot}}(d)$ and $G_i(d,o)$, respectively, along with a fit of $G_{\mathrm{tot}}(d)$ to Eq. (4) for the 5.2 GHz HH_6 to HH_6 LOS measurements. We draw two important conclusions from the figure: (i) our theory of two types of shadowing is confirmed – the local power variations of $G_i(d,o)$ around $G_{\mathrm{tot}}(d)$ can be clearly seen from the figure; (ii) the distance dependence is weak, compared to the variations around it – for scenarios with a low pathloss exponent, the signal attenuation due to the antenna direction can prove to be a factor of greater importance than the signal attenuation due to increasing distance. The extracted pathloss exponent is between 0.2 and 1.4 for all but one LOS scenarios, whereas for NLOS scenarios, the distance dependence is stronger, with pathloss exponents between 1.7 and 2.7.

The shadowing loss L_{e} due to the environment is found to be reasonably well described by a log-normal distribution (i.e., by using a χ^2–test with a 1% significance level, we find that the dB values of L_{e} can be described as Gaussian with a standard deviation $\sigma_{L_{\mathrm{e}}}$) as can be seen in Fig. 4. Another χ^2–test with the same significance level reveals that the dB values of the body shadowing loss L_{b} also can be described by a Gaussian distribution, with a standard deviation $\sigma_{L_{\mathrm{b}}}$ (see Fig. 4). The pathloss and shadowing model parameters are given in Table II, and from the table we note that the body shadowing variance is constant irrespective of whether the measurement is LOS or NLOS. Also, with the exception of the HH to HH scenario, all model parameters are fairly constant over the two frequency ranges. Furthermore, by comparing

[4]By averaging over the antenna elements, we thus choose to neglect the aforementioned influence of the antenna arrangements in this part of the analysis.

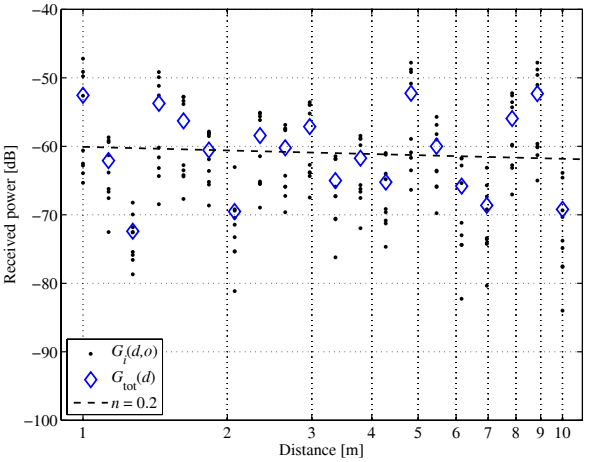

Fig. 3. Scatter plot of the received power vs. distance for the 5.2 GHz HH_6 to HH_6 LOS measurements.

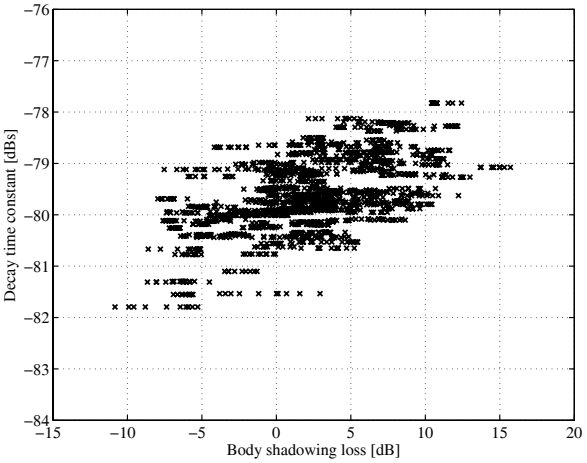

Fig. 5. Correlation between body shadowing loss and decay time constant for the 5.2 GHz HH_3 to HH_4 LOS measurements. The correlation coefficient in this case is 0.56.

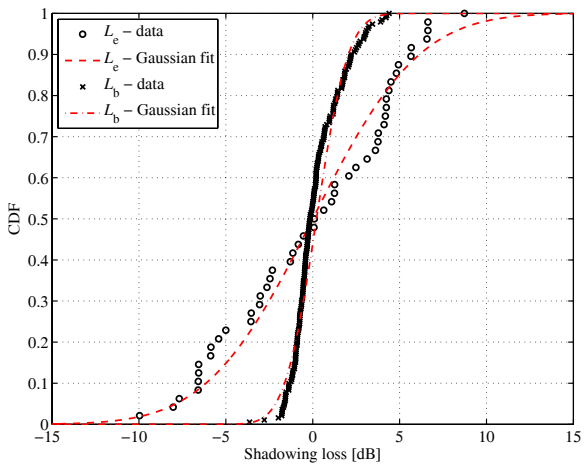

Fig. 4. Cdf:s of the shadowing loss due to the environment, L_e, and the body shadowing loss, L_b, for the 5.2 GHz AP to HH_6 NLOS measurements.

the results of e.g., $AP2HH_3^{5.2}$ and $AP2HH_6^{5.2}$, we note that the difference between the different types of handheld devices is small, even though they use different antenna types as well as array design.

B. Power Delay Profile

Since it has previously been reported in the literature [22] that delay spread and shadow fading are correlated, we seek to investigate if this is the case for both types of shadowing. Noting that the APDP of our measurements consists of a single, exponentially decaying cluster,[5] we thus evaluate this, following the reasoning from Sec. III-C, by deriving the correlation between the two types of shadowing and the decay time constant γ instead.

The results reveal that there is (with one exception) a positive correlation between both types of shadowing and the delay spread for all measured scenarios, i.e., the shadowing loss increases for increasing delay spread (see Fig. 5). Excluding the 2.6 GHz HH to HH scenario (which has a correlation coefficient of -0.12), the correlation coefficient between $L_e|_{dB}$ and $\gamma|_{dB}$ lie between $0.32 - 0.78$ for LOS and $0.16 - 0.54$ for NLOS, whereas the correlation coefficients between $L_b|_{dB}$ and $\gamma|_{dB}$ lie between $0.26 - 0.58$ for LOS and $0.17 - 0.40$ for NLOS.

Returning to the decay time constant, we do not see any distance dependence, as has been reported in previous measurement campaigns [22], but instead choose to model γ as a random variable. Using a χ^2–test with a 5% significance level, we find that within each scenario, the variations of the decay time constant *in dB* can be well described by a Gaussian distribution (see Fig. 6). We thus have $\gamma|_{dB} \sim N(m_\gamma, \sigma_\gamma)$ with constant values given by Table II. We note that there is essentially no difference between different scenarios, which is reasonable since the delay spread of the channel is mainly determined by the environment and not the antenna arrangements.

C. Small-Scale Fading Statistics

A study of the histograms of the received amplitudes (using frequency subchannels *and* snapshots) for the different spatial channels of a measurement, allows us to draw two conclusions: (i) *within the same measurement*, the statistics of different spatial channels can be quite different, and (ii) the Rice and Rayleigh distributions cannot completely describe it. Fig. 7 shows the statistics for the 3×4 spatial channels of a LOS measurement from the 5.2 GHz HH_3 to HH_4 scenario (using frequency subchannels *and* spatial snapshots as ensemble). Comparing with the best-fit Rice and Rayleigh distributions (also plotted for each ensemble), we note that, within the same *LOS* measurement, only a few spatial channels are well described by a Rice distribution (with a reasonably high K–factor), whereas others are better described by a Rayleigh. Since the antenna patterns are fairly directive (and with the placement of the antenna elements in mind), a

[5]Note that due to the idiosyncrasies of measuring PAN channels, it is not possible to use the angular domain for a more refined identification of clusters.

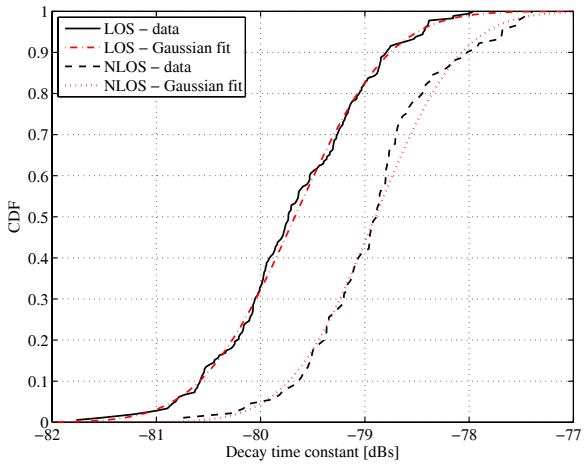

Fig. 6. Cdf:s of the decay time constants γ from the 2.6 GHz HH to HH scenario, LOS as well as NLOS data.

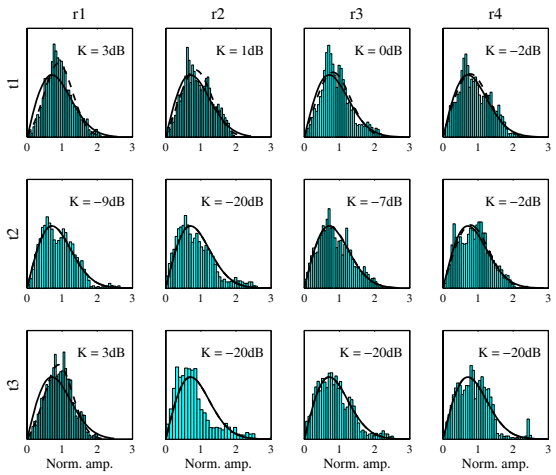

Fig. 7. Amplitude statistics for all spatial channels from the 5.2 GHz, HH_3 to HH_4, Tx4 to Rx18 measurement (see Fig. 2). The figure is organized as a matrix with Tx elements (t1, t2,...) as rows and Rx elements as columns (r1, r2,...; the indices are written in the left and top perimeter). For each ensemble (snapshots *and* frequency samples), a Ricean fit (dashed; with the ML K-factor given) and a Rayleigh fit (solid) is shown.

possible explanation for the lack of Ricean channels can be that the antenna gain in the direction of the optical LOS is very poor for some antenna elements, and hence the signal strength of the optical LOS path becomes weak compared to the reflected paths. However, and more importantly, we also note that some channels are poorly described by a Rayleigh as well as a Ricean (e.g., t3 to r2 in Fig. 7).

To get further insight into the cases that are, clearly, neither Ricean nor Rayleigh, we investigate the amplitude statistics of each snapshot separately, i.e., we use *only* the (321) frequency subchannels as the ensemble for analysis. The results show that there is also a clear difference in the statistics of different *snapshots*, where some are well described by a Rice distribution, whereas others are better described by a Rayleigh distribution. Thus the total small-scale amplitude variations over the snapshots becomes a mixture of Rice and Rayleigh

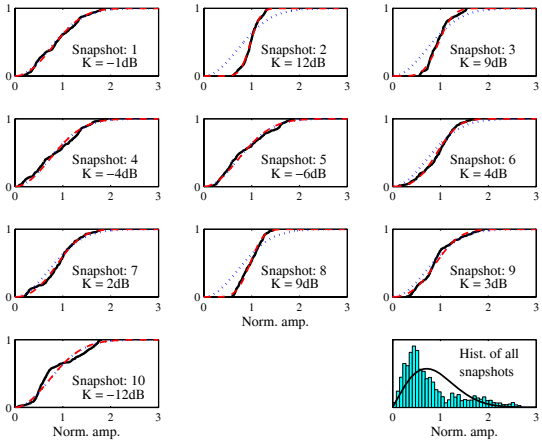

Fig. 8. Cdf:s of the snapshot amplitude statistics for one spatial channel from the 5.2 GHz, HH_3 to HH_4, Tx3 to Rx9 measurement. The solid lines are measured data, the dashed lines are best fit Ricean distributions (with the ML $K-$factor given), whereas the dotted lines are best fit Rayleigh distributions. It is clearly seen that different snapshots have different statistics.

samples. The shifting between Ricean and Rayleigh would be obvious for cases where either of the antenna device holders are facing away from the other, and the small motion of the Tx device could make the optical LOS path between the antennas alternate between unobstructed during some snapshots, and obstructed by the body of the device holder during others. However, this effect is also present in measurements were both human bodies are clearly out of the way. Fig. 8 shows cdf:s of the snapshot amplitude distributions from a LOS measurement (again from the 5.2 GHz, HH_3 to HH_4 scenario) where Tx and Rx are separated by only 1 m and the device holders are facing each other. We note that snapshots 2, 3 and 8 appear Ricean distributed while the others rather are Rayleigh distributed. A possible explanation for this could be the directivity of the antenna elements and the influence of the device holder's arm. Since the arm in practice becomes a part of the antenna, the radiation pattern is likely to change slightly with the small-scale movement of the device, and hence, the antenna gain in the optical LOS will change from snapshot to snapshot.

It is thus a noteworthy result from our measurements that the statistics of the ensemble created by the different frequency samples are different from the statistics of the ensemble created by also using the snapshot (or temporal) samples. Consequently, the concept of frequency ergodicity, as introduced by Kattenbach [23], becomes invalid in this case. With only 10 spatial samples available, a complete model for the K –factor variations cannot be derived in a satisfactory way. However, by looking at the variations of the *mean* and *standard deviation* of the ML estimated $K-$factor (in dB) within each spatial channel, denoted $\bar{K}_{\text{dB}}$ and $\sigma_{K_{\text{dB}}}$, respectively, we can make a coarse analysis of the $K-$factor fluctuations. The mean of $\sigma_{K_{\text{dB}}}$, over spatial channels and measurement positions, is varying between 4.5 and 6.0 dB for the different LOS scenarios and between 4.9 and 5.6 dB for the NLOS scenarios, and we thus note that the $K-$factor variations within a spatial channel generally are high.

The mean value of $\bar{K}_{\mathrm{dB}}$ is varying between -2.2 and 1.5 dB for the LOS scenarios whereas the mean value for the NLOS scenarios lie between -3.8 and -1.5 dB.

For many applications, it is still of interest to consider the statistics of the ensemble of snapshots and frequency. Thus, the amplitude data is fitted to a Rayleigh distribution, a Rice distribution and a GG distribution and we determine which distribution that best describe each ensemble by using the Akaike weights as described in Sec. III-B. Using the distribution with the highest weight (i.e., probability of being the best fit) as test outcome, we conclude that the GG distribution is regarded as the best fit in a clear majority of the cases (around $60-70\%$), whereas the remainder of the test outcomes are evenly spread over Ricean and Rayleigh. For those reasons, we use the GG distribution model the small-scale statistics and thus focus on how to select the distribution parameters.

As previously mentioned, the GG distribution is controlled by the three parameters, α, β and c, where c controls the upper part of the pdf, and αc controls the lower part. It can be shown [18] that

$$\beta = \sqrt{E\left(r^2\right)\frac{\Gamma\left(\alpha\right)}{\Gamma\left(\alpha+2/c\right)}} = \sqrt{\frac{\Gamma\left(\alpha\right)}{\Gamma\left(\alpha+2/c\right)}} \tag{5}$$

where the last equality stems from the fact that we use normalized data. Since this relation is maintained in the ML estimation process, we have $\beta = \beta\left(\alpha, c\right)$ and thus only need a model for α and c.

While there might be correlation between the fading of adjacent spatial channels, this aspect is beyond the scope of the current paper where we restrict ourselves to modeling the fading of a single link. No significant correlation is found between the small-scale parameters (α, c and the relative path gain G_{r}) and the two shadowing types or the Tx-Rx separation, but by using a χ^2–test with a 5% significance level, we find that for each spatial subchannel, the *dB-values* of α and c can be well described as (strongly) correlated Gaussian random variables (see Figs. 9 and 10).[6] Another χ^2–test shows that G_{r} *in dB* also can be described by a Gaussian (see Fig. 9), and since we do not find any correlation between G_{r} and α or c, we choose our model as

$$\left[\begin{array}{ccc} \alpha & c & G_{\mathrm{r}} \end{array}\right]^T \sim \mathcal{N}\left(\mu, \mathbf{C}\right) \tag{6}$$

with a mean value matrix

$$\mu = \left[\begin{array}{ccc} \mu_\alpha & \mu_c & \mu_{G_{\mathrm{r}}} \end{array}\right]^T \tag{7}$$

and a covariance matrix

$$\mathbf{C} = \left[\begin{array}{ccc} R_{\alpha\alpha} & R_{\alpha c} & 0 \\ R_{\alpha c} & R_{cc} & 0 \\ 0 & 0 & R_{G_{\mathrm{r}}G_{\mathrm{r}}} \end{array}\right]. \tag{8}$$

Parameter values for the small-scale fading model, derived as the average over all spatial channels within each scenario, are given in Table II.

[6]In a few cases ($< 1\%$ of the outcomes), the ML estimation process failed to create meaningful results, by means of leading to a monotonically decreasing log-likelihood function (for an increasing c). Thus, the smallest value of the c-stepping range (0.1 in our case) was returned from the estimator, and as these results are obviously unphysical, they were disregarded in the analysis.

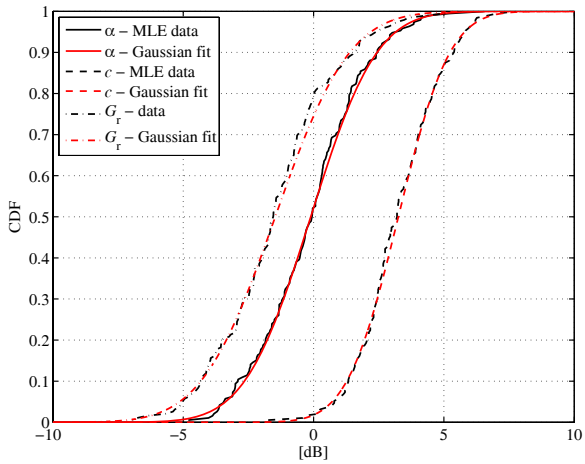

Fig. 9. Extracted smallscale parameters for one spatial channel of the 5.2 GHz AP to HH_6 NLOS measurements. Also shown are Gaussian fits to the data.

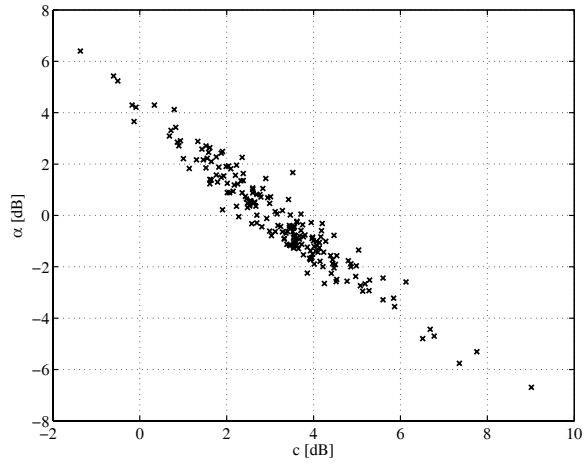

Fig. 10. ML estimates of α and c for one spatial channel of the 5.2 GHz AP to HH_6 NLOS measurements.

The model is thus based on the observation that the irregular antenna arrangements create unpredictable small-scale fading statistics, an observation that is true for all but one of the measured scenarios – the AP to BW scenario. This is not surprising, since this is a scenario where neither Tx nor Rx does in fact have an irregular antenna arrangement, rather all spatial channels can be characterized as co- or crosspolarized. Hence this scenario implies fading statistics that are far more predictable, and therefore this scenario is left out of our model.

V. Our Model

A realization of the complete path gain (in dB) for the spatial channel between Tx element n and Rx element m separated by a distance d is thus given by

$$G\left(d, m, n\right) = G_0 - 10n\log_{10}\left(\frac{d}{d_0}\right) - L_{\mathrm{e}} - L_{\mathrm{b}} + G_{\mathrm{r}} + G_{\mathrm{ss}} \tag{9}$$

where L_{e}, L_{b}, and G_{r} has been defined previously, and $\sqrt{G_{\mathrm{ss}}}$ is the small-scale amplitude drawn from the generalized gamma

TABLE II
MODEL PARAMETERS.

LOS	G_0	n	σ_{L_e}	σ_{L_b}	μ_α	μ_c	μ_{G_r}	$R_{\alpha\alpha}$	$R_{\alpha c}$	R_{cc}	$R_{G_rG_r}$	m_γ	σ_γ	ρ_{L_e}	ρ_{L_b}
AP2HH$^{2.6}$	−43	1.4	2.3	2.3	−0.7	4.3	−0.6	8.4	−5.1	3.9	4.8	−80	0.4	0.6	0.4
PC2HH$^{2.6}$	−54	0.6	6.4	2.7	−0.2	3.6	−0.5	7.1	−4.0	3.3	4.0	−80	0.8	0.3	0.3
HH2HH$^{2.6}$	−47	2.7	4.2	4.2	0.1	3.1	−0.6	5.5	−3.6	2.7	3.7	−80	0.7	−0.1	0.6
AP2HH$^{5.2}_6$	−47	1.0	2.4	1.7	−0.2	4.0	−1.5	8.5	−4.5	3.4	12	−80	0.4	0.8	0.3
AP2HH$^{5.2}_4$	−47	1.2	2.7	2.2	−0.1	3.6	−1.4	6.7	−4.0	3.3	11	−80	0.4	0.7	0.3
PC2HH$^{5.2}_6$	−59	0.6	5.5	2.9	−0.1	3.6	−1.6	10	−5.8	4.5	13	−80	0.8	0.6	0.4
PC2HH$^{5.2}_4$	−60	0.7	5.4	3.7	0.2	3.2	−1.2	10	−6.2	4.5	9.2	−80	0.8	0.4	0.4
HH2HH$^{5.2}_6$	−60	0.2	6.2	5.5	0.3	3.1	−2.3	7.5	−4.2	3.2	21	−80	0.8	0.5	0.6
HH2HH$^{5.2}_4$	−60	0.3	6.3	4.6	0.4	2.9	−1.1	7.1	−4.6	3.4	8.7	−80	0.7	0.6	0.6
NLOS															
AP2HH$^{2.6}$	−48	2.0	5.1	2.2	−0.4	3.5	−0.6	6.0	−4.1	3.1	4.0	−79	0.6	0.5	0.2
HH2HH$^{2.6}$	−55	2.2	3.6	3.6	0.3	2.9	−0.4	4.3	−2.9	2.2	2.7	−79	0.6	0.4	0.4
AP2HH$^{5.2}_6$	−54	1.7	4.8	1.5	0.0	3.2	−1.2	4.9	−3.2	2.4	8.9	−79	0.5	0.5	0.2
AP2HH$^{5.2}_4$	−54	1.8	4.7	2.1	0.3	2.9	−0.7	5.1	−3.3	2.4	5.8	−79	0.5	0.4	0.2
HH2HH$^{5.2}_6$	−53	2.6	2.9	4.3	0.6	2.7	−1.7	4.8	−3.1	2.3	15	−79	0.7	0.2	0.4
HH2HH$^{5.2}_4$	−53	2.7	2.7	3.6	1.1	2.2	−2.3	6.0	−4.1	2.9	14	−79	0.7	0.2	0.3

distribution. How to generate data can be summarized as follows:

1) For each Tx-Rx separation d, derive the deterministic path gain from Eq. (4), and subtract a shadowing loss caused by the environment, $L_e \sim \mathcal{N}(0, \sigma_{L_e})$.
2) Next, for every simulated orientation of a user, subtract an additional body shadowing loss $L_b \sim \mathcal{N}(0, \sigma_{L_b})$.
3) For each (uncorrelated) spatial channel, add a relative gain G_r and derive the pdf of its small-scale statistics by drawing α, c and G_r according to Eq. (6). Finally, to account for the small-scale effects, add a small-scale channel gain G_{ss} by generating $\sqrt{G_{ss}}$ from the generalized gamma pdf determined by α, c and β, where the latter is given by Eq. (5).

Additionally, the model can be extended by deriving a SE power delay profile with a Gaussian distributed decay constant (in dBseconds) having a correlation to both types of shadowing.

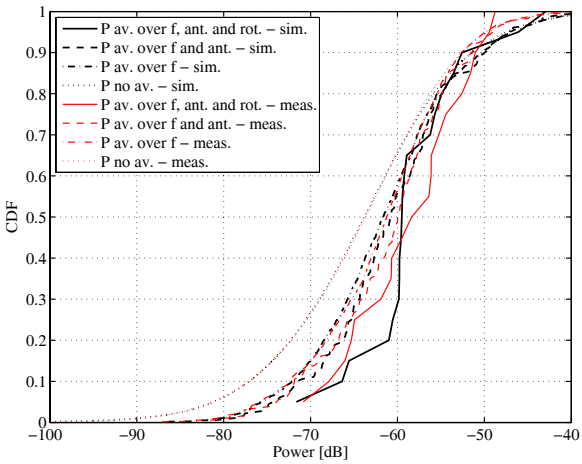

Fig. 11. Comparison of modeled and measured power for the 5.2 GHz HH_3 to HH_4 LOS scenario.

A. Validation of Model

To verify the agreement of model and measurements, we derive, for each scenario, the same number of channel realizations as measured, and compare with the measured results. The metrics we use for comparison are cdf:s of the simulated received power, evaluated for four cases: (i) averaged over frequency, (ii) averaged over frequency and spatial channels, (iii) averaged over frequency, spatial channels and rotations, and (iv) without averaging. We find that the agreement between measurements and model is very good, as can be seen in Fig. 11, where simulation results for the 5.2 GHz HH_3 to HH_4 scenario are displayed.

VI. Summary and Conclusions

We have reported results from an extensive channel measurement campaign, where scenarios, antenna arrangements, and choice of locations have been selected in order to correspond to typical PANs. Measurements were performed over two frequency ranges, using a multitude of multi-antenna devices combined in various ways to create several different scenarios. Our results show that PAN channels exhibit fundamental differences in the structure of large-scale as well as small-scale fading statistics, namely that:

- Due to the impact of the irregular antenna arrangements and the impact of the (antenna device) users typically involved in PANs, the small-scale varying amplitude is sensitive to even very small movements. Hence, a spatial channel is likely to fluctuate between "seeing" a Rayleigh and a Ricean environment, and thus the small-scale amplitude variations over a small area cannot be described by the Rayleigh our Rice distribution alone. Rather a mixed distribution has to be used; in this paper we have used the generalized gamma distribution as a model.
- It is suitable to distinguish between two types of shadowing; (i) body shadowing (due to the rotation of the device holder) and (ii) shadowing due to the physical environment (lateral movement).

The second observation was present in all of the measured scenarios, whereas the first was present in all scenarios except the AP to BW scenario, in which the antenna devices we

used caused far more predictable small-scale statistics. The small differences between LOS and NLOS are likely due to the little attenuation provided by the gypsum walls separating the offices of our measurement environment. Furthermore, we have noted that:

- In the distance range considered for PANs, the impact of the distance on the received power can be minor, and shadowing effects dominate, especially for LOS situations.
- The power delay profile is well described by a single exponential, with a decay time constant (i.e., delay spread) in dB described by a Gaussian distributed random variable.
- The definition of LOS becomes ambiguous, as the obstruction of a direct propagation path between Tx and Rx can be due to the direction of the antenna, or the person holding the device.
- The channel parameters do not change significantly between the 2.6 and 5.2 GHz frequency range.

We have also created and parameterized a channel model based on our observations. In the model, the two types of shadowing are given as random processes, well described by log-normal distributions. Also, both types of shadowing are found to be correlated with the delay spread. The model can be used for system design and performance prediction of PAN systems.

VII. Acknowledgements

We thank Bristol University and Ilmenau University, especially Prof. Mark Beach and Prof. Reiner Thomä, for kindly letting us perform measurements with their antennas. Part of this work was funded from the MAGNET project (contract no. 507102) of the European Union, an INGVAR grant of the Swedish Foundation for Strategic Research, and a grant from the Swedish Science Council.

References

[1] J. Karedal, A. J. Johansson, F. Tufvesson, and A. F. Molisch, "Characterization of MIMO channels for handheld devices in personal area networks at 5 GHz," in *Proc. European Signal Processing Conf. 2006*, Sept. 2006.

[2] ——, "Shadowing effects in MIMO channels for personal area networks," in *Proc. IEEE Veh. Technol. Conf. 2006 Fall*, 2006.

[3] D. Bakker, D. M. Gilster, and R. Gilster, *Bluetooth End to End*, 1st ed. Wiley, 2002.

[4] A. Batra *et al.*, "Multi-band OFDM physical layer proposal," 2003, document IEEE 802.15-03/267r2.

[5] J. H. Winters, "On the capacity of radio communications systems with diversity in Rayleigh fading environments," *IEEE J. Select. Areas Commun.*, vol. 5, no. 5, pp. 871-878, June 1987.

[6] G. J. Foschini and M. J. Gans, "On limits of wireless communications in a fading environment when using multiple antennas," *Wireless Personal Commun.*, vol. 6, pp. 311-335, Feb. 1998.

[7] A. Paulraj, D. Gore, and R. Nabar, *Multiple Antenna Systems*. Cambridge, U.K.: Cambridge University Press, 2003.

[8] [Online] Available: http://www.ist-magnet.org/.

[9] V. Erceg, L. Schumacher, P. Kyritsi, A. Molisch, D. S. Baum, A. Y. Gorokhov, C. Oestges, Q. Li, K. Yu, N. Tal, B. D. Dijkstra, A. Jagannatham, C. Lanzl, V. J. Rhodes, J. Medbo, D. Michelson, and M. Webster, "TGn Channel Models," IEEE P802.11 Wireless LANs, Tech. Rep., May 2004. [Online] Available: http://www.802wirelessworld.com:8802/.

[10] J. Medbo, J.-E. Berg, and F. Harryson, "Temporal radio channel variations with stationary terminal," in *Proc. IEEE Veh. Technol. Conf. 2004 Fall*, Sept. 2004, pp. 91-95.

[11] A. Alomainy, Y. Hao, and X. Hu, "UWB on-body radio propagation and system modelling for wireless body-centric networks," *IEEE Proceedings - Commun.*, vol. 153, no. 1, pp. 107-115, 2006.

[12] A. Fort, C. Desset, J. Ryckaert, P. De Doncker, L. Van Biesen, and P. Wambacq, "Characterization of the ultra wideband body area propagation channel," in *Proc. IEEE International Conf. on Ultra-Wideband*, pp. 22-27, 2005.

[13] T. Zasowski, G. Meyer, F. Althaus, and A. Wittneben, "Propagation effects in uwb body area networks," in *Proc. IEEE International Conf. Ultra-Wideband*, pp. 16-21, 2005.

[14] R. Thomae, D. Hampicke, A. Richter, G. Sommerkorn, A. Schneider, U. Trautwein, and W. Wirnitzer, "Identification of the time-variant directional mobile radio channels," *IEEE Trans. Instrumentation and Measurement*, vol. 49, pp. 357-364, 2000.

[15] A. F. Molisch, *Wireless Communications*. Chichester, West Sussex, UK: IEEE Press-Wiley, 2005.

[16] A. F. Molisch *et al.*, "IEEE 802.15.4a channel model—final report, Tech. Rep. Document IEEE 802.15-04-0662-02-004a, 2005.

[17] T. S. Rappaport, *Wireless Communications—Principles and Practices*, 2nd ed. Upper Saddle River, NJ: Prentice Hall, 2002.

[18] R. Vaughan and J. B. Andersen, *Channels, Propagation and Antennas for Mobile Communications*. London, UK: IEE, 2003.

[19] H. W. Hager and L. J. Bain, "Inferential procedures for the generalized gamma distribution," *J. American Statistical Assoc.*, vol. 65, no. 332, pp. 1601-1601, Dec. 1970.

[20] H. Akaike, "Information theory and an extension of the maximum likelihood principle," in *Breakthroughs in Statistics*, S. Kotz and N. L. Johnson, Eds. New York: Springer, 1992, vol. 1, pp. 610-624.

[21] J.-P. Rossi, "Influence of measurement conditions on the evaluation of some radio channel parameters," *IEEE Trans. Veh. Technol.*, vol. 48, no. 4, pp. 1304-1316, July 1999.

[22] L. J. Greenstein, V. Erceg, Y. S. Yeh, and M. V. Clark, "A new path-gain/delay-spread propagation model for digital cellular channels," *IEEE Trans. Veh. Technol.*, vol. 46, no. 2, pp. 477-485, May 1997.

[23] R. Kattenbach, "Characterization of time-variant indoor radio channels by means of their system and correlation functions," Ph.D. dissertation, University of Kassel, 1997.

Johan Karedal received the M.S. degree in engineering physics in 2002 from Lund University in Sweden. In 2003, he started working towards the Ph.D. degree at the Department of Electrical and Information Technology, Lund University, where his research interests are on channel measurements and modeling for MIMO and UWB systems. Johan has participated in the European research initiative "MAGNET".

Anders J Johansson received his Masters, Lic. Eng. and Ph.D. degrees in electrical engineering from Lund University, Lund, Sweden, in 1993, 2000 and 2004, respectively. From 1994 to 1997 he was with Ericsson Mobile Communications AB developing transceivers and antennas for mobile phones. Since 2005 he is an Associate Professor at the Department of Electrical and Information Technology at Lund University. His research interests include antennas, wave propagation and telemetric devices for medical implants as well as antenna systems and propagation modeling for MIMO systems. He is funding chair of the Swedish chapter of IEEE Engineering in Medicine and Technology section.

Fredrik Tufvesson was born in Lund, Sweden in 1970. He received the M.S. degree in Electrical Engineering in 1994, the Licentiate Degree in 1998 and his Ph.D. in 2000, all from Lund University in Sweden. After almost two years at a startup company, Fiberless Society, Fredrik is now associate professor at the Department of Electrical and Information Technology. His main research interests are channel measurements and modeling for wireless communication, including channels for both MIMO and UWB systems. Beside this, he also works with channel estimation and synchronization problems, OFDM system design and UWB transceiver design.

Andreas F. Molisch Andreas F. Molisch (S'89, M'95, SM'00, F'05) received the Dipl. Ing., Dr. techn., and habilitation degrees from the Technical University Vienna (Austria) in 1990, 1994, and 1999, respectively. From 1991 to 2000, he was with the TU Vienna, becoming an associate professor there in 1999. From 2000-2002, he was with the Wireless Systems Research Department at AT&T (Bell) Laboratories Research in Middletown, NJ. Since then, he has been with Mitsubishi Electric Research Labs, Cambridge, MA, USA, where he is now a Distinguished Member of Technical Staff and Chief Wireless Standards Architect. He is also professor and chairholder for radio systems at Lund University, Sweden.

Dr. Molisch has done research in the areas of SAW filters, radiative transfer in atomic vapors, atomic line filters, smart antennas, and wideband systems. His current research interests are measurement and modeling of mobile radio channels, UWB, cooperative communications, and MIMO systems. Dr. Molisch has authored, co-authored or edited four books (among them the textbook "Wireless Communications, Wiley-IEEE Press), eleven book chapters, more than 110 journal papers, and numerous conference contributions, as well as more than 70 patents.

Dr. Molisch is an editor of the IEEE TRANSACTIONS ON WIRELESS COMMUNICATIONS and co-editor of special issues of several journals. He has been member of numerous TPCs, vice chair of the TPC of VTC 2005 spring, general chair of ICUWB 2006, TPC co-chair of the wireless symposium of Globecomm 2007, TPC chair of Chinacom2007, and general chair of Chinacom 2008. He has participated in the European research initiatives "COST 231," "COST 259," and "COST273," where he was chairman of the MIMO channel working group, he was chairman of the IEEE 802.15.4a channel model standardization group, and was also chairman of Commission C (signals and systems) of URSI (International Union of Radio Scientists). Dr. Molisch is a Fellow of the IEEE, a Fellow of the IET, an IEEE Distinguished Lecturer, and recipient of several awards.

Paper IV

Characterization of a Computer Board-to-Board Ultra-Wideband Channel

Johan Karedal, *Student Member, IEEE*, Amit P. Singh, Fredrik Tufvesson, *Member, IEEE*, and Andreas F. Molisch, *Fellow, IEEE*

***Abstract*— In this paper we present the results of an extensive ultra-wideband (UWB) measurement campaign performed inside the chassis of two desktop computers. The purpose of the campaign is to analyze the possibility of board-to-board communications, replacing cable connections. Measurements of the propagation channel are performed over a frequency range of $3.1-10.6$ GHz using a vector network analyzer and antennas small enough to enable integration on a circuit board. The results show that the propagation environment is very uniform, with small variations in the path gain between different positions within a computer. We also performed interference measurements, showing that the interference is restricted to certain subbands.**

***Index Terms*— Ultra-wideband, channel measurements, interference, statistical model, wireless communications.**

I. Introduction

THE interest in ultra-wideband (UWB) communications has increased dramatically in recent years, with applications being found both for high-data-rate and low-data-rate communications. The attractiveness of UWB systems stems from properties such as low-power transmission, low-cost circuitry, and high possible data rates [1], [2]. The use of a large transmission bandwidth results in robustness to frequency-selective fading and allows using a low spectral density, which in turn enables a system with low interference to other wireless systems.

One of the many envisioned applications is the usage of UWB transmissions for communications between different circuit boards in desktop computers. Using small antennas that are integrated on the circuit boards, wireless UWB links can replace the currently used cable connections, thus simplifying automated installation and integration of a card into a computer. With the cable connections being removed, the usage of a new card would be one step closer to true "plug-and-play." A number of generic UWB transceiver schemes have been proposed in the past, which could be used for such board-to-board communications, including impulse radio with simplified Rake receivers, direct-sequence CDMA, multiband impulse radio with noncoherent detection, and OFDM. However, the relative merits of such schemes strongly depend on the propagation channels in which they operate [3], as well as the characteristics of the interference. Thus, the first step in designing a board-to-board communications system has to be an understanding of the UWB propagation channel, as well as the interference, within desktop computers.

This letter presents the (to our knowledge) first-ever measurements of UWB propagation channels within desktop computers.[1] We present extensive measurement results (some 4200 impulse responses) in two desktop computers, and derive a statistical model that can be used for system design and evaluation of transceiver performance.

II. Measurement Setup and Evaluation

Two computers were used for the measurements, in order to investigate the impact of different interior design. Both were brand new and based on current consumer market technologies (year 2006). One computer, by HP™ (Media Center PC, Model No. EP080AA-ABS), was factory assembled and had a very crowded interior. The second computer was bought in parts and assembled by the buyer (henceforth referred to as the assembled, or asb., computer), and had more empty space inside. Inside each computer, several realistic Tx/Rx positions (on the circuit boards, or locations on the outside of CD drive, hard drive, etc.) were selected. Each location was used as transmitter or receiver in different measurements. To attach the antennas on the circuit board, thin (3 mm) LEGO™ pieces were used (see Fig. 1). One LEGO piece was glued to e.g., the circuit board, with the other being glued to the antenna. This way, several channel samples could be taken at each Tx/Rx position (referred to as "Tx/Rx blocks"), with a well-defined separation, by translating the LEGO pieces on antenna and board relative to each other. Also, since the LEGO piece supports a 90° rotation, performing measurements with different orientations of the antennas was possible. Due to the crowded interior architecture of the computer, at some positions measurements were only possible using one of the orientations. In total, 1435 channel measurement (using 8 Tx/Rx blocks) were made in the HP computer and 2840 measurements (9 Tx/Rx blocks) were made in the assembled computer.

Measurements of the propagation channel between Tx and Rx were performed in the frequency domain using a vector network analyzer (HP 8720C) sweeping the frequency range $3.1-10.6$ GHz. With the frequency band being divided into 1601 points, this implies a delay resolution of 0.13 ns (i.e., 4 cm path resolution) and a maximum resolvable delay of 210 ns. The antennas were small-sized PIFA-like UWB antennas from SkyCross™ (Model No. SMT-3TO10M), small enough to allow for integration on a circuit board in a real application.

From the measured channel transfer functions $H(f)$, we obtain by inverse Fourier transformation (using a Hanning window to suppress sidelobes) the channel impulse responses

Manuscript received October 11, 2006. The associate editor coordinating the review of this letter and approving it for publication was Dr. Biao Chen.

J. Karedal and F. Tufvesson are with the Department of Electroscience, Lund University, Box 118, SE-221 00 Lund, Sweden (e-mail: Johan.Karedal@es.lth.se).

A. P. Singh is with the Department of Electronics and Computer Engineering, Indian Institute of Technology, Roorkee-247667, India.

A. F. Molisch is with the Department of Electroscience, Lund University, Box 118, SE-221 00 Lund, Sweden, and with Mitsubishi Electric Research Labs, 201 Broadway, Cambridge, MA 02139, USA.

Digital Object Identifier 10.1109/LCOMM.2007.061661.

[1] After our paper was accepted, we learned that parallel to our work, Chen and Zhang also performed similar measurements [4].

Fig. 1. An inside view of the HP computer. The eight circled Tx/Rx blocks (of various sizes) can be seen scattered over the computer. Block 6 is located in the horizontal plane, on the mother board, whereas block 7 is located in the vertical plane, on the hard drive (around 7 cm above the mother board). Also, inset in the top right corner is a (magnified: note the size of the SMA connector) picture of the SkyCross antenna.

$h(\tau)$, whose square magnitude $|h(\tau)|^2$ gives the power delay profiles (PDPs).[2] Averaging over the PDPs belonging to one Tx/Rx block combination, we obtain the average power delay profile (APDP). The step increment between two positions on a LEGO block is 8 mm, which with $5-7$ positions per block equals a total length of only $30-50$ mm. Since half a wavelength ($\lambda/2$) at 3.1 GHz is 48 mm, whereas $\lambda/2$ at 10.6 GHz corresponds to 14 mm, it should be pointed out that this implies an averaging over a rather small spatial area; the effects of this will be discussed later in the paper.

Since a running computer can be expected to produce interference, disturbing the radio link, we also performed interference measurements at all measurement positions in each computer. These measurements were performed with the computers running only the operating system (Windows XP; no other software applications were ran) inside a shielded chamber in order to avoid any unwanted signals. We used a spectrum analyzer (Rohde&Schwartz FSU) set to a resolution bandwidth of 3 kHz to sweep the measurement frequency range (divided into 2501 frequency points), and the measurements were made using the max peak detector in order to analyze the worst case interference power level at each frequency point.

III. Results

A. Propagation Channel Measurements

Our first observation concerns the path gain, i.e., $E\left\{(1/B)\int_B |H(f)|^2 df\right\}$, where $B = 7.5$ GHz, and the expectation is taken over the positions within a Tx/Rx block combination. It turns out that the path gains are very similar, regardless of what Tx and Rx block positions are considered. The measured *mean* path gain (taken over all Tx/Rx block combinations) in the HP computer is -29.1 dB, with a standard deviation of 2.1 dB, whereas in the assembled computer, a mean path gain of -28.7 dB with a standard deviation of 1.4 dB, was measured. It is noteworthy that despite the different distances between Tx and Rx, and despite the possibility of shadowing by metallic objects (component casings, fans, etc.) the variation of the path gain is extremely small.[3] We also note that the mean path gain is almost the same in both computers, despite their different interior layout.

Next, we analyze the delay dispersion. We note that the APDPs of our measurements include a small period of "soft onset" (generally less than 1 ns; see Fig. 2a), a phenomenen that has been observed and modeled in [6]. However, since a soft onset is mainly of interest for ranging techniques (which is not amongst the applications targeted in this paper), we find it more tractable to use a simpler approach; the single exponential decay. Hence, we model the APDPs as

$$P(\tau) = P_0 e^{-\tau/\gamma}$$

where P_0 is the power at delay $\tau = 0$, and γ is the decay time constant. The variations of γ within each computer are small, though we note that there is some difference between the two computers. This difference is likely due to the HP computer being more crowded (with scatterers), than the more empty assembled one, which hence has a slightly slower decay. We fitted the distribution of γ both to a normal distribution and a lognormal distribution [5]. While the normal distribution gave a marginally better fit, the lognormal distribution has the advantage that even theoretically, negative decay constants are not possible. We thus suggest to model $\gamma' = 10\log_{10}(\gamma/1\text{ ns})$, the decay constants on a dB scale, as normally distributed, $\gamma' \sim \mathcal{N}(\mu_{\gamma'}, \sigma_{\gamma'})$. The HP computer has a mean decay time constant $\mu_{\gamma'} = 5.42$ dBns with a standard deviation $\sigma_{\gamma'} = 0.11$ dBns, whereas the assembled computer has $\mu_{\gamma'} = 7.34$ dBns and $\sigma_{\gamma'} = 0.09$ dBns (see Fig. 2b). The corresponding linear mean values of γ, 3.49 ns and 5.44 ns, gives an approximate $0.5-$coherence bandwidth of 79 MHz for the HP computer, and 51 MHz for the assembled one.

We thus find that both the path gain, and the shape of the APDPs is essentially the same, regardless of which Tx/Rx blocks are considered. This leads to the conclusion that the propagation environment between two arbitrary pairs of Tx/Rx blocks inside the computer chassis is very similar, and fading margins to account for large-scale phenomena can be very small. Also, since different combinations of Tx/Rx blocks imply a different amount of LOS/NLOS, this also means that there is no significant difference between LOS and NLOS situations and subsequently no separation into LOS and NLOS has been made in our analysis. Finally, we find that rotating the antenna has no significant influence on the transmission. This latter effect is most likely due to the omnidirectional properties of the antennas, a result that also justifies our

[2]To compensate for the different runlengths of different Tx/Rx combinations, we have adjusted the delay axis of each impulse response according to the geometric distance between Tx and Rx [5]. Hence, the first component of an impulse responses is counted as the one arriving at the delay corresponding to the LOS distance.

[3]Actually, our measurement results slightly overestimate the path gain variance due to shadowing: some residual influence of small-scale fading is present, because the number of independent spatial samples within a Tx/Rx block is small. However, the importance of this effect is somewhat limited, since the measured path gains are averaged both over spatial samples and frequency samples.

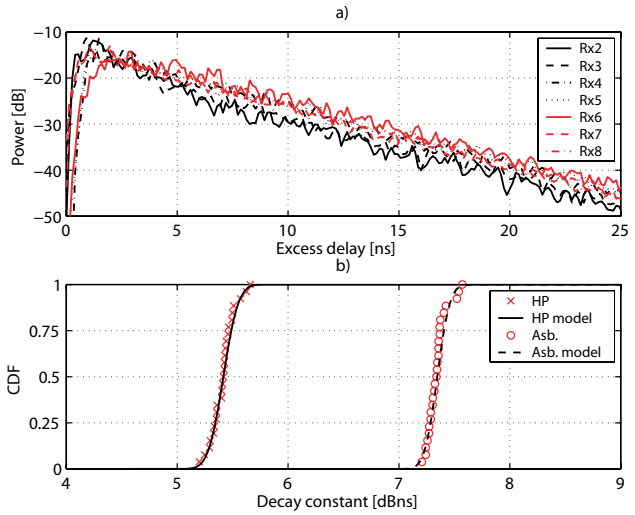

Fig. 2. a) The APDPs measured from Tx block 1 to all other (Rx) blocks in the HP computer. Each APDP is normalized so that the total power within the APDP is unity. The two lowest curves (Rx2 and Rx3) are measurements that are considered LOS (see Fig. 1). In b), the distribution of decay constants, as measured and modeled, respectively, is shown.

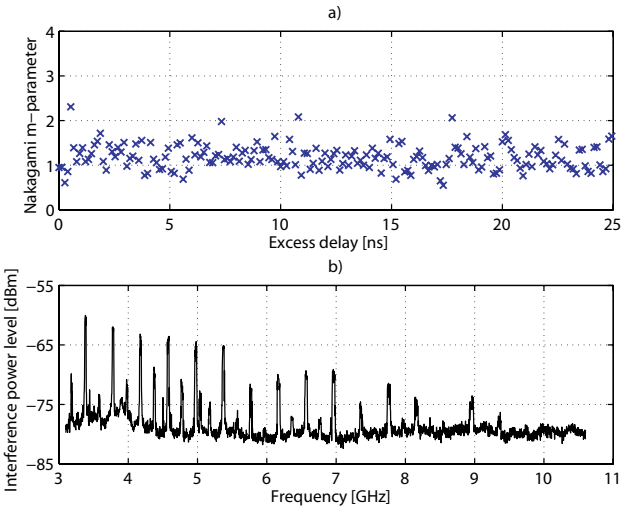

Fig. 3. a) The Nakagami m-parameter estimates of the amplitudes measured between Tx/Rx blocks 1 and 7 in the HP computer (note that $m = 1$ corresponds to a Rayleigh distribution). b) The maximum interference power level measured at Tx/Rx block 6 of the HP computer.

using all available measurements (per block) in the previous derivations of APDPs and path gains.

We next analyze the small-scale fading, by fitting the amplitude distribution belonging to all measurements of each Tx/Rx pair to the Nakagami$-m$ distribution, which is in widespread use for UWB (see [3] and references therein). Thus, for each delay, we estimate the $m-$parameter using the inverse normalized variance estimator [7]. An example plot of the result is shown in Fig. 3a, where the estimate can be seen to be close to 1, which corresponds to a Rayleigh distribution, for almost all delays. The mean value (over delay and all measurements) of the $m-$estimate was 1.19 for the HP computer, and 1.11 for the assembled one.

B. Interference Measurements

The results of the interference measurements show great variations in the power levels at different frequencies. Fig. 3b shows an example plot of the maximum interference power level, that can be seen to be essentially restricted to certain subbands. The subbands are approximately 30 MHz wide, and (with a few exceptions) separated by 400 MHz. The same behavior, probably caused by the memory bus, is observed at all Tx/Rx blocks of both computers, with only small variations in power level of the frequency peaks.

This result has two important consequences: (i) due to the similarity of interference level at different Tx/Rx blocks, no locations within the chassis are more suitable than another, in an applications sense (this is especially true in conjunction with the path gain and APDP results from the previous section), (ii) some bands of the frequency spectrum are very unsuitable for radio transmission, which serves as a motivation for using band-notch filters or OFDM-like systems, for this type of application.

IV. Conclusions

We have presented results from a UWB measurement campaign performed inside two different computer chassis. The measurements were made over a frequency range of $3.1-10.6$ GHz and show several interesting points:

- The propagation environment inside the computer chassis is very uniform, with similar values for the path gain regardless of antenna position.
- No significant large-scale fading effects was observed.
- The orientation of the antenna elements has no significant effect on the results.
- The power delay profile is given by a single exponential decay, with a decay constant that can be well described by a log-normal distribution.
- The amplitude statistics within the chassis is well described by a Rayleigh distribution.
- The interference caused by the computer is mainly restricted to certain subbands; however, the frequency spacing of the interference lines is less than 500 MHz.

The results can thus serve as basis for the design and performance simulation of UWB board-to-board communications systems.

References

[1] R. C. Qiu, H. Liu, and X. Shen, "Ultra-wideband for multiple access communications," *IEEE Commun. Magazine*, vol. 43, no. 2, pp. 80–87, Feb. 2005.

[2] G. di Benedetto *et al.*, *UWB Communications Systems: A Comprehensive Overview*. EURASIP Publishing, 2005.

[3] A. F. Molisch, "Ultrawideband propagation channels - theory, measurement, and modeling," *IEEE Trans. Veh. Technol.*, vol. 54, no. 5, pp. 1528–1545, Sept. 2005.

[4] Z. M. Chen and Y. P. Zhang, "Inter-chip wireless communication channel: Measurement, characterization, and modeling," *IEEE Trans. Antennas Propag.*, vol. 55, no. 3, pp. 978–986, Mar. 2007.

[5] D. Cassioli, M. Z. Win, and A. F. Molisch, "The ultra-wide bandwidth indoor channel: from statistical models to simulations," *IEEE J. Sel. Areas Commun.*, vol. 20, no. 6, pp. 1247–1257, Aug. 2002.

[6] A. F. Molisch et al., "IEEE 802.15.4a channel model - final report, Tech. Rep. Document IEEE 802.15-04-0662-02-004a, 2005.

[7] A. Abdi and M. Kaveh, "Performance comparison of three different estimators for the Nakagami *m* parameter using Monte Carlo simulation," *IEEE Commun. Lett.*, vol. 4, no. 4, pp. 119–121, Apr. 2000.

Paper V

A Measurement-Based Statistical Model for Industrial Ultra-Wideband Channels

Johan Karedal, *Student Member, IEEE*, Shurjeel Wyne, *Student Member, IEEE*, Peter Almers, *Student Member, IEEE*, Fredrik Tufvesson, *Member, IEEE*, and Andreas F. Molisch, *Fellow, IEEE*

***Abstract*— The results of three ultra-wideband (UWB) measurement campaigns conducted in two different industrial environments are presented. A frequency range of $3.1 - 10.6$ or $3.1 - 5.5$ GHz was measured using a vector network analyzer and a virtual array technique enabling the investigation of small-scale statistics. The results show that the energy arrives in clusters, and that the abundance of metallic scatterers present in the factory hall causes dense multipath scattering. The latter produces a small-scale fading that is mostly Rayleigh distributed; the only exception being the delay bin containing the line-of-sight component. The power delay profile can be modeled by a generalized Saleh-Valenzuela model, where different clusters have different ray power decay constants. It is also noted that the number of multipath components required to capture a majority of the energy is quite large. More than a hundred components can be needed to capture 50% of the total available energy.**

***Index Terms*— Ultra-wideband, channel measurements, statistical model, industrial environment.**

I. Introduction

In recent years, ultra-wideband (UWB) spread spectrum techniques have gained increasing interest [1], [2], [3], [4]. UWB systems are often defined as systems that have a relative bandwidth larger than 20% and/or absolute bandwidth of more than 500 MHz [5]. There are several qualities of UWB systems that can be of interest in the area of wireless communications. The large relative bandwidth, as well as the large absolute bandwidth, ensures resistance to frequency-selective fading, which implies more reliable communications [6], [7], [8]. Also, the spreading of the information over a very large frequency range decreases the spectral density. This decreases interference to existing systems (which is important for commercial applications) and makes interception of communication more difficult (which is of interest for military communications). Finally, the concept of impulse radio allows the construction of communications systems with simplified transceiver structures [3], [6].

UWB communications are envisioned for a number of applications and there are two major trends in the development of new systems. The first is high-data rate communications, with data rates in excess of 100 Mbit/s [9]. One typical application for such a high-rate system is high-definition TV transmission. The other trend is data rates below 1 Mbit/s, usually in the context of sensor networks, and in conjunction with UWB positioning systems. A considerable part of these systems will be deployed in industrial environments. Interesting applications include machine-to-machine communications in e.g., process control systems, or supervision of storage halls.

For the planning and design of any wireless system, channel measurements and modeling are a basic necessity [10]. Previous UWB measurement campaigns have been restricted to office and residential environments, and there exist channel models for those environments, see e.g., [11], [12], [13], [14]. However, industrial environments have unique propagation properties (large number of metallic objects, dimensions of halls and objects) and thus existing UWB channel models, especially, the standardized IEEE 802.15.3a model [15], are not valid there. On the other hand, available *narrowband* channel models in industrial environments (e.g., [16]) cannot be used, because the behavior of the narrowband and the UWB channel is remarkably different as have been shown by numerous theoretical as well as practical investigations [11], [13], [14], [17], [18], [19], [20]. For these reasons, there is an urgent need for measurements of the UWB channel in industrial environments, and a subsequent channel model. To our knowledge, no such investigation has been published yet.

In this paper, we present results from three UWB measurement campaigns that cover the FCC-approved frequency band [5] (measurement campaign three only covers $3.1 - 5.5$ GHz) conducted in two industrial halls. We propose a statistical model for the measured data suitable as a basis for system simulations. It should be noted, however, that since the number of different factory halls we measure is limited, we do not claim our model to describe any "general" industrial environment. They best agreement between model and measurement can obviously be expected in halls very similar to the ones where our measurements were performed. Also, the outcome of the first measurement campaign has been used as input to the channel modeling group of IEEE 802.15.4a [21].

The remainder of the paper is organized the following way: Section II gives the details of the measurement setup. In Section III, we describe the measurement environment and transmitter and receiver locations, while Section IV covers the data processing. Section V presents results for the multipath propagation, clustering, and delay spreads and Section VI gives a statistical model based on our measurements. Finally, a summary and conclusions about UWB system behavior in

Manuscript received December 21, 2005; revised July 18, 2006; accepted August 17, 2006. The associate editor coordinating the review of this paper and approving it for publication was R. M. Buehrer. Parts of this work have been published at Globecom 2004, VTC 2004 Fall, and WPMC 2005.

J. Karedal, S. Wyne, P. Almers, and F. Tufvesson are with the Department of Electroscience, Lund University, Lund, Sweden (e-mail: {Johan.Karedal, Shurjeel.Wyne, Peter.Almers, Fredrik.Tufvesson@es.lth.se).

A. F. Molisch is with Mitsubishi Electric Research Labs, Cambridge, MA and also at the Department of Electroscience, Lund University, Lund, Sweden (e-mail: Andreas.Molisch@ieee.org).

Digital Object Identifier 10.1109/TWC.2007.051050.

TABLE I
MEASUREMENT SETUP PARAMETERS

	Campaign No.		
	1	2	3
Frequency range [GHz]	$3.1-10.6$	$3.1-10.6$	$3.1-5.5$
Frequency points	1251	1601	981
Delay resolution [ns]	0.13	0.13	0.42
Max. resolvable delay [ns]	167	213	408
Element separation [mm]	50	37	50

the measured environment is presented in Section VII.

II. MEASUREMENT SETUP

The measurement data were acquired during three measurement campaigns. All measurements were performed in the frequency domain using a vector network analyzer (HP 8720C in the first two campaigns, Rohde&Schwartz ZVC in the third), determining the complex channel transfer function $H(f)$. In the first two campaigns, the measured frequency range was 3.1 to 10.6 GHz which implies a delay resolution of approximately 0.13 ns (corresponding to 4 cm path resolution). The difference between the two campaigns was the number of frequency points used. In the first campaign, the spectrum was divided into 1251 frequency points, i.e., 6 MHz between the frequency samples and thus a maximum resolvable delay (with the inverse Fourier transform technique that we use in this paper) of 167 ns (corresponding to 50 m path delay). In the second campaign, 1601 frequency points were used, implying a frequency resolution of 4.7 MHz and a maximum resolvable delay of 213 ns (64 m path delay). The third measurement campaign limited the measured frequency range to 3.1 to 5.5 GHz, giving a delay resolution of 0.42 ns. 981 frequency points were used, giving a maximum resolvable delay of 408 ns (122 m path delay).[1] All measurement parameters are summarized in Table I.

Omnidirectional conical monopole antennas (Antenna Research Associates, Model No. CMA-112/A) were used as transmitter as well as receiver throughout all three campaigns. Using stepper motors, the monopoles were moved to different positions along rails, thus creating a *virtual* uniform linear antenna array (ULA) at each end (for a picture of the full setup, see [22]). In the first and the third campaign, the separation between the array elements was set to 50 mm, which corresponds to $\lambda/2$ at 3.1 GHz. In the second, the array element separation was 37 mm ($\lambda/2$ at 4 GHz). By moving each antenna, a virtual MIMO system of 7 by 7 antennas was created. Each rail was mounted on a tripod, with a height of 1.0 m, and moved to various locations in the building.

III. MEASUREMENT ENVIRONMENT

A. Measurement Campaign 1 and 2: DSM Resins Scandinavia

The first two measurement campaigns were performed in a factory hall in Landskrona, Skåne, Sweden. The hall was an incinerator hall of DSM Resins Scandinavia, a chemical company producing resins for coating systems. The hall has a floor area of 13.6×9.1 m and a height of 8.2 m (see Fig. 1). Comparing this with the maximum path delay (see Section II) it can be noted that the latter is about four or five times the largest dimension of the building (for the first and second measurement campaign, respectively). The walls and ceiling of the factory hall consist mostly of metal (corrugated iron), whereas the floor is made of concrete. In addition to the metallic walls and ceiling, the building is also packed with metallic equipment, e.g., pumps, tanks and pipes (see Fig. 2). At one end of the building, there is a balcony (between points D to E in Fig. 1) at 3 m height. From the balcony, a metal grate bridge stretches into the room (the shaded area in Fig. 1), covering positions over the reaction chamber.

Inside the building, positions were selected to obtain three different scenarios, as well as three different transmitter - receiver separations. The different scenarios were: line-of-sight (LOS), peer-to-peer non-line-of-sight (PP NLOS) and base station (BS) NLOS. In the BS NLOS scenario, the transmitter array tripod was placed on top of the balcony (position 22 in Fig. 1) while the receiver array remained on floor level. For the LOS and PP NLOS scenarios, three

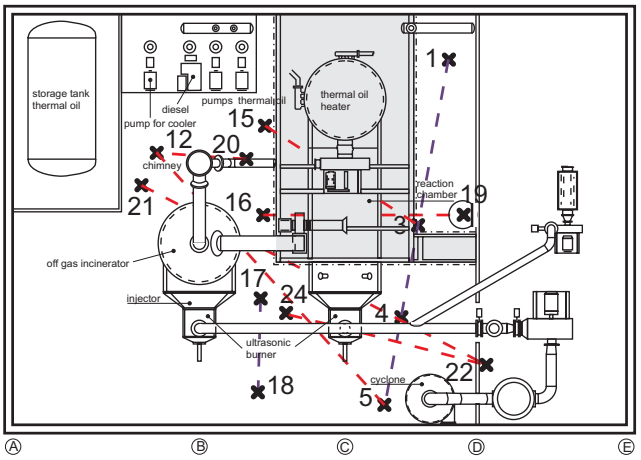

Fig. 1. The incinerator hall of DSM Resins as seen from above. The numbers indicate different antenna positions and the dashed lines show between which positions measurements were made.

Fig. 2. An inside view of the incinerator hall at DSM Resins. The photograph is taken from the position corresponding to the lower left corner of Fig. 1, showing the cyclone next to antenna position 5 at the rightmost of the picture.

[1]This campaign was actually measured over a frequency range $3.1-8.0$ GHz, but all resulting frequency responses displayed several strong peaks for the higher frequencies, probably due to interference from the equipment in the hall, and hence only the lowest 2.4 GHz was used in the analysis.

different antenna separations were measured, 2 m, 4 m and 8 m, whereas for the BS NLOS only two separations, 5 m and 9 m (horizontal distance), were used. Campaign one included three LOS measurements, all performed along the same line, alongside the reaction chamber, and five NLOS measurements (3 PP and 2 BS), where transmitter and receiver were separated by the reaction chamber and/or the parts of the incinerator. Campaign two included one LOS measurement and two PP NLOS measurements.

The antenna arrays were aimed to be aligned broadside to broadside, and hence parallel. However, for practical reasons achieving perfect aligning of the arrays was very difficult, especially for the NLOS measurements when often no points of reference could be used to assure a proper alignment.

There was no moving machinery inside the incinerator hall during the measurements, and no moving personnel. Thus, the measurement environment was stationary, a basic requirement for the measurement technique used here.

B. Measurement Campaign 3: MAX-Lab

The third measurement campaign was performed in MAX-Lab, a medium-sized industrial environment in Lund, Sweden. The hall has a floor area of 94×70 m and a ceiling height of 10 m. This hall has walls made of reinforced brick and concrete, a ceiling made of steel and a floor made of concrete. Since it also contains many metallic objects, e.g., pipes, pumps and cylinders, it too constitutes a rich scattering environment.

Inside the factory hall, 16 receive antenna positions for PP NLOS measurements, spread over 4 different Tx positions, were selected along with 6 receive antenna positions for BS NLOS, spread over 2 Tx positions. In the BS NLOS measurements, the Tx antenna was elevated 3 m above floor level. The measured Tx-Rx separations for PP NLOS were 2, 3, 4, 6, 8, 10, 12 and 16 m, whereas separations of 4, 8, and 12 m (horizontal distance) were used in the BS NLOS measurements.

IV. Measurement Data Processing

The measured transfer functions were processed the following way: the transfer function between the mth transmit and nth receive antenna position within the virtual arrays, $H(f,m,n)$, was inverse Fourier transformed (applying a Hanning window to suppress aliasing) to the delay domain, resulting in the impulse response $h(\tau,m,n)$.[2] From that, we define the instantaneous power delay profile (PDP) as the square magnitude of the impulse response, i.e.,

$$\text{PDP}(\tau,m,n)=\left|h(\tau,m,n)\right|^2 \tag{1}$$

For each 7×7-measurement the 49 corresponding instantaneous PDPs were averaged to obtain the averaged PDP (APDP) as

$$\text{APDP}(\tau)=\frac{1}{MN}\sum_{m=1}^{M}\sum_{n=1}^{N}PDP(\tau,m,n) \tag{2}$$

where M and N are the number of receive and transmit elements, respectively.

[2]Note that a small amount of aliasing is still present in some of our measurements, see, e.g., Fig. 5.

The method of spatial averaging is classical, but when used in conjunction with UWB it gives rise to some concerns. A multipath component that will arrive at a certain delay τ_i when received by antenna array element 1, will arrive a time increment $\Delta\tau$ later when received by antenna element 2. Due to the fine delay resolution, τ_i and $\tau_i+\Delta\tau$ may fall into different delay bins. In that case, the averaging will have a "smearing" effect, as what really should be present in only one delay bin instead will be represented in several.

In [11], it has been suggested to adjust the delay axis of the power delay profile so that the (quasi)-LOS component of all instantaneous PDPs of the same measurement corresponds to the same delay bin (the required adjustment can be obtained from simple geometrical considerations). Such a correction facilitates a more accurate extraction of the statistical parameters of the first arriving component. However, due to the array aligning and the maximum possible excess runtimes, this effect is not significant in our measurement setup for the LOS component. For later arriving components, no delay adjustment has been made either, since without accurate angular information for each MPC, such a procedure is not possible.

The concerns connected spatial averaging also affects the rms delay spread since, by definition, the delay spread is based on the APDP. However, since the rms delay spread is such a widely used parameter for a wireless channel, we included the results in our analysis. The rms delay spread is defined as the second central moment of the APDP [23]

$$S(\tau)=\sqrt{\frac{\int_{-\infty}^{\infty}\text{APDP}(\tau)\tau^2d\tau}{\int_{-\infty}^{\infty}\text{APDP}(\tau)d\tau}-\left(\frac{\int_{-\infty}^{\infty}\text{APDP}(\tau)\tau d\tau}{\int_{-\infty}^{\infty}\text{APDP}(\tau)d\tau}\right)^2} \tag{3}$$

V. Results

In this section, we analyze the measurement results, and draw conclusions about propagation effects. We will pay special attention to those effects that are specifically caused either by the industrial environment (multiple metallic reflectors) and/or the very large bandwidth of the measurements.

A. Power Delay Profiles

A first effect we can observe is that the APDPs consist of several distinct clusters, which are clearly identifiable even with the naked eye (see Fig. 3). This clustering of multipath components (MPCs) has also been observed in indoor office and indoor residential environments (both for the narrowband and the ultra-wideband case) and can be modeled by the Saleh-Valenzuela (SV) model [13], [14], [18], [19], [20], [21]. However, inspection of Fig. 3 reveals two important differences to the conventional SV model:

1) The decay time constants of the different clusters are different. Typically, clusters with a longer delay exhibit a larger decay time constant.
2) The clusters do not necessarily show a single-exponential decay. In some cases, they can be better described as the sum of a discrete (specular) component and a "diffuse" cluster with a longer decay time constant (see, e.g., the third cluster in the upper APDP of Fig. 3).

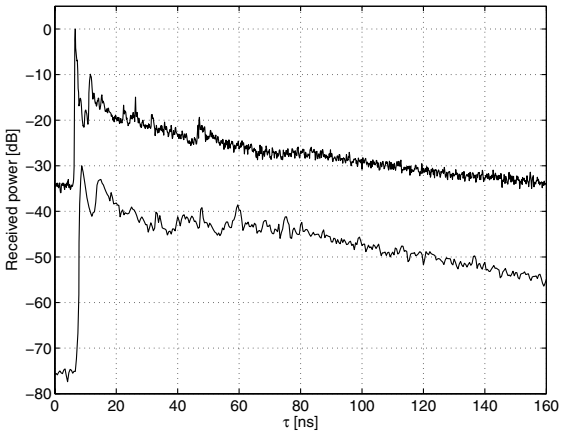

Fig. 3. Average power delay profiles for 2 m LOS (DSM Resins; upper curve) and 2 m PP NLOS (MAX-Lab; lower curve) normalized to their strongest component. The latter is plotted with a -30 dB offset.

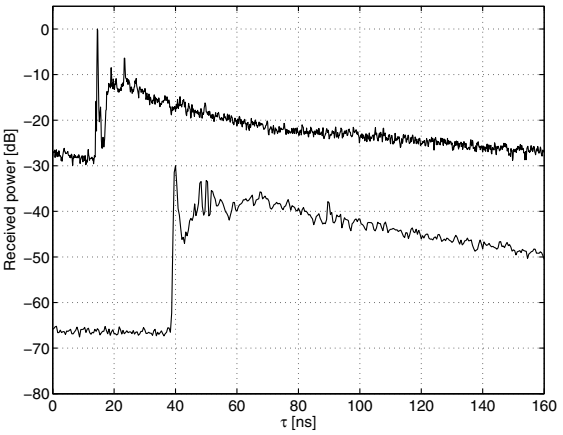

Fig. 4. Average power delay profiles for 4 m PP NLOS (DSM Resins; upper curve) and 12 m BS NLOS (MAX-Lab; lower curve) normalized to their strongest component. The latter is plotted with a -30 dB offset.

For the LOS components, as well as most NLOS situations, the first component is strong and followed by a pronounced minimum in the APDP. A similar effect has also been observed in office environments [18]. A possible interpretation for this minimum is that the Fresnel ellipsoid that corresponds to a delay of one bin (130 ps) is free of scatterers. Alternatively, the minimum is created by the "smearing" effect caused by the spatial averaging, since this effect is less pronounced for MPCs entering from broadside direction, such as the LOS component.

Another important observation in that context is that the first arriving component is very strong even in NLOS situations when the distance between Tx and Rx is small (see lower APDP of Fig. 3 and upper APDP of Fig. 4). A 4 m PP NLOS measurement was performed in measurement campaign 1, with the antennas separated by the large reaction chamber (Tx at position 19, Rx at position 16), i.e., LOS was definitely blocked. But even for this location that was so clearly NLOS, the effective behavior of the impulse response very much resembles the LOS measurements. Also, the rms delay spread value, 34 ns, of this measurement resembles the LOS results (e.g., the 4 m LOS has a mean rms delay spread of 31 ns) rather than the other NLOS measurements. Using a conventional beamformer [24] on the lowest 0.9 GHz sub-band $(3.1 - 4.0$ GHz)[3] for the upper APDP in Fig. 4 reveals that each of the two main peaks has an angle-of-arrival as well as an angle-of-departure that is almost broadside. Considering the delay times of these bins, one can by inspection of the map identify these paths. The first peak belongs to the path below the reaction chamber, reflected only by the floor, and the second is the path above the chamber, reflected by the metal grate on the balcony.

The measurements discussed above show a behavior that is somewhat similar to the classical exponential decay, i.e., the first arriving component is the strongest, and the APDP

[3]Since the main focus of this paper was not angular information, the antenna element separation of the virtual arrays was not selected to allow for an analysis of the whole frequency spectrum. The conventional beamformer may result in angular ambiguities when the antenna separation is larger than $\lambda/2$ and hence, only a low frequency sub-band was used in the analysis.

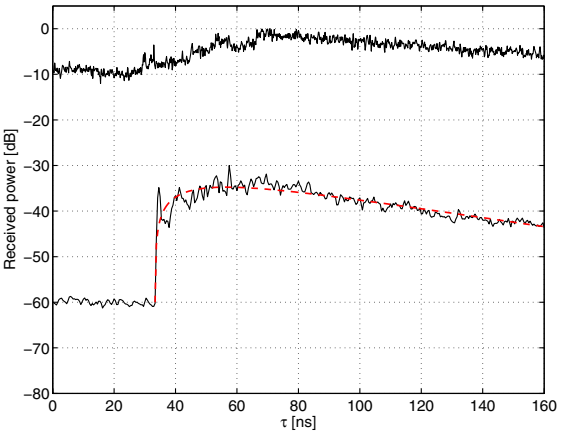

Fig. 5. Average power delay profiles for 8 m PP NLOS (DSM Resins; upper curve) and 10 m PP NLOS (MAX-Lab; lower curve) normalized to their strongest component. The latter is plotted with a -30 dB offset. The dashed curve shows a fit to Eq. (9).

(or at least the envelopes of the multiple clusters) decays more or less monotonically. However, this situation changes drastically for NLOS situations with larger Tx-Rx separations, as depicted in Fig. 5. There, we observe that the maximum of the APDP occurs some 10-40 ns *after* the arrival of the first multi-path component (MPC); the power after this maximum is monotonically decreasing. This shape of the APDP can have significant impact on the system performance, as discussed in Section VII.

Since these two types of APDP shapes are present in the results from both measurement sites, it seems reasonable to divide the analysis of the NLOS results into two groups, NLOS A and NLOS B. The NLOS A group contains measurements for shorter distances. These have a strong first component and a general shape very similar to the LOS cases. The NLOS B group contains measurements for larger distances, and these all have a "soft onset", i.e., a power that is not monotonically decreasing with delay. For DSM Resins, PP NLOS measurements over distances less than 8 m belong to NLOS A, while for MAX-Lab PP NLOS measurements over

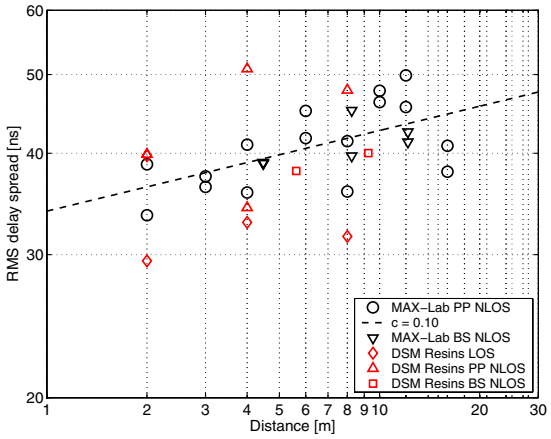

Fig. 6. Rms delay spread for all measurements. The dashed line ($c = 0.1$) corresponds to a best-fit to Eq. (4) for the MAX-Lab PP NLOS measurements.

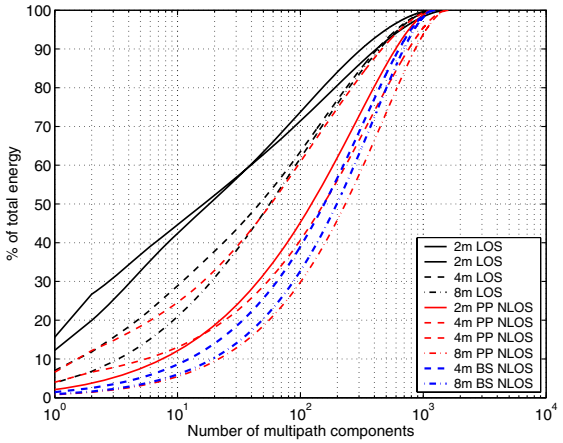

Fig. 7. The received energy for a certain number of multipath components for the measurements at DSM Resins.

distances less than 10 m belong to the same group.

Regarding the BS NLOS measurements, the APDP shape differs between the two sites. For DSM Resins, though it is hard to draw any general conclusions as only two BS measurement were made there, the APDP has a "soft onset" as in the case of the NLOS B discussion above. For MAX-Lab, however, the APDP shape agrees with shorter range measurements, i.e., they have a strong first component, even for the largest measured distance, 12 m (see lower APDP of Fig. 4). Hence, these are treated as NLOS A.

B. Delay Spread

As a further step, we analyze the rms delay spread in our measurements. For measurement campaign 1 and 2, the mean rms delay spread, as defined by Eq. 3, ranges from 28 ns to 38 ns for the LOS measurements, and from 34 ns to 51 ns for the NLOS measurement (PP and BS included). For measurement campaign 3, the rms delay spread varies between 34 ns to 50 ns for PP NLOS and between 39 ns and 45 ns for BS NLOS. For comparison, consider the narrowband measurements of [16] in an industrial environment: here, the rms delay spreads vary between 25 and 150 ns for both LOS and NLOS (there called OBS; obstructed); however, we note that the physical dimensions of some of those factory halls were larger than in our case.

The rms delay spread has often been reported to increase with distance [25]. This is also the case in our measurements. In Fig. 6 the rms delay spread is plotted as a function of distance for all measurements. Thus, we model the distance dependence with a power law as

$$\tau_{rms} \propto d^{c}. \tag{4}$$

Only the MAX-Lab PP NLOS scenario (represented by the circle markers in Fig. 6) has a number of measurements that is large enough to allow an extraction of the constant c, which in this case is 0.10.

For the design of Rake receiver systems, it is important to know the number of MPCs to be collected in order to capture a certain amount of the energy. Our analysis shows the difficulty of designing a Rake receiver for an industrial environment. For distances of 8 m in a NLOS scenario, collecting the 100 strongest MPCs would still only capture a little more than 30% of the total energy (see Fig. 7). This demonstrates the challenges of designing UWB systems in industrial environments.

VI. Statistical Model

In this section we give a statistical model that fits the measured data. As mentioned in Section V, our measured data show several clearly identifiable clusters in the APDPs, hence following the SV model seems reasonable. The SV model is widely accepted, simple and has also been adopted by the modeling group of IEEE 802.15.4a, where measurement campaign 1 of this paper was used as input. However, since then measurement campaign 2 and 3 has been conducted, and the combined result from all three measurement campaigns has given rise to some questions whether the power decay of the SV model being the best description. Hence, we also give a brief description on an alternative way of modeling the power decay in Section VI-B.

A. The Saleh-Valenzuela Model

The Saleh-Valenzuela (SV) model is commonly used to describe multi-cluster impulse responses, since its basic assumption is that multipath components arrive in clusters. In the SV model, the impulse response is given by

$$h(t) = \sum_{l=0}^{\infty} \sum_{k=0}^{\infty} \beta_{kl} e^{j\theta_{kl}} \delta(t - T_l - \tau_{kl}), \tag{5}$$

where β_{kl} and θ_{kl} are the gain and phase of the kth ray of the lth cluster, respectively, whereas T_l is the arrival time of the lth cluster and τ_{kl} the arrival time of the kth ray measured from the beginning of the lth cluster. The gain is determined by

$$\overline{\beta_{kl}^2} \equiv \overline{\beta^2(T_l, \tau_{kl})} = \overline{\beta^2(0,0)} e^{-T_l/\Gamma} e^{-\tau_{kl}/\gamma}, \tag{6}$$

where Γ and γ are the cluster and ray power decay constants, respectively [26].

Thus, to describe our measured data we need the following: Cluster arrival rate, ray arrival rate, cluster power decay and ray power decay. Note that the concept of cluster and ray power decay is only meaningful for LOS measurements and NLOS A measurements. The corresponding NLOS B analysis is covered in Section VI-A.5.

Our first objective is to divide each APDP into clusters. The identification can be performed in several ways: when the clusters are well-separated in the delay domain, it is sufficient to find the maxima of the power delay profile, since these signify the onset of a new cluster. Alternatively, a "best fit" procedure can be used, where the number and start time of clusters are used as parameters that are fitted to the measured power delay profile. This approach was used, e.g., in the parameterization of the IEEE 802.15.3a channel models. However, it can suffer from numerical problems - depending on the choice of the start values of the minimum-search algorithm, different solutions (that all fit the measurement results) can be obtained. It should be noted that, at the moment, there is no formal way of identifying clusters. We thus in this paper choose an approach "by visual inspection" [27], [28], as the human eye is good at the detection of patterns and structures even in noisy data.

To identify different clusters, we make use of two criteria: (i) the observation from Section V-A, that different clusters have different decay time constants, and (ii) that the onset of a new cluster most often is marked by a pronounced step in receive power. Hence, we can focus on identifying pronounced steps in conjunction with different slopes in our APDPs. The first criterion is used, so that, when stepping along the delay axis, a cluster contains all delay bins that can be described reasonably good by the same, fitted, regression line. Exceptions to this procedure occur when there is one strong (specular) component followed by some diffuse clutter, since the specular component is not that well described by a "decay of its own". In these cases, the specular component and the clutter are included in the same cluster. Generally, in all our measurements we have a number of clusters that ranges between 4 and 6. On average, 5 clusters are observed.

While the number of impulse responses used for estimation does affect the appearance of the APDP, we note that this number has no significant effect on our cluster identification. This, of course, unless more measurements from a *much larger* geometric area (i.e., using longer virtual arrays) are combined, as this would enhance the smoothing effect discussed in Section IV. Comparing APDPs derived from 25 measurements, with APDPs derived from 49 measurements, the clusters can be seen to be essentially the same.

1) Cluster Arrival Rate: The cluster arrival rate Λ is obtained by measuring the cluster interarrival times $\Delta T_l = T_l - T_{l-1}$ for each APDP, with $\Lambda = 1/\overline{\Delta T_l}$ where $\overline{\Delta T_l}$ is the average value within the APDP. We note that ΔT_l seems to increase with delay in our measurements. However, this is not used any further, since the number of measured T_l (which are *realizations* of a random variable) is not sufficient to allow determination of a general trend for the probability density function. According to the SV model, ΔT_l is described by an exponential distribution and this agrees well with our results (see Fig. 8). All values are given in Table II.

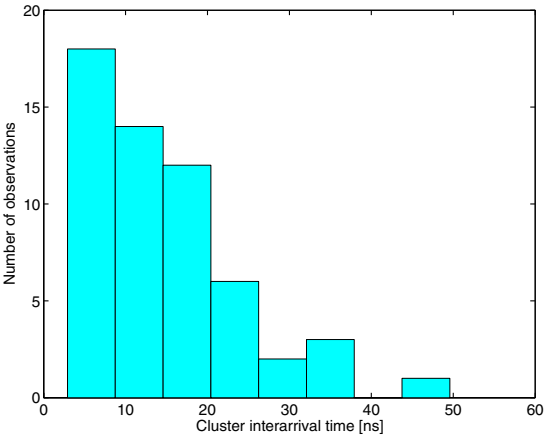

Fig. 8. A histogram of the cluster interarrival times for all measurement points from the measurements at MAX-Lab.

2) Ray Arrival Rate: The ray arrival rate λ is not determined since, despite the fine delay resolution (at best 0.13 ns, for measurement campaign 1), it was not possible to resolve the inter-path arrival times by an inverse Fourier transform of the measured data. Each resolvable delay bin contains significant energy. Therefore, we use a tapped delay line approach in our model, i.e., let every delay tap (on the measurement grid) contain energy according to Eq. (6).

3) Ray Power Decay: The standard SV model assumes that the γ:s are the same for all clusters of a certain impulse response. As previously mentioned, this is not the case in our measurements. The identification process of above immediately gives the ray power decay constant γ_l of each cluster as

$$\gamma_l = \frac{10}{k_{reg,l} \ln 10}, \tag{7}$$

where $k_{reg,l}$ is the negative slope of the regression line (on a dB-scale) belonging to cluster l and $\ln\{\sim\}$ is the natural logarithm. The γ values range from 0.5 to 70 ns, and since there are large differences of the values within a measurement, an average value is not a sufficient way of describing them. Generally, γ increases with delay, where the delay of a cluster l is defined as the arrival time of the first component of that very cluster, i.e., T_l in Eq. (5).[4] We thus propose a generalized SV model where γ increases linearly with delay (see Fig. 9), i.e.,

$$\gamma = \gamma(\tau) = \gamma_0 + a\tau, \tag{8}$$

where γ_0 is the ray power decay constant of the first cluster. This gives values of the constant a in the range of $0.5 - 1.2$ (see Table II).

4) Cluster Power Decay: The cluster power decay constant Γ is determined as the exponential decay of the peak power of the received clusters. To derive parameter values, we first normalize all (linear) cluster peak power values for each APDP so that the first cluster starts at 1. Then, all peak powers belonging to the same measurement site and scenario (e.g., PP

[4]Indeed, there are a few cases where some uncertainty remains regarding exactly when one cluster ends and the next one begins, but this has only a minor effect on our results.

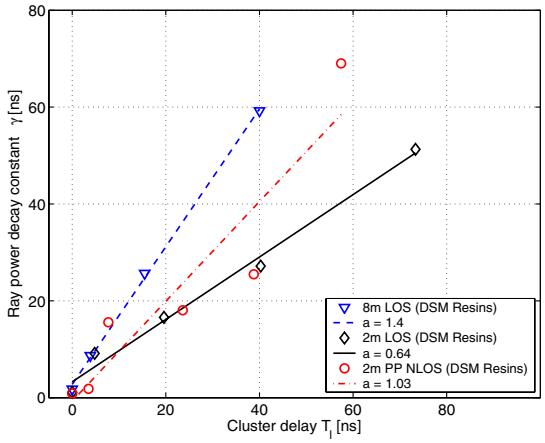

Fig. 9. Example plot of the linear delay dependence of the ray power decay constant γ. The figure shows γ as a function of delay for three different measurement positions from measurement campaign 1.

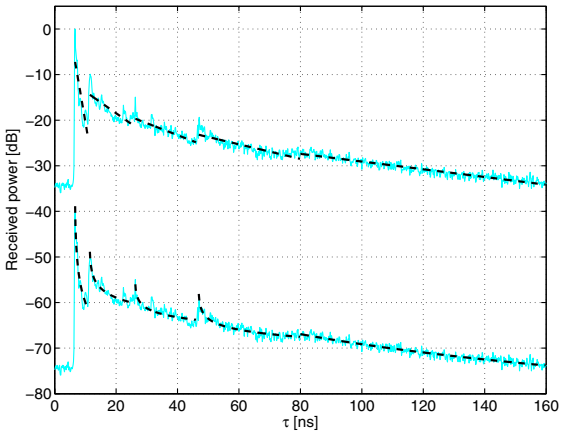

Fig. 10. A comparison of the classical SV model, i.e., an exponential power decay (upper curve), versus a power law decay (lower curve, plotted with a -40 dB offset) applied on the APDP of a 2m LOS measurement (DSM Resins). The upper curve has a mean square error (MSE) between measurement and model of $6.9 \cdot 10^{-4}$ whereas the lower curve has an MSE of $1.2 \cdot 10^{-4}$.

TABLE II
SALEH-VALENZUELA MODEL PARAMETERS

DSM	$1/\Lambda$ [ns]	Γ [ns]	γ_0 [ns]	a	γ_1 [ns]	γ_{rise} [ns]	χ
los	15.83	12.62	3.52	0.80	-	-	-
pp nlos a	13.10	29.78	4.13	1.19	-	-	-
pp nlos b	-	-	-	-	66.86	100	0.98
bs nlos (b)	-	-	-	-	71.36	11.12	0.90
MAX-Lab							
pp nlos a	16.00	28.87	4.98	0.54	-	-	-
pp nlos b	-	-	-	-	44.00	14.29	1.00
bs nlos (a)	12.53	24.01	2.53	0.69	-	-	-

NLOS) are plotted on a dB-scale as a function of the excess delay, and, finally, Γ is determined from a best-fit regression line in the same way as the ray power decay constant. This gives cluster power decay values in the range of $13 - 30$ ns (see Table II).

5) PDP Shape for NLOS B: As mentioned in Section V, the power of the measurements characterized as NLOS B is not monotonically decreasing, but there is a soft onset starting at the first arriving MPC where the power is actually increasing with delay. Hence, the power gains can no longer be described by Eq. (6). Instead, the power delay dependence is given by

$$\overline{\beta_{kl}^2} = \Omega_1 \frac{\gamma_1 + \gamma_{\text{rise}}}{\gamma_1 \left(\gamma_1 + \gamma_{\text{rise}} \left(1 - \chi\right)\right)} \left(1 - \chi e^{-\tau/\gamma_{\text{rise}}}\right) e^{-\tau/\gamma_1}, \tag{9}$$

where γ_1, γ_{rise} and χ are shape parameters while Ω_1 is the normalized power [21]. An example plot of the curve fitting of Eq. (9) is shown in Fig. 5. All parameter values are found in Table II.

B. Alternative Model - Power Law Approach

As previously mentioned, the SV model is commonly used, but it provides a fit to our data that is not entirely satisfactory. By mere inspection of the APDPs, it can be noted that the power decay of neither cluster, nor ray power is purely exponential (see Fig. 3). The ray power decay rather seems to follow a power law, i.e., the power within a cluster l is given by

$$P_{kl}\left(\tau_{kl}\right) = P_{0,l} \tau_{kl}^{-\alpha}, \tag{10}$$

where τ_{kl} is the arrival time of the kth ray measured from the beginning of the lth cluster. The power law decay has also been observed and discussed in [29], but then only for a single-cluster scenario. For our measurements, also the cluster peak power can be well described by a power law.

By visual inspection (see Fig. 10) the power law decay gives a better fit than the classical SV exponential decay. Results on this power law approach is reported in [30].

C. Small-Scale Statistics

For an indoor channel, many UWB measurement campaigns have reported an amplitude fading that follows a log-normal distribution (see e.g., [15]) or an m-Nakagami distribution (see e.g., [11]). Since these two distributions are the most frequently reported, we seek to analyze which of them that gives a better fit to our measured data, i.e., for each delay bin we investigate whether our observed amplitude vector $\mathbf{A} = \left[\begin{array}{cccc} A_1 & A_2 & \ldots & A_N \end{array}\right]$, where $N = 49$, has been drawn from an log-normal distribution or a m-Nakagami distribution. First, we turn our attention to the possibility of the latter, where m-parameter estimates are determined using the inverse normalized variance (INV) estimator [31]

$$\hat{m}_{INV} = \frac{\mu_2^2}{\mu_4 - \mu_2^2}, \tag{11}$$

where $\mu_k = N^{-1} \sum_{i=1}^{N} A_i^k$. It appears that for most of the measurements, an m-parameter estimate of 1 is achieved, which corresponds to a Rayleigh distribution. The only exception is for the delay bin containing the LOS component and a few adjacent delay bins. This is clearly different from the office environment in [11], where the m-parameter is found to be decreasing with the delay. Hence, the selection between log-normal and m-Nakagami changes to one between log-normal and Rayleigh.

Thus, for each delay bin we want to decide whether $\mathbf{A}$ was drawn from an Rayleigh distribution with a pdf

$p(\mathbf{A}; \hat{\sigma}_R, \text{Rayleigh})$, where $\hat{\sigma}_R$ is the maximum likelihood estimate (MLE) of σ_R given by

$$\hat{\sigma}_R = \sqrt{\frac{1}{2N}\sum_{i=1}^{N} A_i^2}, \tag{12}$$

or if $\mathbf{A}$ has been drawn from a log-normal distribution with a pdf $p(\mathbf{A}; \hat{\mu}_{LN}, \hat{\sigma}_{LN}, \text{log-normal})$, where $\hat{\mu}_{LN}$ and $\hat{\sigma}_{LN}$ are the MLEs of μ and σ given by the mean and standard deviation of $\ln\{\mathbf{A}\}$, respectively.

To make a choice between the two candidate distributions, we perform a generalized likelihood ratio test (GLRT) that decides, without favoring any of the two distributions, a Rayleigh distribution being the most likely if

$$\frac{p(\mathbf{A}; \hat{\sigma}_R, \text{Rayleigh})}{p(\mathbf{A}; \hat{\mu}_{LN}, \hat{\sigma}_{LN}, \text{log-normal})} > 1. \tag{13}$$

The result of the GLRT is that a Rayleigh distribution is more probably in more than 80% of the (excess) delay bins for each measurement. Hence, our model assumes that a Rayleigh distribution is applicable at all delays except for the LOS component. However, in order to avoid having to use different distributions for different delay bins, a more practical solution is to apply an m-Nakagami distribution to all delay bins, with an m-value of 1 used for all delay bins except the one containing the LOS component.

Several other tests have also been made in order to verify the result: (*i*) a Kolmogorov-Smirnoff test, (*ii*) a comparison of the mean square error between on one hand the cdf:s of a Rayleigh distribution and the measured data, and on the other the cdf:s a log-normal distribution and the measured data, (*iii*) a comparison of the Kullback-Leibler (KL) distance between a Rayleigh distribution and the measured data versus the KL distance between a log-normal distribution and the measured data. All of these tests have a few weaknesses, but regardless of these, all tests point towards a Rayleigh distribution.

The Rayleigh fading amplitude is a somewhat surprising result since it has been assumed that the fine resolution of the UWB would imply a too small number of paths arriving in each delay bin to fulfil the central limit theorem (CLT). A possible explanation why Rayleigh fading is yet observed here is that the high density of scatterers of the industrial environment creates a number of paths that is high enough to fulfil the CLT. An alternative explanation is that the problems of spatial averaging described in Section IV causes the Rayleigh distribution, i.e., the 49 values constituting the statistical ensemble for a certain delay bin may not be samples of the same MPC, but instead samples of several *different* MPCs.

D. Pathloss

The distance dependent pathloss is determined from scatter plots of the received power and modeled in dB, as

$$PL(d) = PL_0 + 10n\log_{10}\left(\frac{d}{d_0}\right) + X_\sigma \tag{14}$$

where PL_0 is the pathloss at a reference distance d_0, n is the pathloss exponent and X_σ is a log-normal distributed fading with standard deviation σ. Fig. 11 shows scatter plots

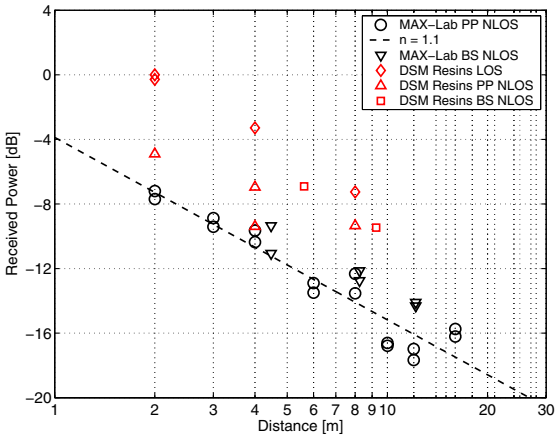

Fig. 11. Scatter plot of the received power for all measurements, normalized to the strongest value.

from all measurements. Only the MAX-Lab PP-NLOS data are sufficient to render reliable pathloss parameters, but it can be seen from the figure that the power samples from the other scenarios/measurements follow a very similar decay. The pathloss exponent for the MAX-Lab PP-NLOS is estimated to 1.1, whereas the log-normal fading has a standard deviation $\sigma = 1.1$ dB. We note that this pathloss exponent is surprisingly low, much lower than what other measurement campaigns have reported in the literature. A possible cause for the low exponent is the very rich multipath in the factory hall.

E. Validation of Model

To prove the validity of the model, we generate a number of impulse responses for each scenario and compare the simulation results with our measurements. Deriving 100 APDPs, each averaged from 49 individual impulse responses as given by Eqs. (5) and (6), gives a good fit for the rms delay spread. We obtain a simulated mean value of 27 ns for DSM LOS, to compare with the measured values of $28-38$ ns. For DSM NLOS A, simulated mean is 36 ns, whereas measured values are between $34-50$ ns. For MAX-Lab PP NLOS A, we obtain a simulated mean of 40 ns, to compare with the measured values $34-45$ ns, whereas for MAX-Lab PP NLOS B, our simulated value of 41 ns is to compare with the measured delay spreads $38-50$ ns.

For the energy capture by Rake receivers, the measurement bandwidth is different between the two factory halls. Therefore, our reported number of required Rake fingers is higher for the DSM hall than for MAX-Lab. Comparing the energy capture of a 5 finger Rake receiver, we find that for DSM LOS, the simulation renders a mean value of 13%, to compare with the measured values of $13-36\%$, whereas a simulated 20 finger Rake receiver would on average capture 31% of the energy, compared with $30-52\%$ in the measurements. For DSM NLOS A, the simulated mean energy capture of a 5 finger Rake is 6%, to compare with the measured $7-18\%$. Corresponding values for a 20 finger Rake is 16% (simulated) and $18-32\%$ (measured). For MAX-Lab PP-NLOS A, a simulated Rake receiver captures, on average, 16 and 39% for 5 and 20 fingers, respectively. Measured values range between

14 and 33% for a 5 finger Rake, and between 34 and 59% for a 20 finger Rake. Finally, for MAX-Lab PP-NLOS B, the simulated mean energy capture for a 5 and 20 finger Rake, respectively, is 10 and 29%, to compare with the measured values $12-17\%$ and $31-40\%$.

VII. Summary and Conclusions

We presented measurements of the ultra-wideband channel in two factory halls. The measurements cover a bandwidth from $3.1-10.6$ or $3.1-5.5$ GHz, and thus give very fine delay resolution. The main results can be summarized as follows:

- Due to the presence of multiple metallic reflectors, the multipath environments are dense; in other words, almost all resolvable delay bins contain significant energy - especially for NLOS situations at larger distances. This is in contrast to UWB office environments, as described, e.g., in [15].
- The inter-path arrival times were so small that they were not resolvable even with a delay resolution of 0.13 ns.
- For shorter distances, a strong first component exists, irrespective of whether there is LOS or not.
- For larger distances and PP NLOS scenarios, the maximum of the power delay profile is several tens of nanoseconds after the arrival of the first component. The common approximation of a single-exponential PDP does not hold at all in those cases.
- Clusters of MPCs can be observed.
- Delay spreads range from 30 ns for LOS scenarios at shorter distances to 50 ns for NLOS at larger distances.

We have also established a statistical model that describes the behavior of the channel, where it is found that the power delay profile can be well described by a generalized Saleh-Valenzuela model (with model parameters given in Table II), which is also used in the IEEE 802.15.4a channel models [21]. There are several noteworthy points:

- In contrast to the classical SV model, the ray power decay constants depend on the excess delay. This dependence is well described by a linear relationship. The decay constants vary between 0.5 and 70 ns.
- The peak cluster power can be described by an exponential function of the excess delay.
- The number of clusters varies between 4 and 6.
- The small-scale fading is well described by a Rayleigh distribution, except for the first components in each cluster, which can show a strong specular contribution.

Additionally, we found that the number of MPCs that is required for capturing 50% of the energy of the impulse response can be very high, up to 200. This serves as motivation to investigate suboptimum receiver structures that do not require one correlator per MPC, e.g., transmitted-reference schemes, [32], [33], [34], as well as noncoherent schemes. Also, the energy capture of partial Rake receivers, that match their fingers to the *first* arriving multipath components, will be highly affected in our measured NLOS scenarios, especially at larger distances.[5] This is due to the fact that the maximum of the PDP occurs some 250 taps *after* the arrival of the first MPC. Furthermore, the pronounced minimum between the LOS component and the subsequent components also reduces the energy capture of the partial Rake in LOS scenarios. We also find that a considerable percentage of the received energy lies outside a 60 ns wide window; this is important in the context of a current IEEE 802.15.3a standardization proposal, which uses OFDM with a 60 ns guard interval.

Our results emphasize the crucial importance of realistic channel models for system design. Parts of the measurements have been used as an input to the IEEE 802.15.4a channel modeling group, which (among other issues) recently have developed a channel model for industrial environments. Our measurement results thus allow a better understanding of UWB factory channels, and provide guidelines for robust system design in such environments.

[5]The overall performance, however, is determined by the combination of pathloss, amount of fading, and energy capture.

VIII. Acknowledgements

We thank DSM Resins Scandinavia for their permission to perform the measurements in their factory hall. Especially, we would like to thank Mr. Bengt-Åke Ling, Mr. Gert Wranning, and Mr. Alf Jönsson for their help and cooperation. We would also like to express gratitude to MAX-Lab for their permission to letting us perform measurements and to Mr. M. Gufran Khan and Mr. Asim A. Ashraf for their assistance during measurement campaign 3. Part of this work was financially supported by an INGVAR grant of the Swedish Strategic Research Foundation and the SSF Center for High Speed Wireless Communication.

References

[1] R. A. Scholtz, "Multiple access with time-hopping impulse modulation," in *Proc. IEEE Military Communications Conference*, vol. 2, 1993, pp. 447–450.

[2] M. Z. Win and R. A. Scholtz, "Ultra-wide bandwidth time-hopping spread-spectrum impulse radio for wireless multiple-access communications," *IEEE Trans. Commun.*, vol. 48, pp. 679–691, Apr. 2000.

[3] C. J. LeMartret and G. B. Giannakis, "All-digital PAM impulse radio for multiple-access through frequency-selective multipath," in *Proc. IEEE Global Telecommunications Conference*, 2000, pp. 77–81.

[4] M. G. diBenedetto, T. Kaiser, A. F. Molisch, I. Oppermann, C. Politano, and D. Porcino (eds.), *UWB communications systems, a comprehensive overview*. Hindawi Publishing, 2005.

[5] Federal Communications Commission, "First report and order 02-48," 2002.

[6] M. Z. Win and R. A. Scholtz, "Impulse radio: how it works," *IEEE Commun. Lett.*, vol. 2, pp. 36–38, Feb. 1998.

[7] ——, "On the robustness of ultra-wide bandwidth signals in dense multipath environments," *IEEE Commun. Lett.*, vol. 2, no. 2, pp. 51–53, Feb. 1998.

[8] ——, "On the energy capture of ultra-wide bandwidth signals in dense multipath environments," *IEEE Commun. Lett.*, vol. 2, no. 9, pp. 245–247, Sept. 1998.

[9] C. Duan, G. Pekhteryev, J. Fang, Y. Nakache, J. Zhang, K. Tajima, Y. Nishioka, and H. Hirai, "Transmitting multiple HD video streams over UWB links," in *Proc. IEEE Consumer Communications and Networking Conference*, vol. 2, Jan. 2006, pp. 691–695.

[10] A. F. Molisch, *Wireless Communications*. Chichester, West Sussex, UK: IEEE Press–Wiley, 2005.

[11] D. Cassioli, M. Z. Win, and A. F. Molisch, "The ultra-wide bandwidth indoor channel: From statistical models to simulations," *IEEE J. Sel. Areas Commun.*, vol. 20, no. 6, pp. 1247–1257, Aug. 2002.

[12] S. Ghassemzadeh, R. Jana, C. Rice, W. Turin, and V. Tarokh, "Measurement and modeling of an ultra-wide bandwidth indoor channel," *IEEE Trans. Commun.*, vol. 52, pp. 1786–1796, 2004.

[13] C.-C. Chong and S. K. Yong, "A generic statistical based UWB channel model for highrise apartments," *IEEE Trans. Antennas Propag.*, vol. 53, no. 8, pp. 2389–2399, Aug. 2005.

[14] C.-C. Chong, Y. Kim, S. K. Yong, and S. S. Lee, "Statistical characterization of the UWB propagation channel in indoor residential environment," *Wiley J. Wireless Commun. Mobile Computing*, vol. 5, no. 5, pp. 503–512, Aug. 2005.
[15] A. F. Molisch, J. R. Foerster, and M. Pendergrass, "Channel models for ultrawideband personal area networks," *IEEE Personal Commun. Mag.*, vol. 10, pp. 14–21, Dec. 2003.
[16] T. S. Rappaport, S. Y. Seidel, and K. Takamizawa, "Statistical channel impulse response models for factory and open plan building radio communication system design," *IEEE Trans. Commun.*, vol. 39, no. 5, pp. 794–807, May 1991.
[17] R. C. Qiu, "A generalized time domain multipath channel and its application in ultra-wideband UWB wireless optimal receiver design - Part II: Physics-based system analysis," *IEEE Trans. Wireless Commun.*, vol. 3, no. 6, pp. 2312–2324, 2004.
[18] J. Kunisch and J. Pamp, "Measurement results and modeling aspects for the UWB radio channel," in *IEEE Conference on Ultra Wideband Systems and Technologies Digest of Technical Papers*, 2002, pp. 19–23.
[19] A. S. Y. Poon and M. Ho, "Indoor multiple-antenna channel characterization from 2 to 8 GHz," in *Proc. Int. Conference on Communications*, May 2003.
[20] A. F. Molisch, "Ultrawideband propagation channels - theory, measurement, and modeling," *IEEE Trans. Veh. Technol.*, vol. 54, no. 5, pp. 1528–1545, Sept. 2005.
[21] A. F. Molisch et al., "IEEE 802.15.4a channel model - final report, Tech. Rep. Document IEEE 802.15-04-0662-02-004a, 2005.
[22] J. Karedal, F. Tufvesson, P. Almers, S. Wyne, and A. F. Molisch, "Setup for frequency domain ultra-wideband measurements using the virtual array principle," Dept. of Electroscience, Lund University, Sweden, Tech. Rep. ISSN 1402-8840, No. 9, Sep. 2006.
[23] T. S. Rappaport, *Wireless Communications—Principles and Practices*. Upper Saddle River, NJ: Prentice Hall, 1996.
[24] H. Krim and M. Viberg, "Two decades of array signal processing: The parametric approach," *IEEE Signal Processing Mag.*, vol. 13, no. 4, pp. 67–94, July 1996.
[25] L. J. Greenstein, V. Erceg, Y. S. Yeh, and M. V. Clark, "A new path-gain/delay-spread propagation model for digital cellular channels," *IEEE Trans. Veh. Technol.*, vol. 46, no. 2, pp. 477–485, May 1997.
[26] A. A. M. Saleh and R. A. Valenzuela, "A statistical model for indoor multipath propagation," *IEEE J. Sel. Areas Commun.*, vol. 5, no. 2, pp. 128–137, Feb. 1987.
[27] L. Vuokko, P. Vainikainen, and J. Takada, "Clusters extracted from measured propagation channels in macrocellular environments," *IEEE Trans. Antennas Propag.*, vol. 53, pp. 4089–4098, Dec. 2005.
[28] M. Toeltsch, J. Laurila, K. Kalliola, A. F. Molisch, P. Vainikainen, and E. Bonek, "Statistical characterization of urban spatial radio channels," *IEEE J. Sel. Areas Commun.*, vol. 20, pp. 539–549, Apr. 2002.
[29] J. B. Andersen and P. Eggers, "A heuristic model of power delay profiles in landmobile communications," in *Proc. URSI International Symposium on Electromagnetic Theory*, Sydney, 1992, pp. 55–57.
[30] J. Karedal, F. Tufvesson, and A. F. Molisch, *IEEE Commun. Lett.*, to be published.
[31] A. Abdi and M. Kaveh, "Performance comparison of three different estimators for the Nakagami *m* parameter using Monte Carlo simulation," *IEEE Commun. Lett.*, vol. 4, no. 4, pp. 119–121, Apr. 2000.
[32] J. D. Choi and W. E. Stark, "Performance of ultra-wideband communications with suboptimal receivers in multipath channels," *IEEE J. Sel. Areas Commun.*, vol. 20, no. 9, pp. 1754–1766, Dec. 2002.
[33] F. Tufvesson, S. Gezici, and A. F. Molisch, "Ultra-wideband communications using hybrid matched filter correlation receivers," *IEEE Trans. Wireless Commun.*, in press.
[34] T. Q. S. Quek and M. Z. Win, "Analysis of UWB transmitted reference communication systems in dense multipath channels," *IEEE J. Sel. Areas Commun.*, vol. 23, no. 9, pp. 1863–1874, Sept. 2005.

Johan Karedal received the M.S. degree in engineering physics in 2002 from Lund University in Sweden. In 2003, he started working towards the Ph.D. degree at the Department of Electroscience, Lund University, where his research interests are on channel measurement and modeling for MIMO and UWB systems. He has participated in the European research initiative "MAGNET."

Shurjeel Wyne received his B.Sc. degree in electrical engineering from UET Lahore in Pakistan, and his M.S. degree in digital communications from Chalmers University of Technology, Gothenburg in Sweden. In 2003, he joined the radio systems group at Lund University in Sweden, where he is working towards his PhD. His research interests are in the field of measurement and modeling of wireless propagation channels particularly for MIMO systems. Shurjeel has participated in the European research initiative "COST273," and is currently involved in the European network of excellence "NEWCOM."

Peter Almers received the M.S. degree in electrical engineering in 1998 from Lund University in Sweden. In 1998, he joined the radio research department at TeliaSonera AB (formerly Telia AB), in Malmö, Sweden, mainly working with WCDMA and 3GPP standardization physical layer issues. Peter is currently working towards the Ph.D. degree at the Department of Electroscience, Lund University. He has participated in the European research initiatives "COST273," and is currently involved in the European network of excellence "NEWCOM" and the NORDITE project "WILATI." Peter received an IEEE Best Student Paper Award at PIMRC in 2002.

Fredrik Tufvesson was born in Lund, Sweden in 1970. He received the M.S. degree in Electrical Engineering in 1994, the Licentiate Degree in 1998 and his Ph.D. in 2000, all from Lund University in Sweden. After almost two years at a startup company, Fiberless Society, Fredrik is now associate professor at the department of Electroscience. His main research interests are channel measurements and modeling for wireless communication, including channels for both MIMO and UWB systems. Beside this, he also works with channel estimation and synchronization problems, OFDM system design and UWB transceiver design.

Andreas F. Molisch (S'89, M'95, SM'00, F'05) received the Dipl. Ing., Dr. techn., and habilitation degrees from the Technical University Vienna (Austria) in 1990, 1994, and 1999, respectively. From 1991 to 2000, he was with the TU Vienna, becoming an associate professor there in 1999. From 2000-2002, he was with the Wireless Systems Research Department at AT&T (Bell) Laboratories Research in Middletown, NJ. Since then, he has been with Mitsubishi Electric Research Labs, Cambridge, MA, USA, where he is now Distinguished Member of Technical Staff. He is also professor and chairholder for radio systems at Lund University, Sweden.

Dr. Molisch has done research in the areas of SAW filters, radiative transfer in atomic vapors, atomic line filters, smart antennas, and wideband systems. His current research interests are measurement and modeling of mobile radio channels, UWB, cooperative communications, and MIMO systems. Dr. Molisch has authored, co-authored or edited four books, among them the recent textbook *Wireless Communications* (Wiley-IEEE Press), 11 book chapters, some 100 journal papers, and numerous conference contributions.

Dr. Molisch is an editor of the *IEEE Transactios Wireless Communications*, co-editor of recent and upcoming special issues on UWB (in *IEEE Journal on Selected Areas in Communications* and *Proc. IEEE*). He has been member of numerous TPCs, vice chair of the TPC of VTC 2005 spring, general chair of ICUWB 2006, and TPC co-chair of the wireless symposium of Globecom 2007. He has participated in the European research initiatives "COST 231," "COST 259," and "COST273," where he was chairman of the MIMO channel working group, he was chairman of the IEEE 802.15.4a channel model standardization group, and is also chairman of Commission C (signals and systems) of URSI (International Union of Radio Scientists). Dr. Molisch is a Fellow of the IEEE, an IEEE Distinguished Lecturer, and recipient of several awards.